EFFECTS OF AGING AND DISUSE ON BONE REMODELING IN RESPONSE TO MICRODAMAGE

by

Erik Ingemann Waldorff

A dissertation submitted in partial fulfillment
of the requirements for the degree of
Doctor of Philosophy
(Biomedical Engineering)
in the University of Michigan
2008

Doctoral Committee:

Professor Steven A. Goldstein, Chair
Professor Susan V. Brooks
Professor Laurie Kay McCauley
Assistant Professor Joshua D. Miller
Research Assistant Professor Barbara R. McCreadie

Til mor og far fordi I altid har støttet mig.
To my wonderful wife Sarah, whom I love tons and tons.

ACKNOWLEDGEMENTS

Many individuals and funding sources helped make contributions to my work. First I would like thank my thesis committee Susan Brooks, Laurie McCauley, Barbara McCreadie, Joshua Miller, and Steven Goldstein for their guidance through my education as a doctoral student. In particular I would like to thank Steve and Barbara for their guidance and knowledge as advisors, giving me the added perspective of both a senior and junior faculty member of the Orthopaedic Research Laboratories (ORL). Barbara's initial assistance over the first two years helped me transition from the now far away world of aerospace engineering, to biomedical engineering. As my principal advisor over the past three years, Steve helped me become the scientist I am today though his guidance, insight and always helpful suggestions. His down to earth approach with his students, whether in lab, his office, at his home or on the softball field created a wonderful environment of learning.

Funding for my research and education was provided by four sources which were: An American Federation for Aging Research (AFAR) Grant; The University of Michigan-NASA Bioscience and Engineering Institute (NNC04AA21A); NIH-AR46024 and The University of Michigan Geriatrics Center Research Training Grant (NIH/NIA T32-AG000114). I am grateful for the funding without which the research would never have been completed.

Several undergraduate/medical students have aided me with my research. Carl Hammaker and Merry Shao helped me with the rat bone chamber and microdamage models, respectively. Most significantly Katya Christenson helped me clean and maintain all of our hindlimb suspended rats, and did a tremendous job on the microCT analysis. Her assistance significantly shortened the duration of my thesis research.

Several campus laboratories offered integral assistance with many protocols essential to the completion of my thesis. From David Fox's lab, Laura Tesmer offered her expertise on flow cytometry. Additional members from this lab, Judy Endres and Chinh Tran were also helpful answering my questions or "lending" me reagents. From David Kohn's lab, Nadder Sahar and Joseph Wallace helped with the initial confocal microscopy, and gave great advice when it came to embedding and polishing microdamage specimens. In Laurie McCauley's lab, Amy Koh taught me how to run an ELISA, while Jinhui Liao, and Flavia Pirih helped me get started with the TRAP protocols. From Dr. Ron Midura's lab at the Cleveland Clinic, Dr. Caroline "Charlie" Androjna helped develop the hindlimb suspension protocol presented in chapter 3. From Dr. Sue Brooks' lab, Jay Salazar provided the rats and space for the initial test of the hindlimb suspension system.

Over the course of my thesis, I also participated in several collaborative experiments (not presented in this thesis). From Michael Morris' lab, Jacque Cole and I explored a novel microdamage detection method using light scattering. From Theo Ross' lab, Theo Ross, Teresa Hyun, Sarah Bradley, Lina Li and Katherine Oravecz-Wilson helped me characterize the skeletal phenotype of HIP1 double knock-out mice developed in the Ross lab.

I have come to realize what a perfect research environment the Orthopaedic Research Laboratories is during my years of research. It is virtually a utopia of resources with a tremendous faculty and staff, all of whom I have enjoyed working with tremendously, and without whom I could never have completed this thesis. Bonnie Nolan and Kathy Sweet helped set up animal surgeries, cared for my rats, taught me animal care, and helped at odd hours during the weekends. In particular Bonnie spent many of her weekends wrapping rat tails and dissecting tibiae with me. Dennis Kayner, and Charles Roehm were willing to do anything for the benefit of the projects, and extremely helpful in designing, building, machining and fixing experimental equipment. Rochelle Taylor and John Baker helped me with their great knowledge and expertise in histology. Rochelle sectioned countless specimens for me while John and Rochelle both helped me determine the appropriate techniques for my thesis analysis. Peggy Piech helped me get on Steve's schedule, and always knew his whereabouts so I could catch five minutes with him. Sharon Vaassen always made sure I was paid at the end of the month, and Sylvia Steffani helped me with all of my special orders. Ed Sihler and Oleg Svintsitski kept my trusted laptop running perfectly, kept my data safe, and optimized the computers for my gigantic MicroView files. Jaclynn Kriegl has been a great resource of orthopaedic knowledge and help with the MTS machine, while being a great officemate prior to joining the lab permanently as staff.

Many students in the ORL have helped and taught me tremendously both as colleagues and some as friends: Connie Pagedas, Sylva Krizan, Jeff Meganck, Aaron Weaver, Mike Paschke, Amanda Thornton, Danese Joiner, Steve Roller, Grant Reeves,

Sivan Oyserman, Nefertiti Patrick-Boardley, and Ethan Daley. Without these individuals the lab would not have been as much fun.

The faculty members of the ORL have invaluable guided my learning and fate as a doctoral student. Richard Hughes graciously forwarded my email application for a research position in the lab to Barbara and Steve, creating my learning opportunity. Josh Miller helped me climb the steep learning curve of biology. Andrea Alford taught me proper flow hood etiquette, cell biology and was always there to answer any questions. Ken Kozloff was always available for a quick talk, or to give advice whether it was science or running related. He has broadened my orthopaedic view and taught me how to run fast.

I owe my thesis to all the faculty, staff and fellow students of the ORL and thank every one of you.

Laura Tesmer, Ingrid Peterson, Katya Christenson and Ken Kozloff have been tremendously helpful in editing this thesis on a very short notice. Thank you for unraveling my convoluted sentence structures.

Finally I would especially like to thank my family for their support. My family-in-law Jen, Mary, Mark, Janine and Dave, thank you for always being there and creating a wonderful oasis of relaxation away from my studies when I visited, whether in Denver, Muscatine, Rochester or Pittsburgh. My parents, Kaj and Søsse, have always supported me in my endeavors, from attending Herlufsholm boarding school as a ten-year-old boy, to leaving Denmark to go across the pond to Michigan. You believed in me, and for that I love you very, very much. My twin brother, Kristian, has always been my best friend and been there on the journey from the womb, through Herlufsholm, to the US, and into graduate school. I hope our trails will meet up again in Colorado!

Most of all I am grateful for my wonderful wife Sarah. You have supported me through my darkest times, and greatest achievements. You always make me smile, and help me up when I am down. You make the journey of my life seem effortless.

TABLE OF CONTENTS

LIST OF FIGURES

LIST OF TABLES

ABSTRACT

The risk of whole bone fracture in osteoporosis may be substantially increased as a result of microdamage accumulation in bone in conjunction with the associated remodeling that attempts to repair the damage. The risk may be increased as a result of age and disuse, which are hypothesized to alter remodeling in response to microdamage. Elucidating the effects of age and disuse on bone repair may provide clinically important insight into the relationship between microdamage accumulation and increased fracture risk in the elderly. The goals of this study were to experimentally determine the influence of age and mechanical usage on microdamage accumulation and repair.

A unique animal model was developed that enabled loading of distal femoral trabecular bone of rats in-vivo. Utilizing this model, older rats (compared with adults) demonstrated a reduced ability of bone to recover after damage and a reduction in the removal of microdamage.

For the second series of studies a hindlimb suspension system and four-point bending apparatus were developed to simulate disuse and induce tibial cortical microdamage. Utilizing these models, it was shown that disuse alters the bone's response to microdamage through a reduction in woven bone production and cessation of microdamage resorption. These results resemble the pattern of a stress fracture response.

Finally, it was shown that daily short-term weight-bearing during disuse rescued the targeted bone remodeling response following microdamage induction.

These findings suggest that individuals with severe activity reductions may further accumulate microdamage. Most importantly, while many studies have proposed that microdamage repair is triggered by cell apoptosis, our present results suggest this

mechanism may be insufficient without the stimulus associated with mechanical usage. In addition, the ability to rescue the remodeling response through intermittent physiologic loading provides support to early clinical evidence that moderate loading can reduce recovery time from stress fractures.

In aggregate, advanced age and disuse were shown to lead to a reduction in targeted remodeling associated with microdamage. This could potentially increase fracture risk due to potential microdamage accumulation. In addition, the importance of physiological loading to the process of microdamage repair suggests that the current clinical practice of limiting weight-bearing for the treatment of stress fractures should be reconsidered.

CHAPTER 1

INTRODUCTION

Osteoporotic fracture is a common and expensive healthcare problem, with 1.5 million fractures in the United States per year, at a cost of $60 billion annually in the U.S. by 2025 (Riggs and Melton 1995). Yet the factors responsible for susceptibility to fracture remain incompletely understood.

In order to identify and examine these factors, a thorough understanding of bone as a tissue is required. While bone is a marvelous tissue that serves many purposes within the human body, such as transmission of load and protection of organs, it is also an adaptive tissue. Through the processes of modeling and remodeling bone can change shape and adapt to new prolonged external loading scenarios (Wolff's Law), while also being capable of self renewal through replacement of old or damaged bone tissue.

In order for bone to adapt to external forces and to renew itself, choreography of many cells must take place. The major bone cells taking center stage in this performance are the osteoblast, the osteocyte, and the osteoclast. Osteoblasts are derived from mesenchymal stem cells and lay down new bone in the form of osteoid, which is later mineralized. As osteoid is laid down on existing bone tissue, some osteoblasts get engulfed and proceed to become osteocytes. These cells are embedded throughout

compact bone in small crevasses called lacunae and are connected to each other through canaliculi (Figure 1.1). Osteoclasts are derived from hematopoietic stem cells and digest bone by acidifying and dissolving underlying mineralized bone.

When bone adapts to external forces, osteoblasts and osteoclasts act independently (modeling) by adding and removing bone at independent sites to change the current shape of the loaded bone. When self renewal is necessary, osteoblasts and osteoclasts act together (remodeling) in what is termed a basic multicellular unit (BMU), where initial resorption of bone is followed locally by the generation of new bone by the osteoblasts (Figure 1.2) (Matsuo and Irie 2008).

When the symphony of the major bone cells is out of tune, skeletal pathologic conditions arise. During osteoporosis, for example, increased osteoclast activity in conjunction with decreased bone formation leads to reduced bone density and disruption of bone micro-architecture (Eriksen, Mosekilde et al. 1985; Arlot, Delmas et al. 1990). Osteopetrosis, on the other hand, causes an increase in bone density due to a lack of bone resorption by the osteoclasts (Marks 1984; Marks 1989). Sclerosteosis also causes an increase in bone density, but is caused by a deficiency of sclerostin, a protein secreted by the osteocytes that inhibits bone formation (Gardner, van Bezooijen et al. 2005). These three conditions lead to secondary effects such as increased fracture risk and hearing loss. Hence it is clear that understanding how the major bone cells behave, interact, live and die during modeling and remodeling can potentially improve the quality of life for future generations.

Background and significance

It has been proposed that whole-bone failure in osteoporosis may be a result of positive feedback between microdamage and the resulting remodeling that attempts to repair the damage (Burr, Forwood et al. 1997). Microdamage results in a loss of mechanical integrity of the bone tissue, followed by a potentially greater loss in continuum-level bone strength and/or stiffness due to resorption at the beginning of the remodeling cycle. The reduced stiffness and strength may result in further damage or overt failure at lower loads than those required in the original intact bone, resulting in a positive feedback process.

Hence whole bone fracture risk in osteoporosis may be substantially increased if normal remodeling in response to microdamage is altered. Common for most osteoporotic patients are geriatric related factors, such as age and disuse due to severe activity reductions. The effects of these factors on bone remodeling have yet to be discovered, but previous studies in the literature have shown possible clues.

The existence of microdamage has been shown to induce localized osteocyte apoptosis surrounding the individual microcracks (Verborgt, Gibson et al. 2000; Verborgt, Tatton et al. 2002). The localized apoptotic response has been suggested to be caused by hyperemia and the associated decrease in lacunocanalicular interstitial fluid flow (Muir, Sample et al. 2007).

Targeted remodeling in association with microdamage and subsequent osteocyte apoptosis has been observed in vivo (Burr, Martin et al. 1985; Burr and Martin 1993; Mori and Burr 1993; Bentolila, Boyce et al. 1998; Verborgt, Gibson et al. 2000; Lee,

Staines et al. 2002). However, the effect of age on targeted remodeling has not been previously observed in vivo.

Pilot studies have shown that fatigue damage impedes transport from the blood supply, depleting the areas downstream of the microdamage of molecular entities. These results suggest a link between interstitial fluid flow, mass transport, maintenance of osteocyte viability, and regulation of remodeling activity (Tami, Nasser et al. 2002).

Disuse hindlimb suspension models have been shown to decrease interstitial fluid flow due to decreased pressure gradients (Stevens, Meays et al. 2006), with several studies suggesting that convective transport by means of load-induced fluid flow may be necessary to provide sufficient transport of larger molecules such as proteins to and from osteocytes (Knothe Tate, Knothe et al. 1998; Knothe Tate, Niederer et al. 1998).

Based on what has been shown in the literature it is therefore evident that age and disuse could potentially have an effect on remodeling. Elucidating the effects of age and disuse on bone repair may therefore provide clinically important insight into the relationship between microdamage accumulation and increased fracture risk in the elderly.

Study aims and hypotheses

The purpose of this thesis is to investigate the effects of age and disuse on bone remodeling in response to induced microdamage. Following the introduction and verification of several animal models developed specifically for simulating disuse and inducing damage in trabecular and cortical bone, a combination of these models with

young and old animal cohorts will be used to answer the global hypotheses. The global hypotheses of this thesis are three fold:

1) Microdamage removal is significantly different between mature and old animals.
2) Disuse reduces targeted bone remodeling following microdamage.
3) Intermittent daily physiological loading can reverse the lack of target remodeling during disuse.

Chapter overview

To address these hypotheses, several animal models were developed and verified. Chapter 2 describes the development of a novel animal model utilizing a hydraulically loaded bone chamber to load existing distal femoral trabecular bone of rats. Reproducibility of microdamage induction is demonstrated and the model is subsequently implemented in an adult and old cohort to examine the effect of age on remodeling.

Chapter 3 describes the development and verification of animal models for inducing microdamage in cortical bone and simulating disuse. Specifically, two non-invasive tibia loading models are described, verified, and tested, and based on a set criteria, a final microdamage model is presented. The development and verification of a hindlimb suspension system capable of inducing similar disuse effects as seen in the literature is also presented.

The animal models developed in chapter 3 are utilized in chapter 4 to examine the effects of disuse on bone remodeling in response to microdamage in an adult cohort of

animals. Using the same setup as in chapter 4, chapter 5 examines the effects of daily short-term weight bearing during disuse on targeted remodeling.

Taken together the results presented in chapter 2, 4 and 5 indicate the effects of age and disuse on bone remodeling in response to induced microdamage.

As of the submission of this dissertation, chapter 2 has been published (Waldorff, Goldstein et al. 2007), while chapters 4 and 5 are in preparation.

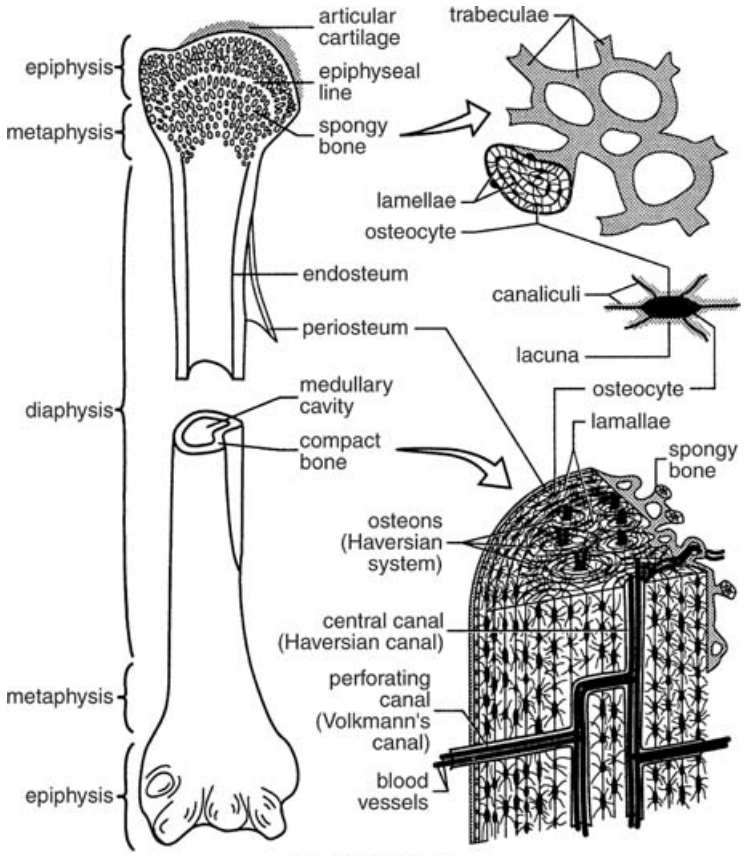

Figure 1.1. Bone structure

Illustration taken from http://media.wiley.com/Lux/84/21784.nfg001.jpg

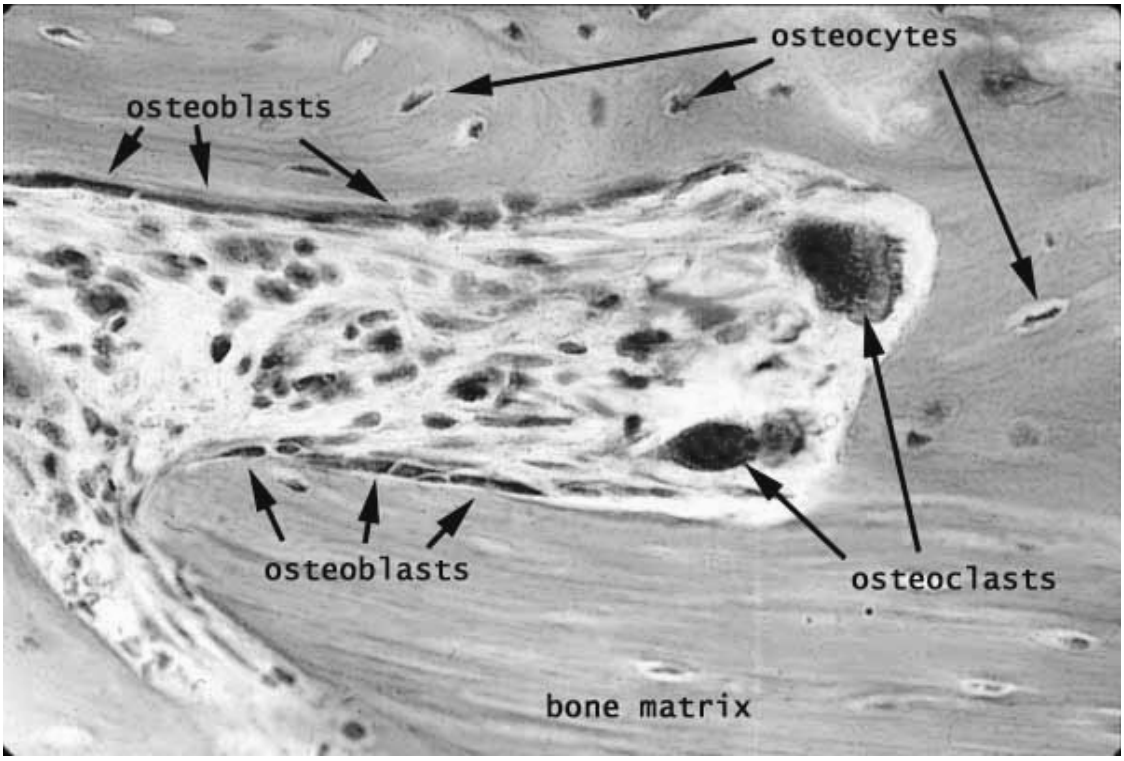

Figure 1.2. Basic multicellular unit (BMU)

Image taken from http://www.siumed.edu/~dking2/ssb/images/remodel.jpg

References

Arlot, M. E., P. D. Delmas, et al. (1990). "Trabecular and endocortical bone remodeling in postmenopausal osteoporosis: comparison with normal postmenopausal women." Osteoporos Int **1**(1): 41-9.

Bentolila, V., T. M. Boyce, et al. (1998). "Intracortical remodeling in adult rat long bones after fatigue loading." Bone **23**(3): 275-81.

Burr, D. B., M. R. Forwood, et al. (1997). "Bone microdamage and skeletal fragility in osteoporotic and stress fractures." J Bone Miner Res **12**(1): 6-15.

Burr, D. B. and R. B. Martin (1993). "Calculating the probability that microcracks initiate resorption spaces." J Biomech **26**(4-5): 613-6.

Burr, D. B., R. B. Martin, et al. (1985). "Bone remodeling in response to in vivo fatigue microdamage." J Biomech **18**(3): 189-200.

Eriksen, E. F., L. Mosekilde, et al. (1985). "Trabecular bone resorption depth decreases with age: differences between normal males and females." Bone **6**(3): 141-6.

Gardner, J. C., R. L. van Bezooijen, et al. (2005). "Bone mineral density in sclerosteosis; affected individuals and gene carriers." J Clin Endocrinol Metab **90**(12): 6392-5.

Knothe Tate, M. L., U. Knothe, et al. (1998). "Experimental elucidation of mechanical load-induced fluid flow and its potential role in bone metabolism and functional adaptation." Am J Med Sci **316**(3): 189-95.

Knothe Tate, M. L., P. Niederer, et al. (1998). "In vivo tracer transport through the lacunocanalicular system of rat bone in an environment devoid of mechanical loading." Bone **22**(2): 107-17.

Lee, T. C., A. Staines, et al. (2002). "Bone adaptation to load: microdamage as a stimulus for bone remodelling." J Anat **201**(6): 437-46.

Marks, S. C., Jr. (1984). "Congenital osteopetrotic mutations as probes of the origin, structure, and function of osteoclasts." Clin Orthop Relat Res(189): 239-63.

Marks, S. C., Jr. (1989). "Osteoclast biology: lessons from mammalian mutations." Am J Med Genet **34**(1): 43-54.

Matsuo, K. and N. Irie (2008). "Osteoclast-osteoblast communication." Arch Biochem Biophys **473**(2): 201-9.

Mori, S. and D. B. Burr (1993). "Increased intracortical remodeling following fatigue damage." Bone **14**(2): 103-9.

Muir, P., S. J. Sample, et al. (2007). "Effect of fatigue loading and associated matrix microdamage on bone blood flow and interstitial fluid flow." Bone **40**(4): 948-56.

Riggs, B. L. and L. J. Melton, 3rd (1995). "The worldwide problem of osteoporosis: insights afforded by epidemiology." Bone **17**(5 Suppl): 505S-511S.

Stevens, H. Y., D. R. Meays, et al. (2006). "Pressure gradients and transport in the murine femur upon hindlimb suspension." Bone **39**(3): 565-72.

Tami, A. E., P. Nasser, et al. (2002). "The role of interstitial fluid flow in the remodeling response to fatigue loading." J Bone Miner Res **17**(11): 2030-7.

Verborgt, O., G. J. Gibson, et al. (2000). "Loss of osteocyte integrity in association with microdamage and bone remodeling after fatigue in vivo." J Bone Miner Res **15**(1): 60-7.

Verborgt, O., N. A. Tatton, et al. (2002). "Spatial distribution of Bax and Bcl-2 in osteocytes after bone fatigue: complementary roles in bone remodeling regulation?" J Bone Miner Res **17**(5): 907-14.

Waldorff, E. I., S. A. Goldstein, et al. (2007). "Age-dependent microdamage removal following mechanically induced microdamage in trabecular bone in vivo." Bone **40**(2): 425-32.

CHAPTER 2

AGE-DEPENDENT MICRODAMAGE REMOVAL FOLLOWING MECHANICALLY INDUCED MICRODAMAGE IN TRABECULAR BONE IN VIVO

Summary

In order to examine the potential age-related response of trabecular bone to microdamage, a novel animal model utilizing a bone chamber to load existing distal femoral trabecular bone of rats was developed. Fifteen 8-month-old (mature) and fifteen 24-month-old (old) Fischer Brown Norway rats underwent bilateral insertion of the bone chamber. After a 3-week recovery period, one leg per animal underwent damage-inducing loading. Double fluorochrome labeling was used to identify microcracks induced by loading. A greater crack density was found in loaded trabecular bone than in corresponding unloaded control bone at day 0 in both age groups (mature n=5, old n=4). At day 35 post loading, older rats (n=3) had greater crack density (suggesting little removal of microcracks), whereas younger rats (n=5) had no difference between loaded and unloaded limbs, suggesting induced microcracks were removed. The difference in bone volume fraction between the loaded and unloaded limb were significantly different at 21 and 35 days post loading when comparing the old with the mature rats. The data suggest a reduced ability of bone to recover after damage in the older rats. The damage-inducing capabilities of the animal model were demonstrated using double fluorochrome

labeling in vivo for detection of microcracks. The results indicate that removal of microdamage is altered with age.

Introduction

Although osteoporotic fracture is a common (1.5 million fractures in the United States per year) and expensive ($60 billion annually in the U.S. by 2025) healthcare problem (Riggs and Melton 1995), the factors responsible for susceptibility to fracture remain incompletely understood. Bone mineral density is strongly associated with bone strength, but its use to assess fracture risk in all patients has been limited (Recker 1989; Kanis 2002). Although the potential addition of geometric and material properties (at multiple hierarchical levels) may improve fracture risk predictions significantly, unexplained factors remain (McCreadie and Goldstein 2000).

For example, it has been proposed that whole-bone failure in osteoporosis may be a result of positive feedback between microdamage and the resulting remodeling that attempts to repair the damage (Burr, Forwood et al. 1997). Microdamage results in a loss of mechanical integrity of the trabecular bone tissue, followed by a potentially greater loss in continuum-level trabecular bone strength and/or stiffness due to resorption at the beginning of the remodeling cycle. The reduced stiffness and strength may result in further damage or overt failure at lower loads than those required in the original intact bone, resulting in a positive feedback process.

Microdamage has been observed in cortical bone as a natural occurrence (Frank, Ryan et al. 2002; Lee, Mohsin et al. 2003), and due to damage inducing loads ex vivo (Burr, Forwood et al. 1997; Lee, Arthur et al. 2000; Lee, O'Brien et al. 2000; O'Brien,

Taylor et al. 2002; Danova, Colopy et al. 2003; O'Brien, Taylor et al. 2003) and in vivo (Burr, Martin et al. 1985; Stover, Martin et al. 1993). Similarly, microdamage has been observed in trabecular bone both naturally (Norrdin, Robinson et al. 1993; Wenzel, Schaffler et al. 1996) and due to loading ex vivo (Fyhrie and Schaffler 1994; Arthur Moore and Gibson 2002; Moore and Gibson 2003). Prior studies have reported the results of in vivo loading of trabecular bone using non-damaging loads to evaluate the effects of mechanical stimulation and to study mechanical signal transduction in cancellous bone (Guldberg, Caldwell et al. 1997; Moalli, Caldwell et al. 2000; Morgan, Yang et al. 2004). Microdamage has previously been induced in trabecular bone in vivo in studies examining the effect of impact loading of rabbit knee joints on cartilage degeneration (Radin, Parker et al. 1973). To our knowledge, microdamage due to direct loading of trabecular bone has not previously been induced experimentally in vivo.

Although targeted remodeling in association with microdamage has been observed in vivo (Burr, Martin et al. 1985; Burr and Martin 1993; Mori and Burr 1993; Bentolila, Boyce et al. 1998; Verborgt, Gibson et al. 2000), the effect of age on targeted remodeling has not been observed in vivo previously. One study (Martin, Stover et al. 1996) has shown a decrease in density of active basic multicellular units with age; however, the effect on targeted remodeling due to damage could not be determined.

As part of a program designed to examine the response of trabecular bone under a variety of conditions such as age and microgravity, we developed a novel animal model in which the distal femoral trabecular bone of rats is loaded in vivo under controlled parameters. The aim of this study was to demonstrate reproducibility in microdamage

induction and to test the hypothesis that microdamage removal is not significantly different over time between mature and old animals.

Materials and Methods

The study involved two phases. First, microcomputed tomography and mechanical testing were conducted to characterize the properties of the trabecular bone of the distal femur and to assist in determining the loading parameters needed to induce damage in trabecular bone in the rat distal femoral metaphysis. Second, the novel rat bone chamber was implanted bilaterally on the distal femora of experimental animals. After three weeks, the trabecular bone of one femur per animal underwent cyclic damage-inducing loading (designated as day 0). Morphological features of the trabecular bone were quantified at days 0, 21 and 35, whereas microcracks were quantified at days 0 and 35. Each step is described in greater detail below. This work was approved by the University Committee on Use and Care of Animals at the University of Michigan.

Microcomputed tomography characterization of rat trabecular bone

In order to assist in estimating the loading parameters needed to induce damage, the bone volume fraction of Fischer Brown Norway rats was obtained at 8 and 23 months of age. The femora from six rats in each age group were dissected of soft tissue and scanned using a cone-beam microcomputed tomography system (GE Healthcare BioSciences). Trabecular bone volume fraction was obtained from the distal femoral trabecular bone region of each bone using routine protocols and MicroView software (GE Healthcare BioSciences).

In situ mechanical characterization of rat trabecular bone

In order to assist in estimating the loading parameters needed to induce damage in the trabecular bone of the distal femur, six femurs from 8-month-old male Fischer Brown Norway rats were dissected free of soft tissue. The distal third of each bone was removed and embedded in methacrylate with the lateral surface of the bone exposed. To simulate the surgical procedures described below, a 3.2-mm diameter circular window of cortical bone was removed near the distal end of the femur (just proximal to the growth plate) using an end mill. The exposed trabecular bone was loaded in compression to failure at a constant displacement rate of 1 mm/s utilizing a cylindrical loading head (simulating the bone chamber piston geometry) attached to a servohydraulic testing machine (858 Mini Bionix II, MTS System, Eden Prairie, MN). The displacement of the loading head was monitored using an external LVDT (100 MHR, Lucas Schavitts, Hampton, VA, USA), while load was recorded using a 5-lb load cell (Sensotec, Columbus, OH, USA) in series with the actuator. Using the Test Star IIs system (version 2.4, MTS, Eden Prairie, MN), load and displacement were recorded at a sampling rate of 2000 Hz. The following parameters were calculated from the load-displacement curves (Figure 2.1) using custom functions in MATLAB (The Mathworks Inc. Natick, MA): stiffness, yield load, displacement at yield load, ultimate load, displacement at ultimate load and displacement ratio (displacement at ultimate load/displacement at yield load). Stiffness was defined as the slope of the force–displacement curve in the linear region that contained the maximum slope. Yield load was determined using a secant modulus method. The intersection of the best-fit line in the linear portion of the force–displacement curve (used for the stiffness calculation) with the x axis was determined. The secant modulus for each

point on the load-deflection curve was defined as the slope of the line joining the point with the intersection of the bestfit line and the x axis. The load at the first point beyond the linear region for which the secant modulus was reduced by at least 10% from the stiffness of the linear region was considered the yield load.

In vivo loading of rat trabecular bone

Fifteen mature (8 months) and fifteen old (24 months) male Fischer Brown Norway rats underwent bilateral insertion of the rat bone chamber (Figure 2.2) on the lateral surface of each distal femur. The rat bone chamber measures 10.3 mm in length, 3.8 mm in width and 8.1 mm in height. It consists of 3 parts: the chamber, a piston with an ethylene-propylene o-ring (Apple Rubber Products Inc., Lancaster, NY) and a set screw with matching ethylene-propylene o-ring (Figure 2.2). The chamber itself is manufactured as a one-piece assembly using a CNC machine. The bottom portion of the piston casing ensures that the chamber is properly located and that the piston will directly load trabecular bone. The chamber and piston (diameter 2.1 mm) are made from commercially pure titanium.

A custom hydraulic loading device used to activate the piston within the chamber consists of a Macintosh IIci computer, running a custom program in LabView 2.2.1, connected to a microprocessor-based servopump equipped with a pressure transducer feedback circuit (Goldstein, Matthews et al. 1991; Guldberg, Caldwell et al. 1997; Moalli, Caldwell et al. 2000). The input parameters of the hydraulic loading system include shape of waveform, number of loading cycles, load amplitude (in volts) and wave frequency.

Due to manufacturing tolerances in the diameters of the o-rings and o-ring grooves in the piston, each chamber/piston pair has a unique relationship between the controller input setting (which determines the hydraulic pressure in the line leading to the chamber) and the resulting piston force. Therefore, each chamber/piston pair was calibrated in a small testing rig prior to surgery to obtain a calibration curve between the controller input and the piston force measured by a small load transducer in the rig. Thereby, the required load (6 N for the 8-month-old rats, and 3 N for the 24-month-old rats) can be translated into a specific input parameter value for each chamber/piston pair, ensuring that the correct load on the trabecular bone was obtained. In addition, each pair was re-calibrated following retrieval to validate correct loading amplitudes. Resulting loads within 10% of the desired load (i.e., 3±0.3 N and 6±0.6 N) were considered acceptable.

During surgery, chambers were inserted bilaterally in each animal. A 1.5-cm lateral parapatellar incision was made extending from the distal femur to just distal of the insertion of the patellar tendon on the tibia. The patella was gently dislocated to expose the distal femur. The lateral aspect of the distal femur was then further exposed using periosteal elevation. A custom mill bit was used to remove a 3.2-mm diameter cortical bone window, thus exposing the trabecular bone proximal to the growth plate. The base of the bone chamber hardware was then fixed to the bone using two small stainless steel bolts passed through predrilled 1.2 mm holes, co-locating the piston with the area of removed cortical bone (Figure 2.3). A specialized drill guide and template were used to ensure precise and repeatable positioning of the implant. The patella was repositioned, and soft tissue was closed in layers around the implant using resorbable sutures and skin

staples. Postoperative radiographs verified placement of the device in regions of sufficient trabecular bone density. Immediately following surgery, animals were injected intraperitoneally with the fluorochrome calcein (10 mg/kg) to label any existing or surgically produced microcracks. The animals were allowed full weight-bearing and normal cage activity immediately following surgery and appeared fully weight bearing within 2 h.

After a recovery period of 3 weeks, each animal was anesthetized and a small incision was made in the skin immediately on top of each chamber. The set-screw was carefully removed, and a CNC-machined fitting attached to a hydraulic hose was carefully screwed into place at the top of each chamber. The hydraulic line from one of the two chambers was randomly chosen and connected to the computer-controlled hydraulic loading system (Goldstein, Matthews et al. 1991; Guldberg, Caldwell et al. 1997; Moalli, Caldwell et al. 2000). The chosen leg then underwent a trapezoidal loading regime of 1000 cycles at 0.5 Hz (rise time: 0.4 s; upper plateau: 0.6 s; return time: 0.4 s; lower plateau: 0.6 s). The chambers in 8-month animals were activated to develop a load of 6 N on the trabecular bone, while 24-month animals were loaded at 3 N. The amplitude and ratio of these loads were chosen to impart equivalent continuum strain, described below. Equivalent continuum strain was selected with the assumption that equal strain would result in equal damage. This assumption is not critical because the true test of the selected load magnitudes is whether the amount of damage (which was later measured) is equal in the two groups. From the in situ mechanical characterization of rat trabecular bone (described above), we chose a load of 6 N for the mature animals to target a load of approximately 10% of the ultimate load. The load for the old animals was

then estimated using the bone volume fraction data described above and two methods: scaling the load directly to the bone volume fraction and using Goulet's relationship (Goulet, Goldstein et al. 1994) between trabecular bone volume fraction and modulus, solving the following equation for $F_{max,\ 24\ months}$

$$\varepsilon = \frac{\sigma}{E} = \frac{F_{\max,24month} / A}{MOD_{22,BV/TV,24month}} = \frac{F_{\max,8month} / A}{MOD_{22,BV/TV,8month}}$$

where ε is strain; σ=F/A is stress; A is the area of the piston (equal for both age groups), Fmax is the maximum load applied and MOD22,BV/TV is the modulus of the bone calculated from Goulet et al. (Goulet, Goldstein et al. 1994) based on the bone volume fraction of the trabecular bone. Scaling the load directly to the bone volume fraction suggested a load of approximately 3 N for the old animals, whereas that using Goulet's equation (Goulet, Goldstein et al. 1994) resulted in a load of approximately 1 N for the old animals. A preliminary study (Waldorff, Goldstein et al. 2005) and the results of this study support the choice of 3 N and 6 N loads to provide equivalent damage in both ages. During loading, the animals were injected intraperitoneally with the fluorochrome Xylenol orange (90 mg/kg) to label induced microcracks.

During and following surgery, five animals from the old group were lost due to insufficient trabecular bone beneath the piston as a result of milling the holes too deep, or a poor match in piston location between contralateral legs. From the 8-month group, five animals each were euthanized at days 0, 21 and 35 following loading. Four, three and three animals from the 24-month group were euthanized at days 0, 21 and 35, respectively. Femora were carefully dissected free of soft tissue and scanned on a microcomputed tomography (microCT) system (GE Healthcare Systems) at 18 μm/voxel

(Figure 2.4). The reconstructed three-dimensional images were thresholded into bone and non-bone voxels. On each of the images, a cylindrical volume, with a diameter equal to that of the piston and 1 mm in length, was identified just beneath the piston and in line with the direction of loading. Trabecular bone architectural parameters for this region of interest were determined using a custom analysis program and a commercially available voxel analysis software package (MicroView v.1.18). The following parameters were measured: bone mineral density (BMD, mg/cm3), bone volume fraction (BV_TV, mm3/mm3), bone surface-to-volume ratio (BS_BV, mm^{-1}), trabecular plate number (TB_N, mm^{-1}), trabecular plate thickness (TB_TH, mm), trabecular plate separation (TB_SP, mm), mean intercept length (MIL, mm), degree of anisotropy (DA, mm/mm) and connectivity (EulN_Vol, mm^{-3}).

After microCT scanning, the specimens were dehydrated and embedded undecalcified in poly methyl methacrylate to quantify microcracks (for days 0 and 35). Specimens were sectioned at 500 μm transverse to the longitudinal axis of the femur using a Buehler Isomet low speed diamond blade saw. Sections that intersected the location of the piston were individually mounted to slides and polished. The specimens were then examined using appropriate fluorescence filters. Microcracks labeled with calcein or both calcein and xylenol orange were determined to be unrelated to loading because they were labeled at surgery. Distinct microcracks labeled with just xylenol orange were considered microdamage induced by loading and were measured and counted. The following parameters were measured throughout the entire trabecular bone region of each section: number of microcracks (#), bone trabecular area (B.Ar., mm2), microcrack density (Cr.Dn., #/mm2), microcrack mean length (Cr.Le., μm) and

microcrack surface density (Cr.S.Dn., μm/mm2). All of these parameters represent the total values from the entire loaded or unloaded region, i.e., the data from all sections that intersected the location of the piston were grouped together. Approximately 36 mm2 were quantified for each bone, using 3 or 4 consecutive sections.

To compare loaded to contralateral unloaded sides, paired t-tests were used. Unpaired t-tests were used for comparisons between age groups and between groups at different time points. Significance was defined as $p \leq 0.05$. The analysis was performed using SPSS statistical software (SPSS, Chicago, IL).

Results

Mechanical properties were successfully obtained from all femurs loaded to failure (Table 2.1), resulting in an average yield load of 50.7 N.

Bone volume fraction for 8-month animals was 0.213 ± 0.022 mm^3, whereas that for 23-month animals was 0.110 ± 0.013 mm^3.

The output force for each chamber/piston pair was found to vary little between pre-surgery calibration and post-retrieval tests (within ±10% of desired load). Chamber/piston pairs subjected to extended calibration times maintained loads within ±2.5% of the desired load for up to 1000 cycles at 0.5 Hz. All animals gained or maintained weight within 10 days of surgery.

The microCT results showed that the difference in bone volume fraction between the loaded and unloaded leg becomes significantly different between the two age groups by day 21 (Figure 2.5, Table 2.2). The old group has a lower bone volume fraction in the loaded side than the unloaded (control) side. The eight-month animals, in contrast, have a

higher (non-significant) bone volume fraction on the loaded side. At day 35 this significant pattern is sustained. A similar pattern is seen for bone mineral density and trabecular plate number. The inverse pattern is seen for trabecular spacing, as expected based on the bone volume fraction. None of the other morphological parameters demonstrated statistically significant differences between the two age groups.

Several differences were noted in microcracks between the loaded and unloaded sides (Figure 2.6, Table 2.3). Loaded trabecular bone had greater crack density than corresponding unloaded controls at day 0 (the day of loading) in both age groups. The difference in crack density between loaded and unloaded sides was similar in both age groups at day 0, indicating that similar crack densities were induced by loading in both age groups. This demonstrates that the loads used to induce microdamage in the two groups generated essentially equivalent microdamage in their respective age groups. In mature animals, there was no significant difference in crack density between loaded and unloaded sides at day 35, suggesting resorption of induced microcracks. The old rats had significantly more damage in the loaded limbs than control limbs at day 35. The magnitude of the difference in crack density between loaded and unloaded limbs is not significantly different between days 0 and 35, indicating that little resorption or repair of induced microdamage took place over the course of 35 days in old animals.

Discussion

Bone chambers have been developed for various species to evaluate mechanical stimulation and signal transduction in trabecular bone (Guldberg, Caldwell et al. 1997; Moalli, Caldwell et al. 2000; Morgan, Yang et al. 2004; Tägil, Åstrand et al. 2004; Tägil,

Åstrand et al. 2004). This study presents a newly developed rat bone chamber designed to load existing trabecular bone in vivo. The model distinguishes itself from others (Goldstein, Matthews et al. 1991; Guldberg, Caldwell et al. 1997; Moalli, Caldwell et al. 2000) in that existing trabecular bone, not newly formed bone, is loaded. To the best of our knowledge, this is also the first time microdamage due to direct loading of trabecular bone has been induced experimentally in vivo.

Because this model is invasive, regional acceleratory phenomenon (RAP) (Frost 1983) might have an effect on the turnover of the trabecular bone underneath the piston. The animals in this study were given 3 weeks to recover from surgery, allowing time for the RAP to decrease. In addition, all animals underwent bilateral insertion of the chamber, adhering to Frost's advice (Frost 1983) describing the need for a bilateral surgical control to separate RAP effects from experimental effects. Despite these precautions, RAP may change the remodeling response to microdamage compared to what would be seen in a non-surgical model. In addition, age may alter the timing or characteristics of the RAP response. The individual data (Table 2.2) show that the bone volume fraction in the unloaded side increases slightly (but not significantly) from day 0 to day 35 for both age groups, which may indicate that RAP is still somewhat present. Previous studies have shown that microdamage in bone can be detected using a wide array of fluorochromes (Lee, Arthur et al. 2000; Lee, O'Brien et al. 2000; Arthur Moore and Gibson 2002; O'Brien, Taylor et al. 2002; Lee, Mohsin et al. 2003; Moore and Gibson 2003; O'Brien, Taylor et al. 2003). With the exception of one study (Stover, Martin et al. 1993), they have been performed ex vivo (Lee, Mohsin et al. 2003). Fluorescent double labeling in vivo for detection of microcracks was utilized in this

study. This method allowed a clear distinction between pre-existing microdamage and that due to the surgical procedures and subsequent induced microdamage. Previous studies have shown that microdamage accumulates with age (Schaffler, Choi et al. 1995; Wenzel, Schaffler et al. 1996; Burr, Forwood et al. 1997). Damage accumulation has been hypothesized to be a factor that increases bone fragility with age (Burr, Forwood et al. 1997). Studies have suggested that as an individual ages, there may be a point when bone microdamage accumulates faster than it can be repaired through remodeling (Schaffler, Choi et al. 1995). This idea is supported by investigators that have shown that a decline in lacunae density is associated with an increase in microcrack density (Vashishth, Verborgt et al. 2000). However, these studies were unable to determine if bone tissue alterations or changes in repair processes occur first.

The trabecular bone architecture results indicate a pattern of significant and sustained higher bone volume fraction in unloaded limbs than loaded limbs in the old rats compared to the mature rats, which may support the hypothesis of positive feedback between microdamage and resulting targeted remodeling (Burr, Forwood et al. 1997). The hypothesis has its origin in microdamage that results in a loss of mechanical integrity of the trabecular bone tissue, followed by a potentially greater loss in continuum-level trabecular bone strength and/or stiffness due to resorption at the beginning of the remodeling cycle. The reduced stiffness and strength will result in further damage or overt failure at lower loads than those required in the original intact bone, resulting in a positive feedback process.

The bone volume fraction may be directly influenced by the loading protocol. Continuous cyclic loading could cause a slight compression of the bone tissue due to

damage accumulation. Thus, the difference in bone volume fraction between the loaded and unloaded leg could be artificially increased. Because both age groups are loaded at a similar tissue strain level, this phenomenon is likely present in both age groups. This is the reason this study compares age groups to each other, as opposed to simply comparing the difference in bone volume fraction between the loaded and unloaded side to zero.

The microcrack results appear to indicate that removal of mechanically induced microdamage has decreased or been lost with age. This is supported by the significant difference in microcrack density between the loaded and unloaded side at day 35 in old rats, with no difference in mature rats. Although the difference in crack density between limbs has not significantly changed from day 0 to day 35 for the old rats, removal of microdamage might take a considerably longer time in this age group. Whether the ability to remove induced microdamage has completely ceased, has been substantially decreased or has been substantially delayed with age cannot be determined in this study. It can be concluded, however, that the removal of microcracks is altered with age. Future studies will investigate if this is due to a change in targeted remodeling or to stochastic remodeling in general.

The significant difference in bone volume fraction (between loaded and unloaded sides) between age groups at days 21 and 35 could cause one to suspect that the change in difference in crack density between the loaded and unloaded leg could have been artificially induced due to a change in trabecular area in the sections examined. However, two arguments speak against this suggestion. First, because the analysis is based on density (number of cracks per area) this measure is not affected if bone is removed in an unbiased manner. In fact, the number of absolute cracks decreases significantly in the

loaded limbs between days 0 and 35 for both mature and old rats, indicating that removal of cracks occurs in both age groups. Second, should the decreased bone volume fraction have led to increased bone fragility and thus cause more microcracks to develop in agreement with the positive feedback hypothesis (Burr, Forwood et al. 1997), then the additional microcracks would not have been marked with the secondary fluorochrome label, and thus not counted. Therefore, the conclusion that an alteration of the repair response (i.e., removal of microcracks, perhaps by targeted remodeling) occurs with age appears to be supported.

In conclusion, this paper has demonstrated the successful implementation of the rat bone chamber, which has proven capable of inducing trabecular microdamage in vivo. Morphological and histological results suggest that removal of mechanically induced microdamage is altered with age. In addition, fluorescent double labeling in vivo for detection of microcracks has been successfully implemented.

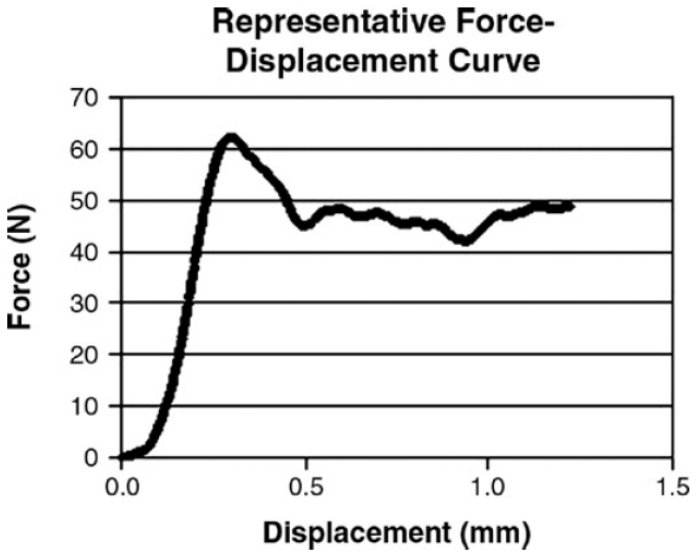

Figure 2.1. Representative force-displacement curve for in situ mechanical test simulating bone chamber function

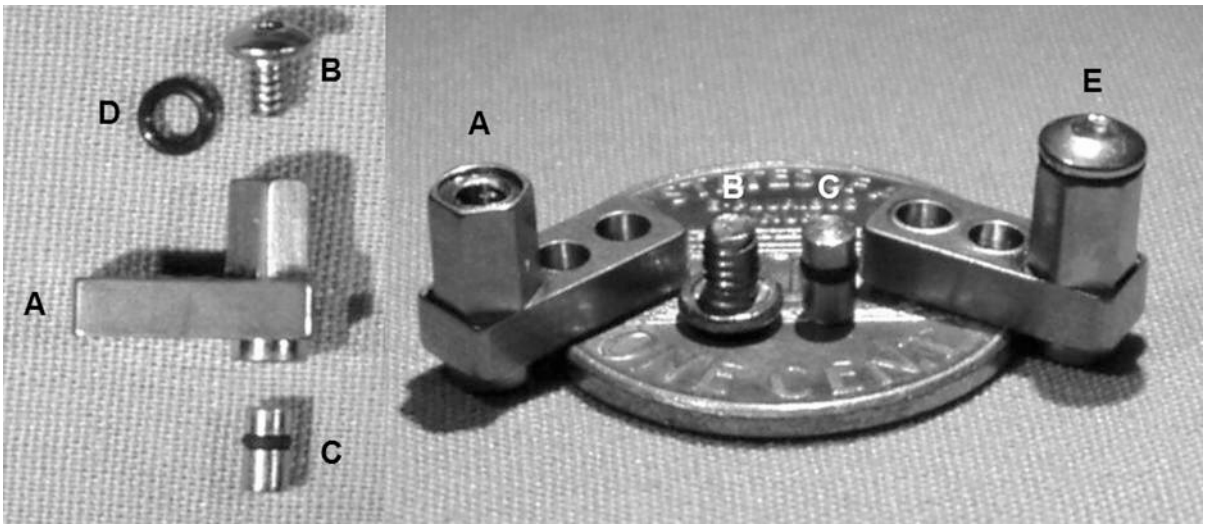

Figure 2.2. Rat bone chamber hardware

A: Rat bone chamber
B: Set screw
C: Piston
D: Set screw o-ring
E: Assembled rat bone chamber on top of a penny

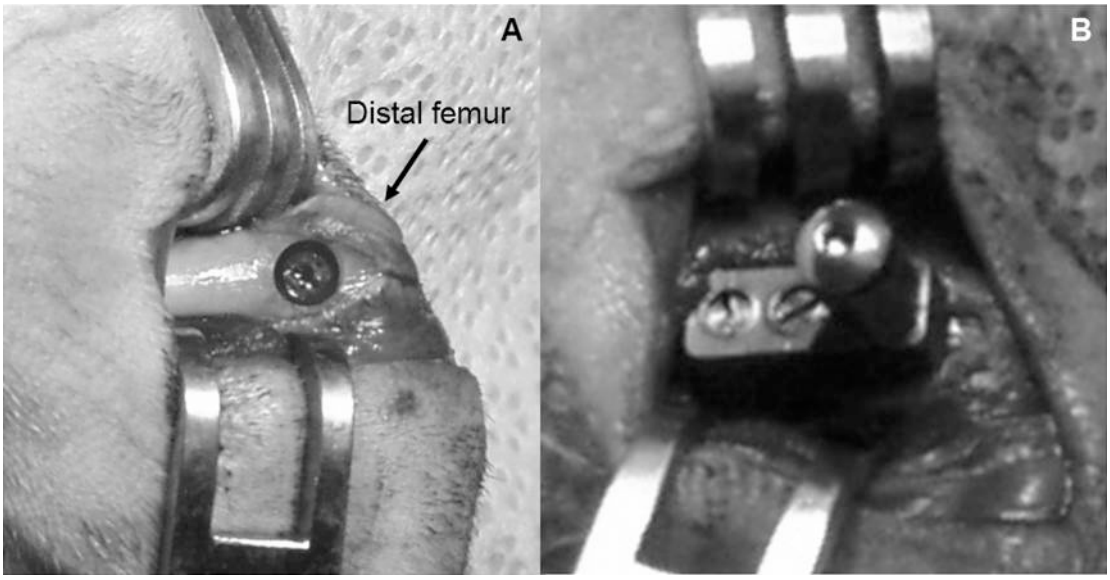

Figure 2.3. Surgical technique

A: Distal femur with cortical window removed for piston
B: Distal femur with implant attached prior to surgical closure

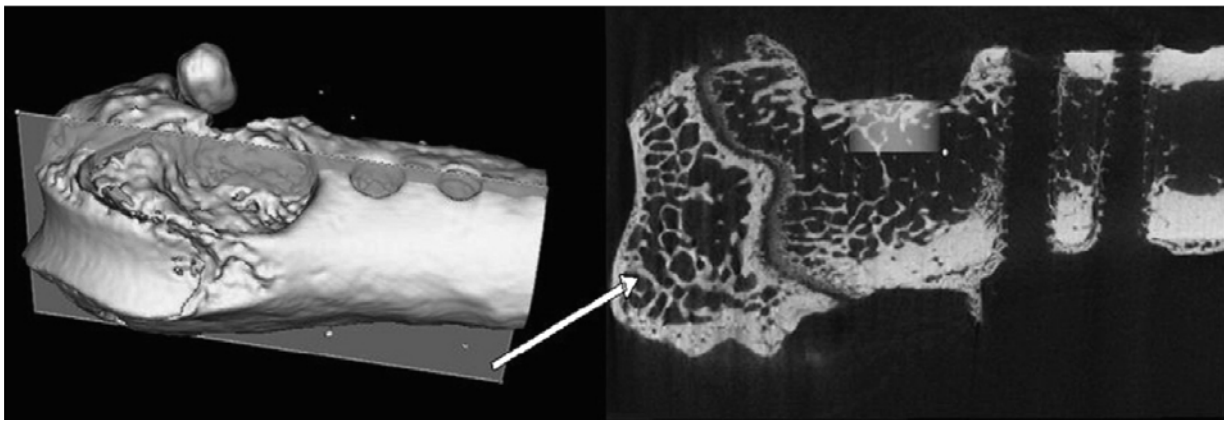

Figure 2.4. MicroCT images of femur after removal of bone chamber

Left: Distal part of femur showing removal of cortex where piston contacts trabecular bone, and two holes where bolts attach chamber to femur.
Right: Longitudinal view of femur at plane shown in left image showing location of the rat bone chamber. The region of interest used for morphological measurements is indicated by the shaded region.

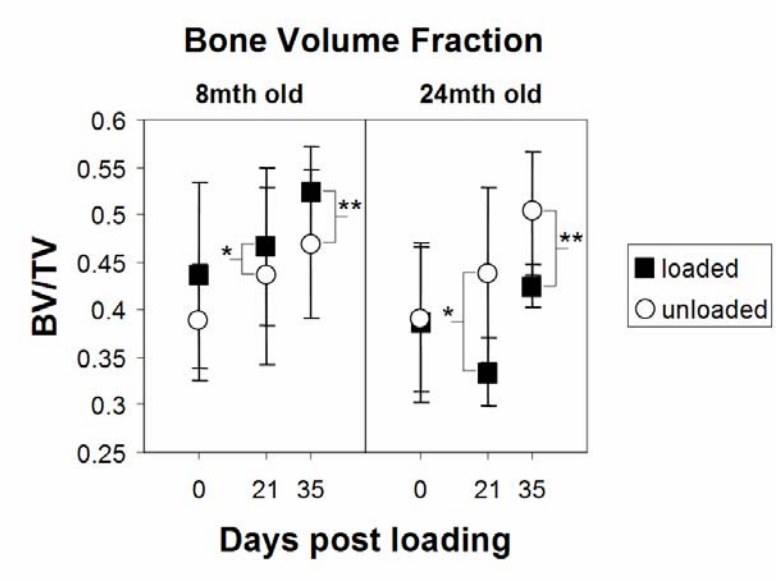

Figure 2.5. Bone volume fraction

Significance ($p \leq 0.05$) of unpaired t-test comparing the bone volume fraction (difference between the loaded and unloaded leg) between age groups at the same time point is indicated by either a single or double asterisk. Error bars indicate standard deviation.

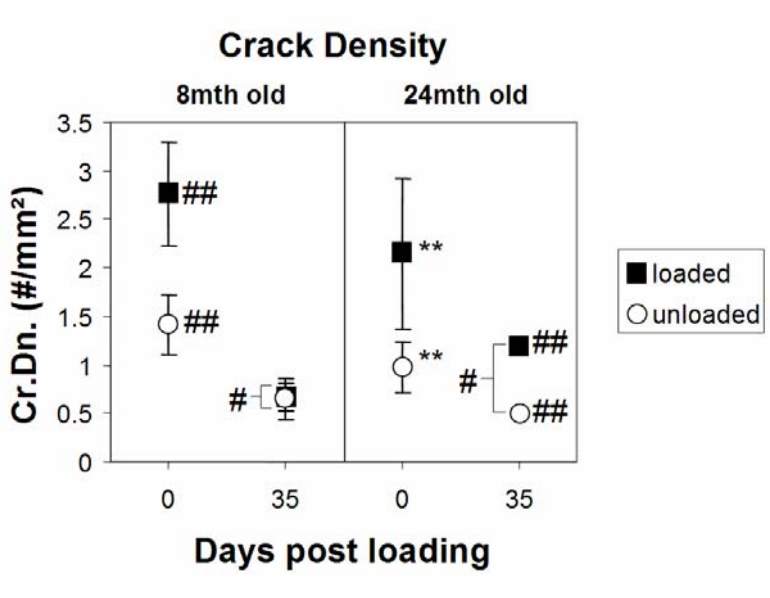

Figure 2.6. Crack density

Significance of paired t-test comparing loaded to unloaded side is indicated by the following symbols: **p≤0.05, ##p≤0.01. Significance of unpaired t-test comparing crack density (difference between the loaded and unloaded leg) between age groups at the same time point is indicated by the following symbols: #p≤0.01. Error bars indicate standard deviation.

Properties	Mean	S.D.
Stiffness, Pa	548.52	120.83
Yield load, N	50.73	23.27
Yield displacement, mm	0.925	0.151
Ultimate load, N	67.71	16.23
Ultimate displacement, mm	1.08	0.08
Yield ratio, mm/mm	1.18	0.11

Table 2.1. Mechanical test results for in situ mechanical testing of trabecular bone

			Property	BMD	BV_TV	BS_BV	TB_N	TB_TH	TB_SP	EulN_Vol
8 month group	Day 0	Loaded side	Mean	460.72	0.44	22.74	4.77	0.09	0.12	55.79
			S.D.	56.37	0.10	4.92	0.36	0.02	0.03	48.51
		Unloaded side	Mean	413.96	0.39	23.23	4.46	0.09	0.14	76.28
			S.D.	48.08	0.06	1.40	0.48	0.01	0.03	12.38
		Delta (loaded - unloaded)	Mean	46.76	0.05	-0.49	0.31	0.00	-0.02	-20.49
			S.D.	90.28	0.14	5.88	0.68	0.02	0.05	55.52
	Day 21	Loaded side	Mean	483.23	0.47	18.12	4.13	0.11	0.13	59.82
			S.D.	62.70	0.08	3.11	0.41	0.02	0.03	14.90
		Unloaded side	Mean	459.01	0.44	19.43	4.07	0.11	0.14	53.50
			S.D.	67.92	0.09	4.32	0.38	0.02	0.03	21.54
		Delta (loaded - unloaded)	Mean	24.22	0.03	-1.31	0.06	0.01	-0.01	6.32
			S.D.	49.76	0.07	3.31	0.30	0.02	0.02	14.04
	Day 35	Loaded side	Mean	538.23	0.52	15.14	3.94	0.13	0.12	43.19
			S.D.	42.81	0.05	1.56	0.32	0.01	0.02	14.83
		Unloaded side	Mean	489.43	0.47	18.23	4.22	0.11	0.13	51.41
			S.D.	69.49	0.08	2.24	0.40	0.02	0.03	5.43
		Delta (loaded - unloaded)	Mean	48.80	0.05	-3.09	-0.28	0.02	-0.01	-8.21
			S.D.	68.49	0.06	2.96	0.43	0.02	0.02	18.02
24 month group	Day 0	Loaded side	Mean	395.31	0.39	21.68	4.10	0.09	0.15	78.98
			S.D.	63.46	0.08	3.70	0.42	0.01	0.03	24.36
		Unloaded side	Mean	401.20	0.39	21.33	4.06	0.10	0.15	69.88
			S.D.	53.14	0.08	3.52	0.26	0.02	0.03	14.37
		Delta (loaded - unloaded)	Mean	-5.89	0.00	0.35	0.04	0.00	0.00	9.10
			S.D.	40.23	0.07	3.96	0.17	0.02	0.02	21.50
	Day 21	Loaded side	Mean	374.31	0.33	17.20	2.90	0.12	0.24	30.72
			S.D.	48.68	0.04	2.33	0.68	0.02	0.07	13.47
		Unloaded side	Mean	449.98	0.44	16.00	3.43	0.13	0.17	41.00
			S.D.	87.79	0.09	2.04	0.30	0.02	0.04	16.00
		Delta (loaded - unloaded)	Mean	-75.67	-0.10	1.20	-0.53	-0.01	0.07	-10.28
			S.D.	46.29	0.07	3.37	0.48	0.03	0.05	29.26
	Day 35	Loaded side	Mean	453.95	0.43	14.86	3.16	0.14	0.18	10.91
			S.D.	20.34	0.02	1.49	0.39	0.01	0.03	9.40
		Unloaded side	Mean	511.80	0.50	14.34	3.60	0.14	0.14	25.25
			S.D.	41.26	0.06	1.32	0.57	0.01	0.04	5.71
		Delta (loaded - unloaded)	Mean	-57.85	-0.08	0.52	-0.44	0.00	0.04	-14.34
			S.D.	60.19	0.09	0.88	0.80	0.01	0.07	12.99

Table 2.2. Specific microCT results for loaded and unloaded side of each age group

			Property	Cr.Dn.	Cr.Le.	Cr.S.Dn.
8 month group	Day 0	Loaded side	Mean	2.76	23.55	65.48
			S.D.	0.53	2.73	17.61
		Unloaded side	Mean	1.41	20.14	28.73
			S.D.	0.31	6.27	11.46
		Delta (loaded - unloaded)	Mean	1.35	3.41	36.74
			S.D.	0.40	6.30	9.42
	Day 35	Loaded side	Mean	0.67	20.43	13.53
			S.D.	0.14	4.05	3.70
		Unloaded side	Mean	0.64	18.10	11.88
			S.D.	0.21	4.37	5.09
		Delta (loaded - unloaded)	Mean	0.02	2.32	1.65
			S.D.	0.19	5.99	4.43
24 month group	Day 0	Loaded side	Mean	2.14	35.12	72.01
			S.D.	0.77	6.03	16.59
		Unloaded side	Mean	0.98	33.29	33.35
			S.D.	0.26	5.60	13.91
		Delta (loaded - unloaded)	Mean	1.16	1.84	38.66
			S.D.	0.75	7.42	13.75
	Day 35	Loaded side	Mean	1.19	31.26	37.26
			S.D.	0.09	1.54	1.44
		Unloaded side	Mean	0.48	40.29	19.21
			S.D.	0.04	15.69	6.86
		Delta (loaded - unloaded)	Mean	0.71	-9.03	18.06
			S.D.	0.07	14.22	7.90

Table 2.3. Specific histology results for loaded and unloaded side of each age group

References

Akhter, M. P., D. M. Raab, et al. (1992). "Characterization of in vivo strain in the rat tibia during external application of a four-point bending load." J Biomech **25**(10): 1241-6.

Arthur Moore, T. L. and L. J. Gibson (2002). "Microdamage accumulation in bovine trabecular bone in uniaxial compression." J Biomech Eng **124**(1): 63-71.

Bentolila, V., T. M. Boyce, et al. (1998). "Intracortical remodeling in adult rat long bones after fatigue loading." Bone **23**(3): 275-81.

Burr, D. B., M. R. Forwood, et al. (1997). "Bone microdamage and skeletal fragility in osteoporotic and stress fractures." J Bone Miner Res **12**(1): 6-15.

Burr, D. B. and R. B. Martin (1993). "Calculating the probability that microcracks initiate resorption spaces." J Biomech **26**(4-5): 613-6.

Burr, D. B., R. B. Martin, et al. (1985). "Bone remodeling in response to in vivo fatigue microdamage." J Biomech **18**(3): 189-200.

Danova, N. A., S. A. Colopy, et al. (2003). "Degradation of bone structural properties by accumulation and coalescence of microcracks." Bone **33**(2): 197-205.

Frank, J. D., M. Ryan, et al. (2002). "Aging and accumulation of microdamage in canine bone." Bone **30**(1): 201-6.

Frost, H. M. (1983). "The regional acceleratory phenomenon: a review." Henry Ford Hosp Med J **31**(1): 3-9.

Fyhrie, D. P. and M. B. Schaffler (1994). "Failure mechanisms in human vertebral cancellous bone." Bone **15**(1): 105-9.

Goldstein, S. A., L. S. Matthews, et al. (1991). "Trabecular bone remodeling: an experimental model." J Biomech **24 Suppl 1**: 135-50.

Goulet, R. W., S. A. Goldstein, et al. (1994). "The relationship between the structural and orthogonal compressive properties of trabecular bone." J Biomech **27**(4): 375-89.

Guldberg, R. E., N. J. Caldwell, et al. (1997). "Mechanical stimulation of tissue repair in the hydraulic bone chamber." J Bone Miner Res **12**(8): 1295-302.

Kanis, J. A. (2002). "Diagnosis of osteoporosis and assessment of fracture risk." Lancet **359**(9321): 1929-36.

Lee, T. C., T. L. Arthur, et al. (2000). "Sequential labelling of microdamage in bone using chelating agents." J Orthop Res **18**(2): 322-5.

Lee, T. C., S. Mohsin, et al. (2003). "Detecting microdamage in bone." J Anat **203**(2): 161-72.

Lee, T. C., F. J. O'Brien, et al. (2000). "The nature of fatigue damage in bone." Int J Fatigue **22**: 847-53.

Martin, R. B., S. M. Stover, et al. (1996). "In vitro fatigue behavior of the equine third metacarpus: remodeling and microcrack damage analysis." J Orthop Res **14**(5): 794-801.

McCreadie, B. R. and S. A. Goldstein (2000). "Biomechanics of fracture: is bone mineral density sufficient to assess risk?" J Bone Miner Res **15**(12): 2305-8.

Moalli, M. R., N. J. Caldwell, et al. (2000). "An in vivo model for investigations of mechanical signal transduction in trabecular bone." J Bone Miner Res **15**(7): 1346-53.

Moore, T. L. and L. J. Gibson (2003). "Fatigue microdamage in bovine trabecular bone." J Biomech Eng **125**(6): 769-76.

Morgan, T. G., X. Yang, et al. (2004). In vivo loading causes mechanical property adaptation in cancellous bone. Orthopaedic Research Society, San Francisco, CA.

Mori, S. and D. B. Burr (1993). "Increased intracortical remodeling following fatigue damage." Bone **14**(2): 103-9.

Norrdin, R. W., H. T. Robinson, et al. (1993). Evaluation of microdamage in canine trabecular bone. Orthopaedic Research Society, San Francisco, CA.

O'Brien, F. J., D. Taylor, et al. (2002). "An improved labelling technique for monitoring microcrack growth in compact bone." J Biomech **35**(4): 523-6.

O'Brien, F. J., D. Taylor, et al. (2003). "Microcrack accumulation at different intervals during fatigue testing of compact bone." J Biomech **36**(7): 973-80.

Radin, E. L., H. G. Parker, et al. (1973). "Response of joints to impact loading. 3. Relationship between trabecular microfractures and cartilage degeneration." J Biomech **6**(1): 51-7.

Recker, R. R. (1989). "Low bone mass may not be the only cause of skeletal fragility in osteoporosis." Proc Soc Exp Biol Med **191**(3): 272-4.

Riggs, B. L. and L. J. Melton, 3rd (1995). "The worldwide problem of osteoporosis: insights afforded by epidemiology." Bone **17**(5 Suppl): 505S-511S.

Schaffler, M. B., K. Choi, et al. (1995). "Aging and matrix microdamage accumulation in human compact bone." Bone **17**(6): 521-25.

Stover, S. M., R. B. Martin, et al. (1993). In vivo labeling of microdamage in cortical bone tissue. Orthopaedic Research Society, San Francisco, CA.

Tägil, M., J. Åstrand, et al. (2004). Alendronate prevents subchondral collapse in mechanically loaded osteochondral grafts. Orthopaedic Research Society, San Francisco, CA.

Tägil, M., J. Åstrand, et al. (2004). Single dose zolendronate treatment of the donor reduces bone resorption and increases bone formation in bone transplants. Orthopaedic Research Society, San Francisco, CA.

Vashishth, D., O. Verborgt, et al. (2000). "Decline in osteocyte lacunar density in human cortical bone is associated with accumulation of microcracks with age." Bone **26**(4): 375-80.

Verborgt, O., G. J. Gibson, et al. (2000). "Loss of osteocyte integrity in association with microdamage and bone remodeling after fatigue in vivo." J Bone Miner Res **15**(1): 60-7.

Waldorff, E. I., S. A. Goldstein, et al. (2005). Age-dependent trabecular bone response to damage-inducing loads using a novel animal model. ASME Summer Bioengineering Conference, Vail, CO.

Wenzel, T. E., M. B. Schaffler, et al. (1996). "In vivo trabecular microcracks in human vertebral bone." Bone **19**(2): 89-95.

CHAPTER 3

DEVELOPMENT AND VERIFICATION OF ANIMAL MODELS USED FOR MICRODAMAGE INDUCTION IN BONE AND SIMULATION OF DISUSE

Summary

In order to examine the effect of disuse on the remodeling in response to microdamage, several animal models had to be developed to meet specific criteria.

The four-point bending setup fulfilled the criteria for a successful animal model for inducing microdamage in vivo and was chosen for the subsequent experiments. It proved capable of inducing significant amounts of fatigue microdamage for hindlimb suspended and weight bearing animals without causing any damage to the joints of the tibia.

The developed hindlimb suspension model also fulfilled its set criteria for a successful disuse animal model. It proved capable of inducing similar effects as seen in the literature, where the disuse condition of the hindlimbs resulted in a decrease in bone formation and an increase in bone resorption.

Common for both chosen animal models was the maintenance of animal health indicated by maintenance of body weight and normal cage activity.

Introduction

As it was shown in chapter 2, older rats have a reduced ability to recover trabecular bone mass after damage and that removal of microdamage is altered with advancing age. This could potentially increase the risk of whole bone fracture associated with alterations in microdamage-related remodeling. The positive feedback loop between increases in microdamage and subsequent remodeling could be enhanced by secondary effects associated with aging such as disuse, caused by a decrease in physical activity and/or infirmity. Hence not only is microdamage repair in general reduced in elderly individuals, but the cessation of activity with increased age could possibly aid in this reduction. Considering this, sporadic periods of activity intermixed with times of disuse might make individuals prone to microdamage accumulation, and therefore increase fracture risk. The influence of disuse on bone remodeling could therefore potentially provide clinically important insight into the relationship between microdamage accumulation and increased fracture risk in the elderly.

In order to study the effects of disuse on bone remodeling it was necessary to develop and verify animal models capable of simulating disuse and inducing microdamage in-vivo. This chapter presents the development and verification of animal models capable of fulfilling these criteria. The work presented for all the developed animal models was approved by the University Committee on Use and Care of Animals at the University of Michigan.

Criteria for Microdamage Animal Model

The criteria for loading animal models for microdamage induction were as follows:

1. Must be applicable with hindlimbs (tibia/femur) since the animal models available for inducing disuse conditions (without casting) are intended for hindlimb disuse only.
2. Must be able to induce repeatable amounts of microdamage non-invasively within a moderate amount of time (1-2 hours).
3. Cannot cause any alterations in animal behavior post loading, while animal must regain full usage of the hindlimbs shortly after loading.

While the animal model presented in chapter 2 proved capable of inducing trabecular microdamage in-vivo, a non-invasive loading model was sought for a higher throughput of experimental animals. The majority of studies in the field of bone microdamage have used the ulna fatigue model developed by Bentolila et. al. (Bentolila, Boyce et al. 1998) in order to examine the effects of microdamage in the cortical bone of the ulnae in vivo (Verborgt, Gibson et al. 2000; Verborgt, Tatton et al. 2002; Danova, Colopy et al. 2003; Follet, Li et al. 2007). However, because the animal models available for inducing disuse conditions without casting are intended for hindlimb disuse only, the ulna fatigue model was inappropriate for the intended studies.

Two models intended for non-damaging loading of the tibiae were found in the literature. The first model was developed for axial loading of the murine tibiae (Fritton, Myers et al. 2001; De Souza, Matsuura et al. 2005; Fritton, Myers et al. 2005; Fritton,

Myers et al. 2005). The second animal model employed four-point bending of the murine tibiae in order to examine the effects of non-damaging loading on skeletal adaptation (Turner, Akhter et al. 1991; Akhter, Raab et al. 1992; Forwood and Turner 1995; Forwood, Bennett et al. 1998; Inman, Warren et al. 1999; Robling, Burr et al. 2001). Neither animal models had been utilized for microdamage induction before but were both deemed appropriate for further development and verification.

Materials and Methods for Microdamage Animal Models

Axial Tibia Loader

Following an adaptation of the Fritton model (Fritton, Myers et al. 2001), which loads the tibia while it is horizontal, tibia ankle and knee holders were manufactured to allow for loading of the tibia vertically (Figure 3.1). This created a loading setup where the load-controlled vertical translation of a loading beam (Figure 3.1A) could be recorded using a standard PC with instrumentation software (LabView 6.1, National Instruments). Prior to any testing, the loading beam was calibrated with known weights in order to obtain the required force/input voltage relationship for the load control parameters (Figure 3.2).

In order to determine the medial microstrain vs. applied force relationship, five tibiae from 8-month old Fisher Brown Norway rats from the Rat Bone Chamber study (Chapter 2) were thawed and soft tissue removed. Strain gauges (EA-XX-015DJ-120/LE, Vishay Micro-Measurements) were attached at the mid-diaphysis of the medial and lateral side of the tibiae with cyanoacrylate. After calibrating the strain gauges and placing the tibiae in the tibia loader, a load/unload pattern was applied by manually

moving the stage to which the load beam was attached. Once 120N was reached, the load was reduced to zero. The resulting output was recorded by the LabView software.

Subsequently two 8-month old Fisher Brown Norway were obtained in order to carry out the identical experiment in-vivo. Once anesthetized with an isoflurane (2%):oxygen balance, strain gauges were attached to the medial side bilaterally, and tibiae were loaded similarly to the ex-vivo experiment.

To determine if microdamage could be induced three tibiae from 8-month old Fisher Brown Norway rats were loaded ex-vivo with a load of -50.5N (-2000 microstrain medially) for 1000 cycles at 1Hz. Two additional tibiae served as unloaded controls. Following loading, soft tissue was carefully removed from the tibiae, which were dehydrated, stained with basic fuchsin, and embedded undecalcified in polymethylmethacrylate (PMMA) to quantify microcracks. Specimens were sectioned at 500 μm transverse to the longitudinal axis of the tibia using a Buehler Isomet low speed diamond blade saw. Sections from the mid-diaphysis were individually mounted to slides and polished. The specimens were then examined using light microscopy.

The experiment was repeated with four tibiae (three loaded, one unloaded), with a loading magnitude of -101.0N (-4000 microstrain medially) for 1000 cycles at 1Hz.

Finally to test the damage capabilities in vivo, three 8-month old Fisher Brown Norway rats were anesthetized and loaded in vivo with a load of -101.0N (-4000 microstrain medially) for 1000 cycles at 1Hz.

Four-Point Bending

The four-point bending model developed by Turner et. al. (Turner, Akhter et al. 1991) fulfilled the requirements of non-invasive loading of the cortical bone of the tibia, while not applying loads to the knee or ankle joints. Using the same basic setup as the axial tibia loader (load beam, computer, and software), 4-point bending pads were manufactured with the same dimensions as the Turner et. al. model (Turner, Akhter et al. 1991). In addition, they were made to fit the load beam and corresponding opposing base slot used for the axial tibia loader (Figure 3.4). The four-point bender has two configurations: 1) Bending configuration (Figure 3.4(2)) where the tibia will undergo bending when loaded, and 2) Non-bending configuration (Figure 3.4(3)) where the tibia will not undergo bending when loaded (used for control legs).

Before commencing, the load beam was calibrated again using the new setup.

Strain gauges were applied ex-vivo to the medial and lateral side of the mid-diaphysis of three tibiae from 8-month old Sprague-Dawley rats. The tibiae were loaded in two ways in the bending configuration: first with the upper loading pads (Figure 3.4B) at the medial side of the tibia, and second with the upper loading pads at the lateral side of the tibia. These initial tests were designed to determine which arrangement provided the maximum strain at the mid-diaphysis while minimizing any muscle indentations from the loading pads. The tibiae were also loaded in a similar fashion in the non-bending (control) configuration.

One 8-month old Sprague Dawley rat was anesthetized and loaded in vivo with a load of -75.6N (-4000 microstrain laterally) for 1000 cycles at 1Hz (bending for left leg, non-bending for right leg) in order to determine if loading would adversely affect the

muscle tissue or animal mobility post loading. Once loaded the rat was observed for 24 hours. At sacrifice the muscle tissue was grossly examined and the tibiae were dehydrated, stained with basic fuchsin, embedded in PMMA, and sectioned along the entire length of the tibia. The sections were examined using light microscopy.

In order to determine if hindlimb suspension (discussed later in this chapter) would affect the strain-applied force relationship, six 8-month old Sprague Dawley rats were split into two groups: 1) Hindlimb suspension (HS) for 14 days (n=3), and 2) Normal weight bearing (WB) for 14 days (n=3). At day 14, all rats were anesthetized and bi-lateral strain gauges were placed in-vivo on the lateral side of the tibiae, 8mm proximal to the tibia-fibula junction. The slope of the lateral strain vs. applied force relationship using the bending configuration was determined for each leg.

In order to determine the initial effects of hindlimb suspension in combination with loading, two 8-month old Sprague Dawley rats were hindlimb suspended for 14 days. At day 14 the rats were anesthetized and the left tibiae were loaded for 7200 cycles at 2Hz using a sinusoidal waveform, with a peak load of 107.8N (ΔLoad = 50.2N), resulting in a maximum lateral strain of -7,000$\mu\varepsilon$ (Figure 3.8). Post loading, the animals were hindlimb suspended for an additional 3 days to observe any behavioral changes due to the loading, and subsequently euthanized. At sacrifice the legs were dehydrated, stained with basic fuchsin, embedded in PMMA, and sectioned at the region of interest (center at 8 mm proximal to tibia/fibula junction, with a total length of 5 mm). The sections were examined using confocal microscopy,

Results for Microdamage Animal Models

Axial Tibia Loader

The average of the five loading ex-vivo tests to determine the medial microstrain vs. applied force relationship revealed the following average relationship:

$$\mu\varepsilon_{medial} = 20.25 \cdot F_{Applied\ Load\ (N)}$$

The resulting average medial microstrain vs. applied force relationship for the in-vivo test was determined to be (Figure 3.3):

$$\mu\varepsilon_{medial} = 39.585 \cdot F_{Applied\ Load\ (N)}$$

Microdamage examinations from the second ex-vivo loading revealed that no microdamage had been induced due to loading. However the third ex-vivo loading revealed qualitatively significant damage accumulation at the mid-diaphysis due to the loading (Figure 3.5).

In all three animals from the second in-vivo loading the patella tendon and knee ligaments were obliterated within the first 100 cycles of loading. Once patella dislocation was observed the animals were euthanized.

Four-Point Bending

The initial load beam calibration using the new setup, resulted in an applied force to input voltage relationship of:

$$F_{Applied\ Load\ (N)} = -37.296 \cdot V_{(load)}$$

From the average strain-force results from the first ex-vivo loading (Figure 3.6) it was determined that the lateral side had the highest με/N slope. Loading from the lateral side resulted in the least amount of muscle indentations at both the lateral and medial side

of the tibia, making it the most desirable way to load the tibiae. Finally, the work of Diab et. al. (Diab and Vashishth 2005) have shown that linear microcracks occur predominantly at locations with compressive stress (tensile stress leads to more diffuse damage). Hence, loading the tibia with the upper loading pads at the lateral side in order to generate the highest amount of linear microdamage is the optimal loading configuration.

The average strain-force results from the first ex-vivo loading using the non-bending (control) configuration (Figure 3.7), revealed that a load of 75.6N, which would result in -4000 microstrain laterally in the bending configuration, would give a medial and lateral strain level of 734.6 and -402.4 microstrain, respectively. The strain level was deemed sufficiently low (below maximum normal physiological levels of loading) that no damage could occur at the region of interest, and the loading configurations were approved to be tested in-vivo.

Normal cage activity was observed following the second in-vivo loading, indicating that using the four-point bender in-vivo would not significantly alter mobility. In addition no muscle indentations due to the loading pads were identified during dissection. It was also found that despite no damage initiation within the region of interest (center of the upper loading pads) while using the non-bending configuration, microdamage was found at the contact points of the upper loading pads.

The third in-vivo loading (Table 3.1) revealed that no significant difference was found between the hindlimb suspended (HS) and weight bearing (WB) groups in the lateral strain vs. applied force relationship. Hence a slope of -65.15με/N was chosen, resulting in a lateral strain vs. applied force relationship of:

$$\mu\varepsilon_{lateral} = -64.93 \cdot F_{Applied\ Load\ (N)}$$

From strain-gauge results from the third in-vivo loading, it was also determined that the tibia would reach ultimate failure at approximately -10,000με (Table 3.2).

The fourth in-vivo loading revealed that significant damage could be induced at the region of interest compared to the non-loaded control tibia (Figure 3.9) for hindlimb suspended animals (determined qualitatively). In addition no abnormal behavior was observed post loading.

Discussion for Microdamage Animal Models

The tibia loader experiments showed that axial loading at -2000 microstrain in-vivo is not harmful to the knee, but no damage can be induced at the mid-diaphysis with this load. Loading at -4000 microstrain ex-vivo results in significant microdamage at the mid-diaphysis; when applying similar loads in vivo, however, the patella is dislocated and the knee ligaments were destroyed. There is no evidence in the literature for murine in-vivo loading of more than 2000 microstrain medially at the mid-diaphysis using the tibia loader. Microdamage could possibly be induced at -2000 microstrain medially if the number of cycles was higher (>25,000). However this contradicts the set criteria (would take >3.5 hours) and the use of the tibia loader was abandoned.

The four-point bending animal model, however, proved capable of inducing significant amounts of fatigue microdamage for hindlimb suspended and weight bearing animals without causing any damage to the joints of the tibia. It was shown that hindlimb suspended and weight bearing animals did not display any adverse behavioral changes post loading and regained full usage of the hindlimbs within hours of loading.

Due to the fulfillment of all the set criteria for a successful microdamage animal model, the four-point bending setup was chosen to be utilized for the subsequent experiment presented in chapter 4 and 5.

Loading parameters for subsequent experiments

The four-point bending setup showed that 14 days of hindlimb suspension did not change the lateral strain vs. applied force relationship compared to animals having undergone 14 days of weight bearing. This resulted in a lateral strain vs. applied force relationship of:

$$\mu\varepsilon_{lateral} = -64.93 \cdot F_{Applied\ Load\ (N)}$$

This relationship was used for all the loading parameters in the subsequent experiments.

Due to the evidence of microdamage induction (and the possible effects) at the loading pad locations for the non-bending (control) loading setup, it was determined that the non-bending (control) loading setup would be abandoned. The control legs for the subsequent experiments would henceforth not be loaded.

Finally based on the in-vivo strain-gauge results for the four-point bending setup, it was determined that the tibia would reach ultimate failure at approximately -10,000με. Based on this information a strain level of -7,000με at the lateral side (107.8N applied force) was chosen as the parameter for subsequent loading.

Criteria for Disuse Animal Model

The criteria for a successful disuse animal model were as follows:

1. Must be able to induce a state of disuse of the hindlimbs of a rat for a period of up to 5 weeks.
2. Hindlimb suspended animals may not lose more than 20% of their starting weight (i.e. weight at the beginning of hindlimb suspension) at any point during hindlimb suspension.
3. After assimilation weight must be maintained for up to 5 weeks. General animal health must be maintained throughout this period.
4. Hindlimb suspension must be able to induce similar physiological changes as shown in the literature for previous hindlimb suspension models (i.e. increased resorption and decreased formation).

Hindlimb suspension models were developed (Wronski and Morey-Holton 1987; Morey-Holton and Globus 2002) in order to induce a disuse condition with effects on bone similar to what had been observed in a microgravity environment in space where bone formation decreased and bone resorption increased (Caillot-Augusseau, Vico et al. 2000; Vico, Collet et al. 2000; Bikle, Sakata et al. 2003; Sakata, Halloran et al. 2003). For the purpose of developing a model that would work within our laboratory setting the specific details for our hindlimb suspension system mirrored the rat hindlimb suspension system used by Midura et. al. (Midura, Su et al. 2006). After developing the animal model, subsequent verification would ensure that our model fulfilled the set criteria for a successful disuse animal model.

Materials and Methods for Disuse Animal Model

In order to simulate a murine disuse setting in which physiological loading of the hindlimbs would be removed, the hindlimb suspension model by Morey-Holton et al. was adapted (Wronski and Morey-Holton 1987; Morey-Holton and Globus 2002). Specifically, the hindlimb suspension model was technically made to be similar to the variation of the Morey-Holton model used by Midura et. al. (Midura, Su et al. 2006). The hindlimb suspension model (Figure 3.10) developed at the Orthopaedic Research Laboratories utilizes a 4 inch tall steel frame (Figure 3.10A), which is compatible with a Specific Pathogen-Free (SPF) rated standard ventilated #3 rat box. This allows for easy stacking on a standard non-ventilated rack. The size of the steel frame allows it to be fitted between the base and the top of the rat box, while maintaining SPF protocol guidelines. The steel frame has a center beam (Figure 3.10B) through which a swivel (Figure 3.10D) with an attached plastic tail holder (Figure 3.10E) can be held in place with a cotter pin (Figure 3.10C). This allows for easy mounting and dismounting of the hindlimb suspended rat within the cage. The plastic tail holder was manufactured in PVC-material on a semi-automatic CNC-machine, with dimensions taken from the Midura model.

The following protocol was developed for long term hindlimb suspension of the rats 3-4 inches from the base of the tail without causing injury: anesthetize rat; swipe tail with alcohol wipes; apply compound benzoin tincture; apply two strips of heavy Moleskin (Seneca Medical) with double sided tape on top to the anterior and posterior part of the tail; wrap with standard gauze, followed by VetWrap (Kendall); insert wrapped tail into plastic tail holder and secure it with VetWrap; hindlimb suspend rat

(Figure 3.11). Once hindlimb suspended, the rats were fed ad libitum using in-cage water bottle and standard rat chow dispersed on the cage floor (Figure 3.11B).

In order to determine if the developed hindlimb suspension model would fulfill the set criteria based on previous hindlimb suspension models (Wronski and Morey-Holton 1987; Morey-Holton and Globus 2002), male 6-month old adult Sprague Dawley rats (500-700g) were obtained from Harlan. Animals were allowed to acclimate to our animal facility for at least 3 days before being included in the experiment. The procedures used in this study were approved by the University Committee on Use and Care of Animals at the University of Michigan.

Animals were housed in individual non-ventilated cages in a temperature-controlled room (68-72˚F) with a 12:12-hour light-dark cycle. Water and rat chow were provided ad libitum.

At day 0, forty-one (41) animals were anesthetized, had blood samples taken from the jugular vein, and were either hindlimb suspended (n=31) or left weight bearing (n=10). Animals were inspected twice daily until sacrifice. Any animal showing symptoms of acclimation difficulties indicated by severe weight loss (loss of more than 20% of weight at day 0) were removed from the study. Animals were weighed at day 0, 14, 21, 28 and 35. Animals were euthanized at day 0 (Control, n=5), day 14 (n=4), day 21 (n=6), day 28 (n=7), and day 35 (n=14). Five animals were kept weight bearing for 35 days (Control day 35, n=5).

In addition to the base line blood draw at day 0, blood draws were done for all available animals at days 21, 28, and 35. Subsequent to all blood draws, samples were spun down and serum was collected and stored at -80˚C for future analysis.

For the day 35 and Control day 35 groups, animals were also injected intraperitoneally with the fluorochrome calcein (10 mg/kg) nine and two days before sacrifice to label the growing periosteal surface.

At sacrifice, tibiae and femora were carefully dissected free of soft tissue. Tibiae were scanned on a microcomputed tomography (microCT) system (GE Healthcare Systems) and the resulting data was reconstructed with a voxel size of 25 μm. Morphological parameters were calculated for two regions of interest (ROI) for the tibiae: 1) Cortical region with a length of 4mm with its center located 8mm proximal to the tibia-fibula junction; 2) Trabecular region starting at the proximal growth plate, with a length of 10% of the distance between the proximal growth plate and the tibia-fibula junction. Bone architectural parameters for these ROIs were determined using a custom analysis program and a commercially available voxel analysis software package (MicroView v.2.2). The following parameters were calculated: cortical and marrow area for the cortical region, bone mineral density (BMD), tissue mineral density (TMD) and bone volume fraction (BVF) for trabecular region.

After microCT scanning, the left tibiae and left femora from day 35 and Control day 35 groups were dehydrated and embedded undecalcified in polymethylmethacrylate to quantify cortical bone formation rate (BFR). Specimens were sectioned at 500 μm transverse to the longitudinal axis of the bone using a Buehler Isomet low speed diamond blade saw. Four sections were taken from the cortical ROI for the tibiae and the mid-diaphysis for the femur (half-way between the distal growth plate and the greater trochanter). The sections were individually mounted to slides and polished. One section per bone was randomly selected and examined using appropriate fluorescence filters at a

magnification of 100x, determining the average distance between the double fluorescent labels at the periosteal surface (based on 20 randomly chosen location at the lateral, medial, anterior and posterior side (5 locations each)). The average BFR was determined based on the time between intraperitoneally fluorochrome injections and the measured average distance between the double fluorescent labels at the periosteal surface for the selected sections of the control day 35 and HS day 35 groups.

Upon complete collection of all serum samples, samples were thawed and serum TRACP5b (RatTRAP, SBA Sciences) and OCN (Rat Osteocalcin, #BT-490, Biomedical Technologies Inc.) were measured by ELISA (Absorbance measured at 450nm (OCN) and 405nm (TRACP5b)), in order to determine relative systemic expression of markers of bone resorption and formation, respectively.

Results for Disuse Animal Model

Due to severe animal weight loss and/or acclimation problems (such as continued tail biting), 4 animals had to be removed from the study, resulting in final groups of: day 0 Control (n=10), day 14 (n=2), day 21 (n=5), day 28 (n=6), day 35 (n=14), and Control day 35 (n=5).

MicroCT results (Figure 3.12A,B) indicated that the cortical and marrow area for the cortical ROI did not change significantly over the course of 35 days of hindlimb suspension. However a trend of a decrease for the cortical area, and an increase for the marrow area were found. No trends were found for any groups at day 14, 21, and 28 for any other bone parameters. The trabecular ROI showed no significant differences of the tissue mineral density for any of the groups, while the bone mineral density decreased

significantly for HS day 35 vs. Control day 35 (Figure 3.13A). This result corresponded to the bone volume fraction of the trabecular ROI, which also showed a significant decrease for HS day 35 vs. Control day 35 (Figure 3.13B).

Serum levels of osteocalcin decreased significantly at day 35 for hindlimb suspended animals compared to control (Figure 3.14A). In addition a corresponding decreasing trend within the HS group itself was observed when compared to HS day 0 (HS day 21 ($p=0.18$), HS day 35 ($p=0.07$)). Rat TRACP5b serum levels increased significantly for HS day 21 and 35 when compared to HS day 0 (Figure 3.14B), while an increasing trend was found in HS vs. control at day 35 ($p=0.08$). No significant changes were found within the control group when comparing day 0, 21, and 35.

The results indicated that the BFR decreased significantly between the two groups for the femur, whereas only a trend was observed for the tibia (Figure 3.15).

The relative weight difference compared to day 0 was found to be significant between control and HS animals at day 14 (Figure 3.16). After 14 days, no additional weight loss was detected for the HS animals. Aside from the four animals removed from the study, the remaining animals had weight loss well within the approved limit of loss of 20% of weight at day 0 (Figure 3.16).

Discussion for Disuse Animal Model

Based on the hindlimb suspension models of Morey-Holton and Midura (Wronski and Morey-Holton 1987; Midura, Su et al. 2006) a custom made hindlimb suspension system was developed. Previous rodent hindlimb suspension models in the literature have shown physiologic changes such as a decrease in bone formation and an increase in bone

resorption (Wronski and Morey-Holton 1987; Morey-Holton and Globus 2002; Midura, Su et al. 2006). The custom made hindlimb suspension system was found to induce similar physiological effects. MicroCT results showed that bone resorption occurred in the trabecular region of the tibia indicated by the reduction in bone volume fraction, while maintaining tissue mineral density. Although mid-diaphyseal cortical bone was not lost significantly, a trend was still present, which was supported by the trend towards increasing marrow area, indicating that resorption may have increased at the endosteal surface. These observations were supported by serum markers for formation and resorption, which decreased and increased, respectively, after 21 days of hindlimb suspension, as well as the decrease in bone formation rate based on dual injected fluorescent labels. Finally the general wellbeing of the hindlimb suspended animals was not adversely affected, as evidenced by the maintenance of weight following a small weight loss during the initial assimilation period of 14 days of hindlimb suspension. Hence the developed hindlimb suspension model fulfilled all the set criteria for a successful disuse animal model, and was deemed ready for implementation for the subsequent experiments presented in chapter 4 and 5.

Conclusion

Due to the inadequacy of the tibia loader, and the fulfillment of the criteria for a successful in vivo loading animal model, the four-point bending setup was chosen for subsequent experiments. The developed hindlimb suspension model also fulfilled its set criteria for a successful disuse animal model. For the subsequent experiments the two animal models are combined in order to examine the effect of disuse on microdamage

remodeling. The last in-vivo loading experiment for the four-point bending setup made an initial successful combination of the two models. This was the final verification for the combined animal models, which would set up the next experiments presented in chapters 4 and 5.

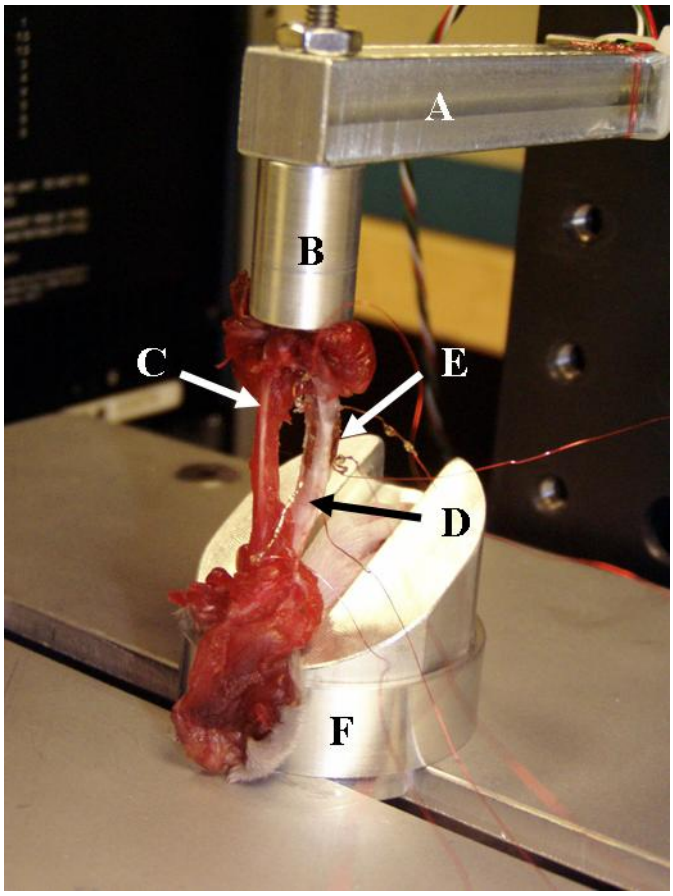

Figure 3.1. Tibia loader with rat tibia with attached foot inserted

A: Loading beam
B: Knee holder
C: Fibula exposed from lower limb of rat with foot attached
D: Tibia exposed from lower limb of rat with foot attached
E: Strain gauge with wires emerging from the middiaphysis of the tibia
F: Ankle holder

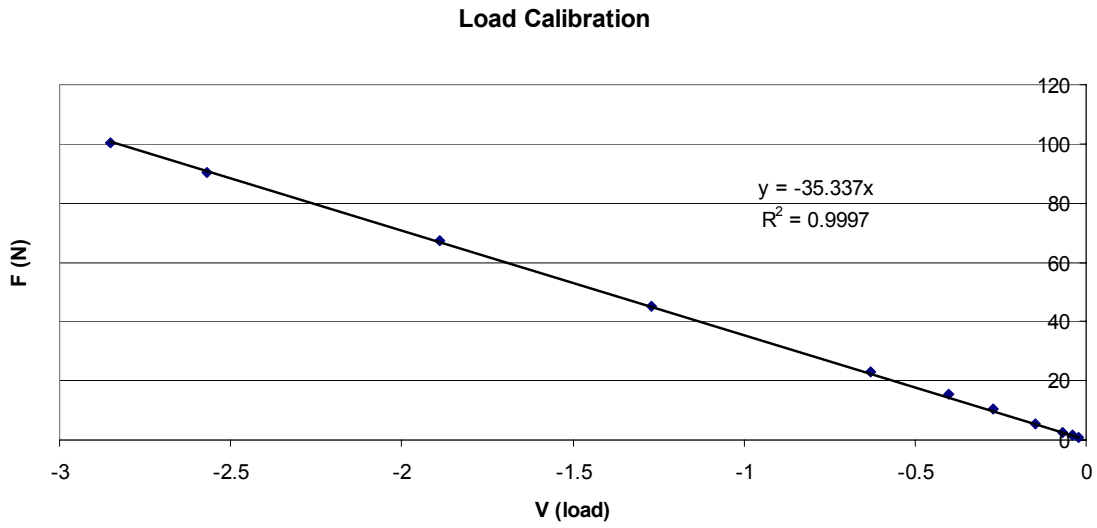

Figure 3.2. Load beam calibration

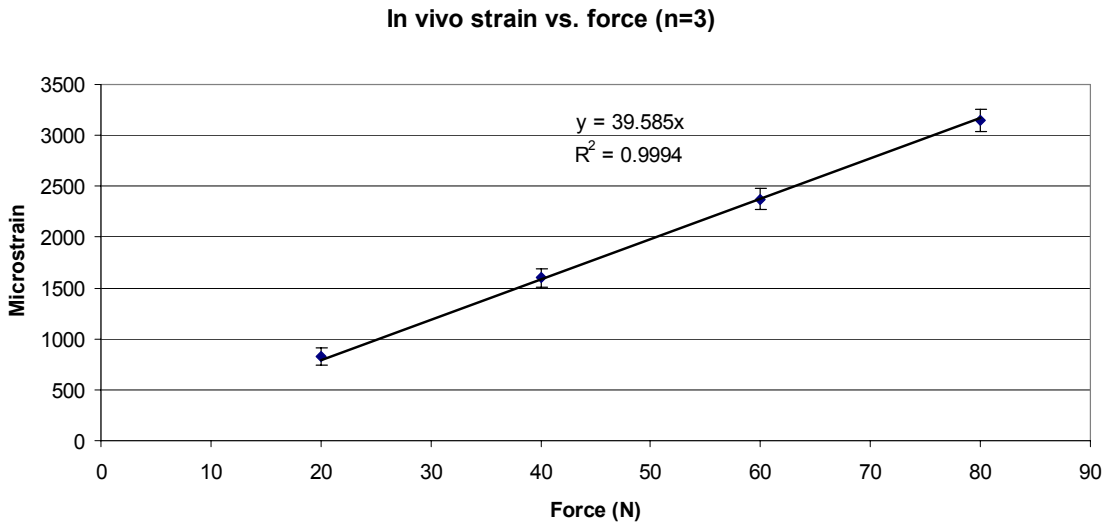

Figure 3.3. In vivo medial microstrain vs. applied force with tibia loader

Error bars indicate standard deviations.

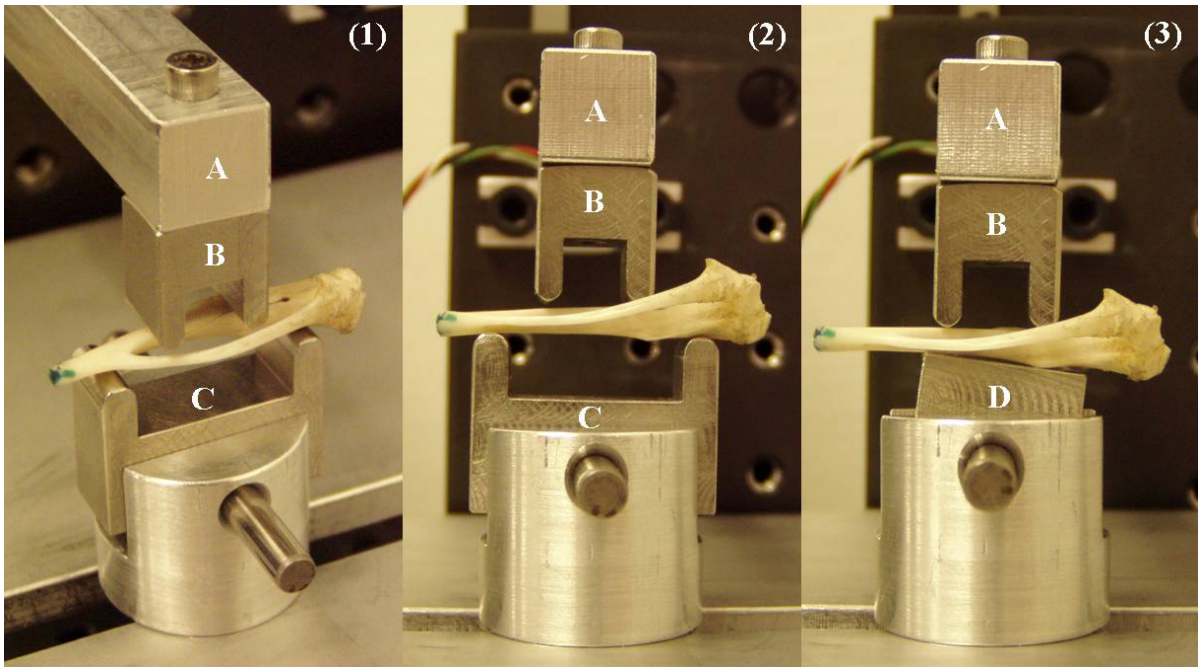

Figure 3.4. Four-point bending pads with tibia

(1): Isometric view of four-point bender
(2): Side view of four-point bender in bending configuration (use of **C**)
(3): Side view of four-point bender in non-bending configuration (use of **D**)
A: Loading beam
B: Upper (lateral) loading pad
C: Lower (medial) loading pad for bending configuration
D: Lower (medial) loading pad for non-bending (control) configuration

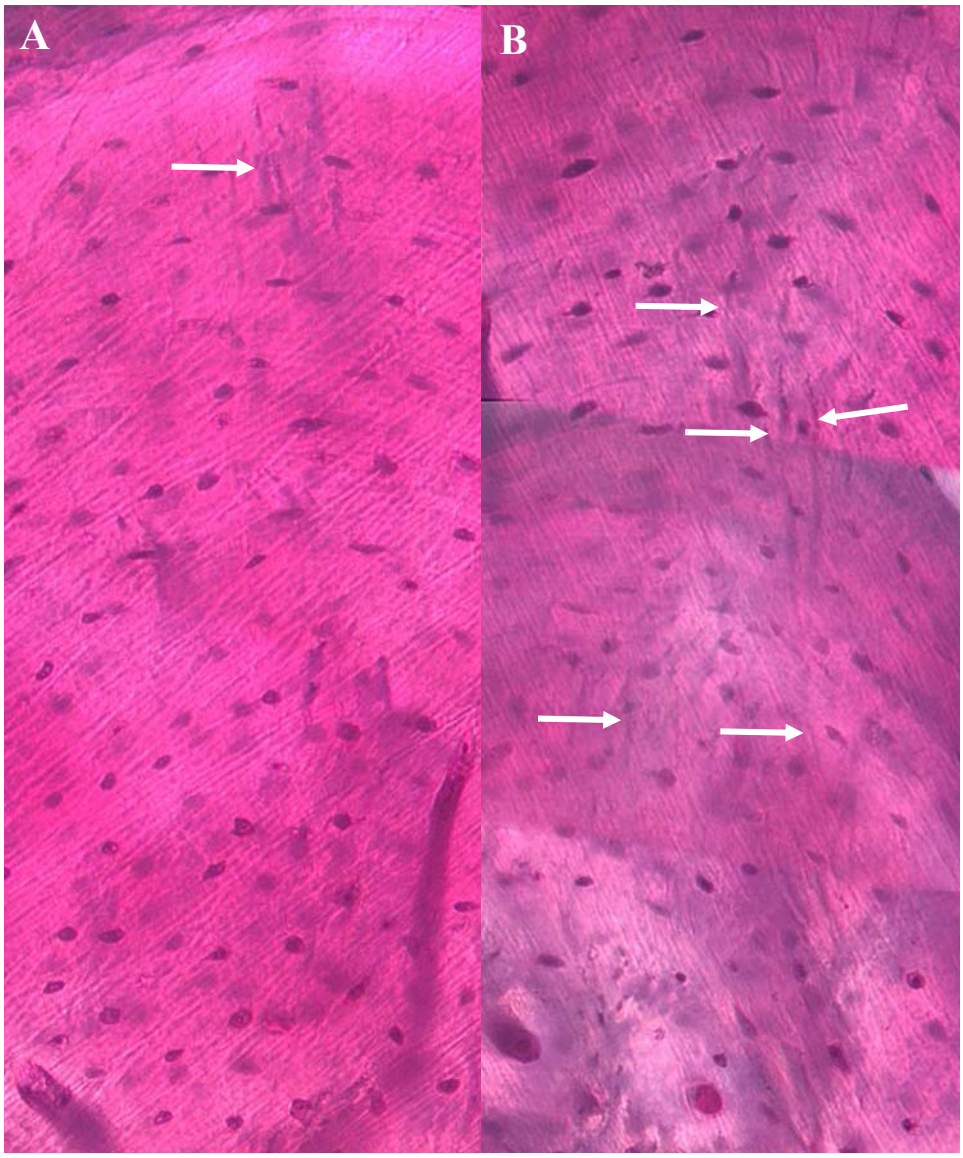

Figure 3.5. Representative light microscopy images of basic fuchsin stained tibiae sections

A: Control
B: Loaded (micro damaged)

Microdamage is indicated with white arrows. Top of images represent the periosteal surface, while the bottom of the images represent the endosteal surface.

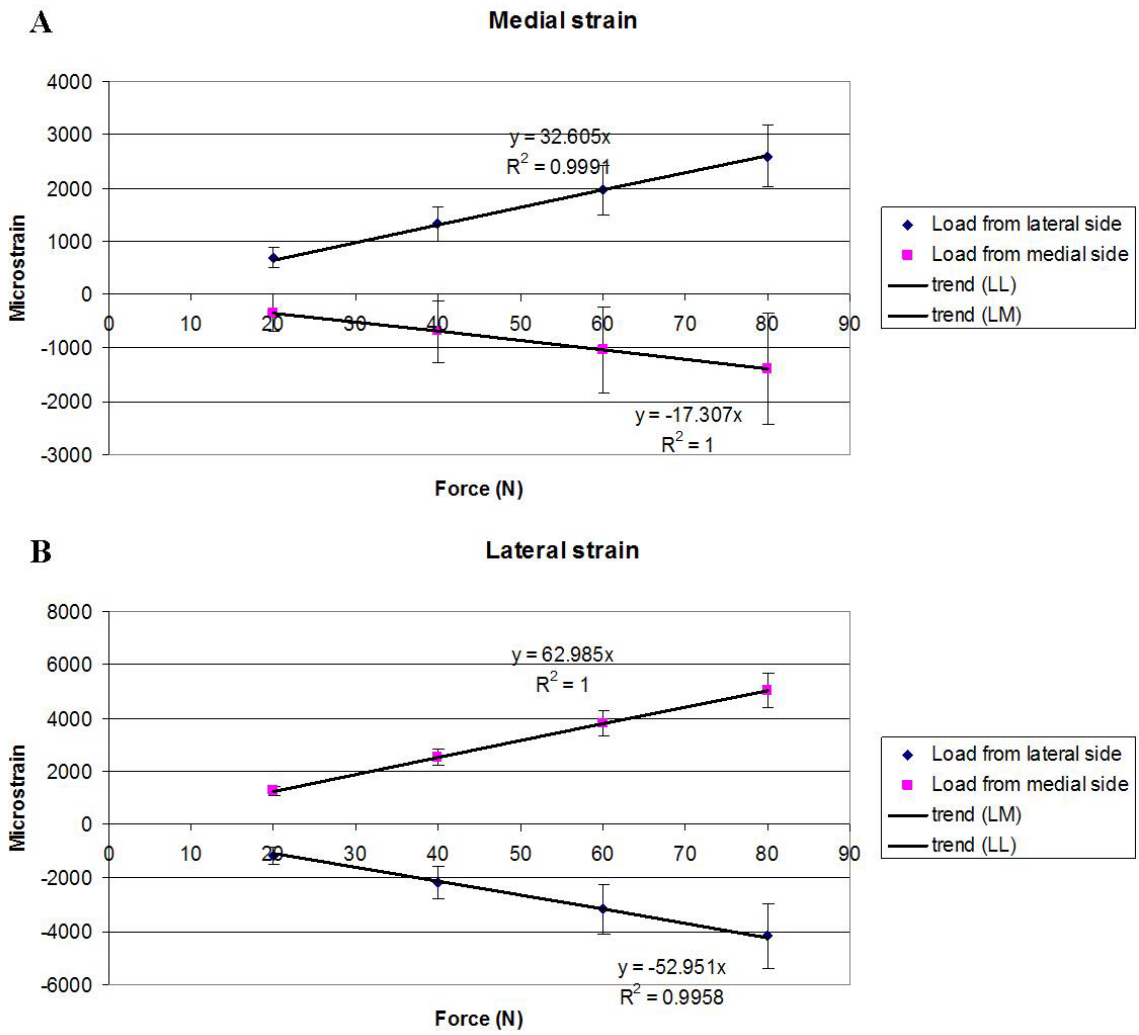

Figure 3.6. Mid-diaphysis microstrain vs. applied force for bending configuration ex-vivo

A: Medial strain for loading with upper loading pads from either medial or lateral side
B: Lateral strain for loading with upper loading pads from either medial or lateral side

Error bars indicate standard deviations.

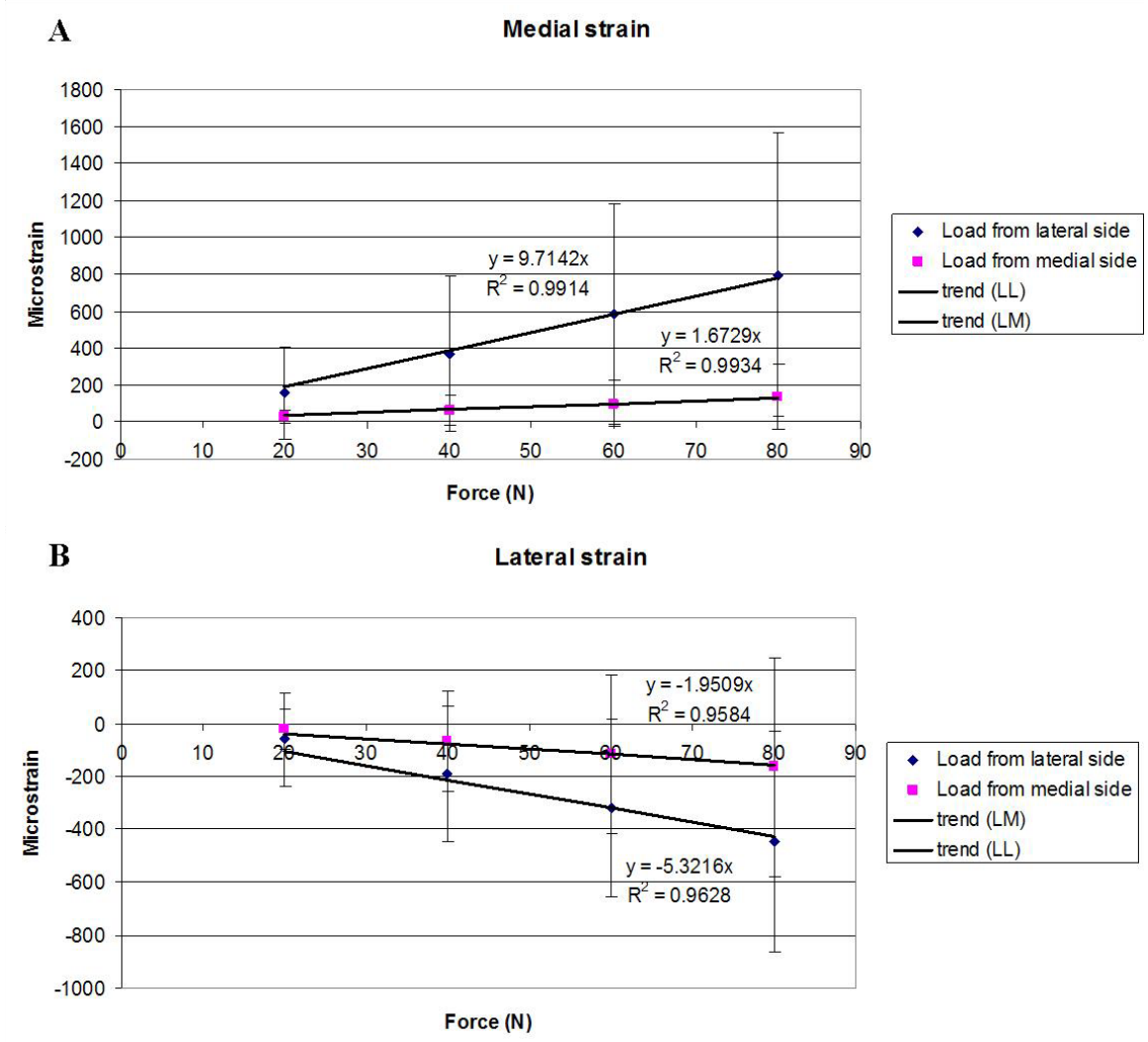

Figure 3.7. Mid-diaphysis microstrain vs. applied force for non-bending (control) configuration ex-vivo

A: Medial strain for loading with upper loading pads from either medial or lateral side
B: Lateral strain for loading with upper loading pads from either medial or lateral side

Error bars indicate standard deviations.

Figure 3.8. In-vivo loading of Sprague-Dawley rat

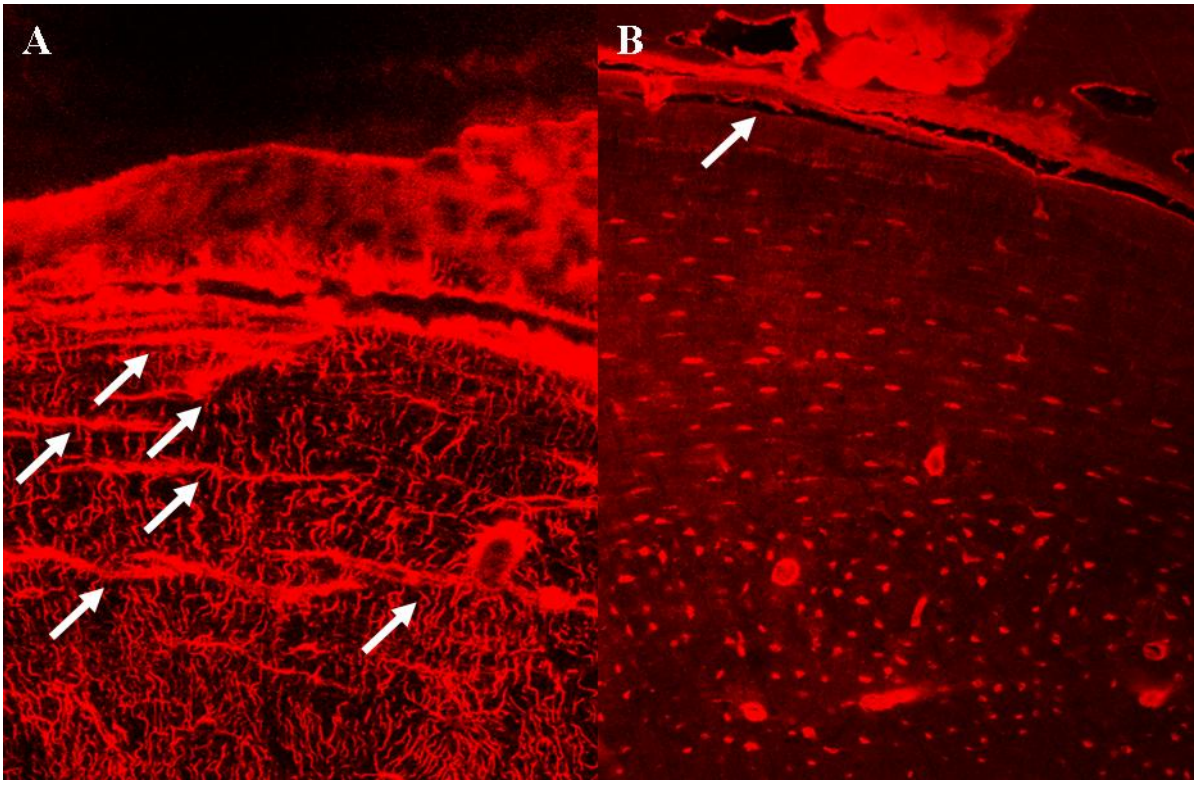

Figure 3.9. Microdamaged vs. undamaged cortical bone from in-vivo loading

A: Microdamaged loaded bone, with basic fuchsin labeled microdamage (white arrows)
B: Undamaged non-loaded bone, with non labeled microdamage caused by processing (white arrow)

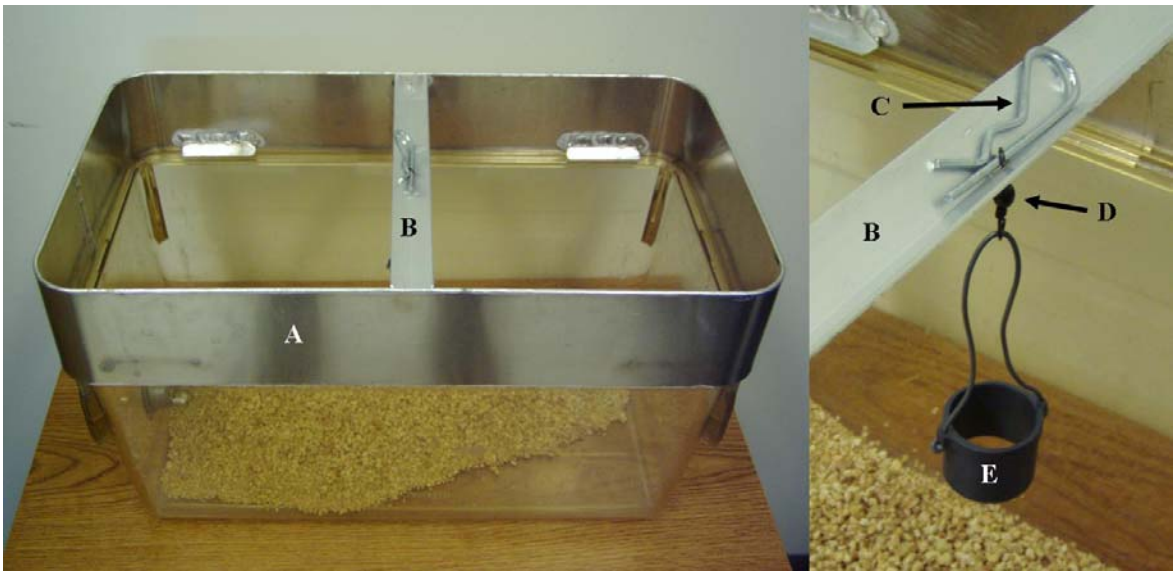

Figure 3.10. Hindlimb suspension system

Left: Steel frame on top of SPF rated standard ventilated #3 rat box
Right: Close-up of center beam
A: Steel frame
B: Center beam
C: Cotter pin
D: Swivel
E: Plastic tail holder

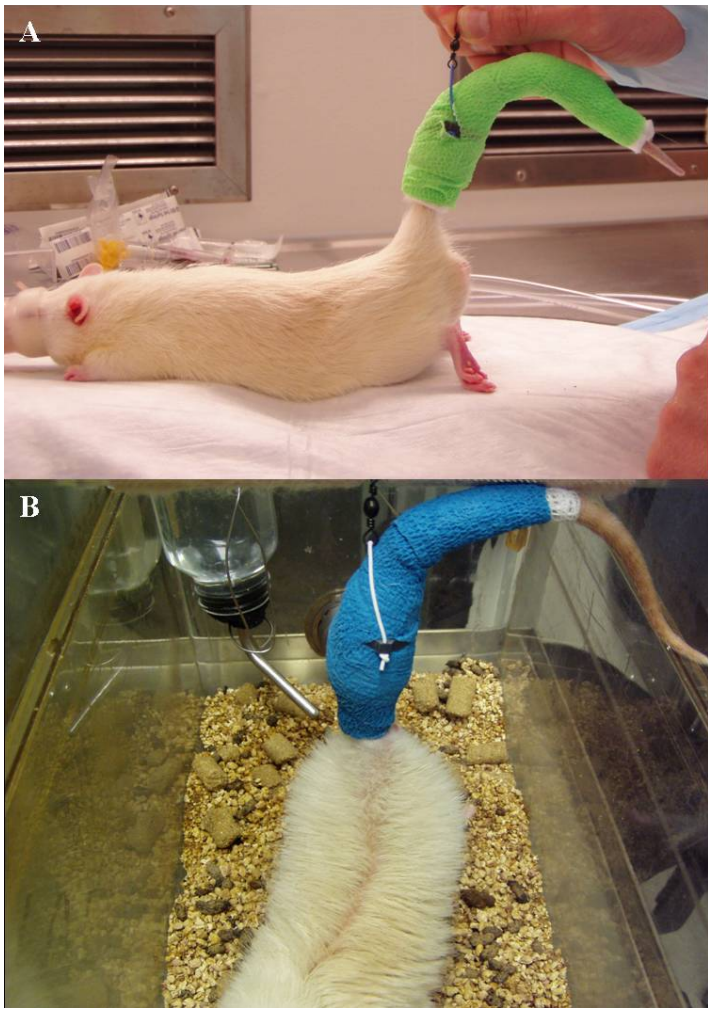

Figure 3.11. Hindlimb suspension tail preparation

A: Fully wrapped tail of anesthetized rat
B: Hindlimb suspended rat with water bottle visible within cage

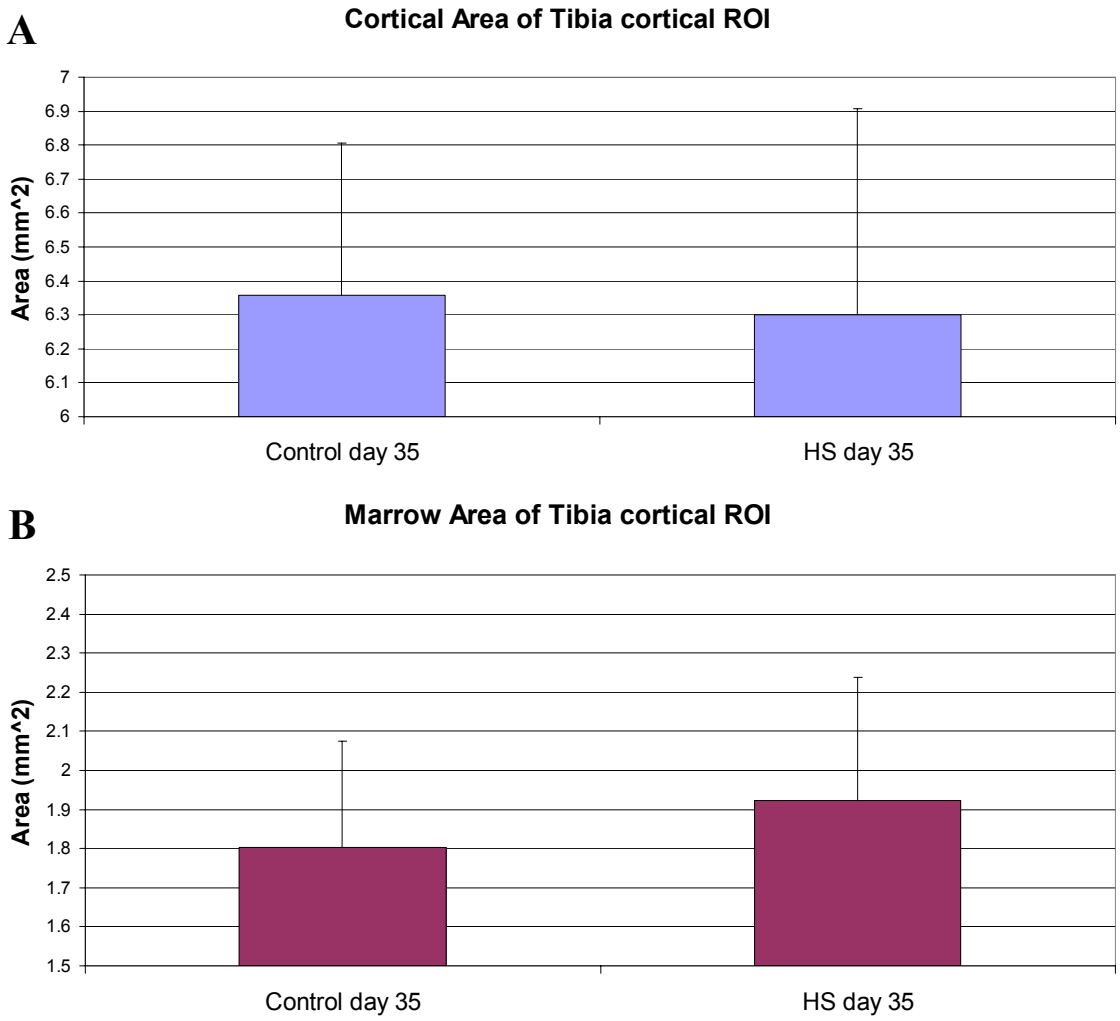

Figure 3.12. MicroCT parameters for tibia cortical ROI

A: Cortical area of tibia cortical ROI
B: Marrow area of tibia cortical ROI

Error bars indicate standard deviations.

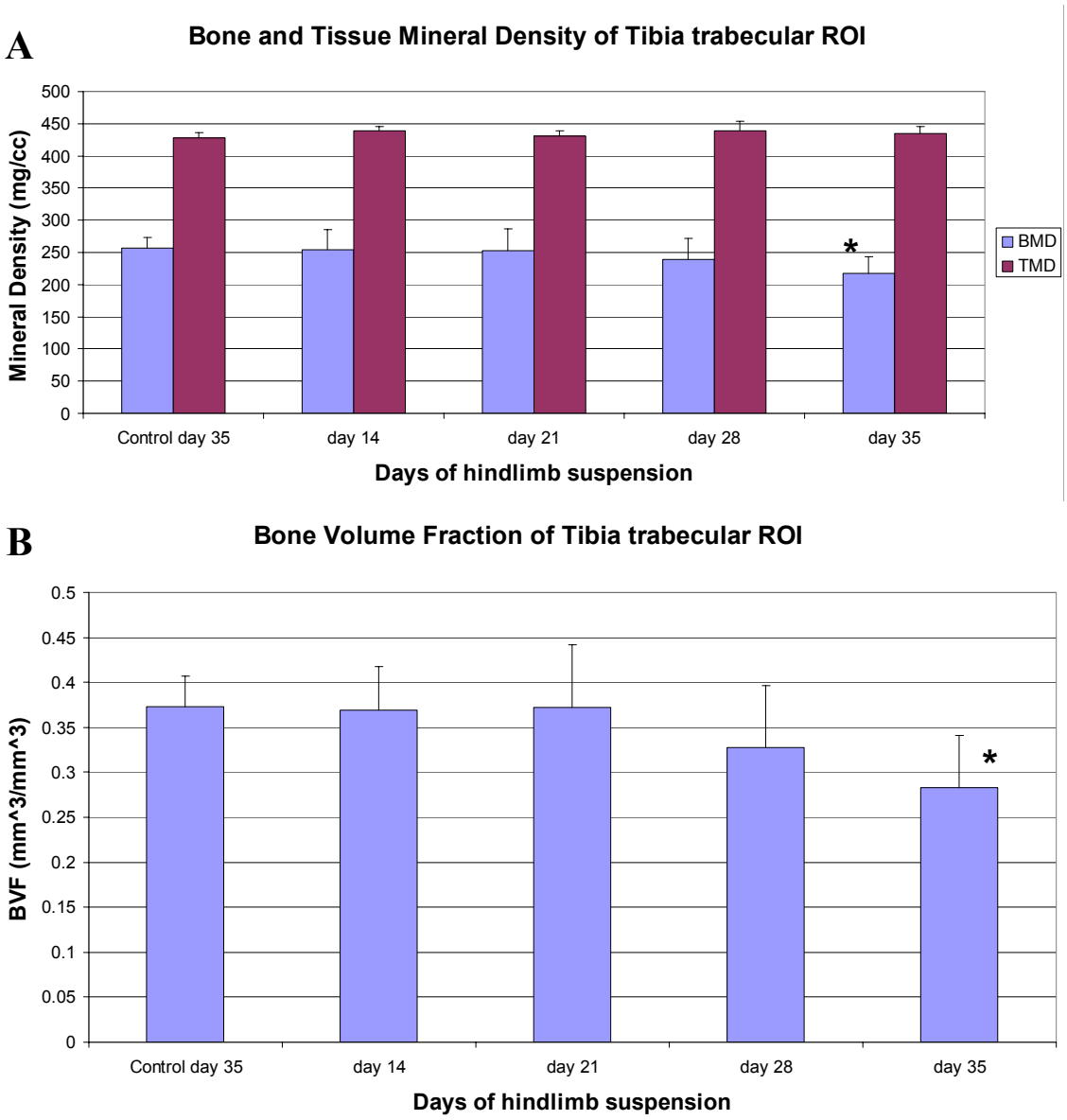

Figure 3.13. MicroCT parameters for tibia trabecular ROI

A: Bone and tissue mineral density of tibia trabecular ROI
B: Bone volume fraction of tibia trabecular ROI

Asterisk (*) indicate significant difference between group and control day 35. Error bars indicate standard deviations.

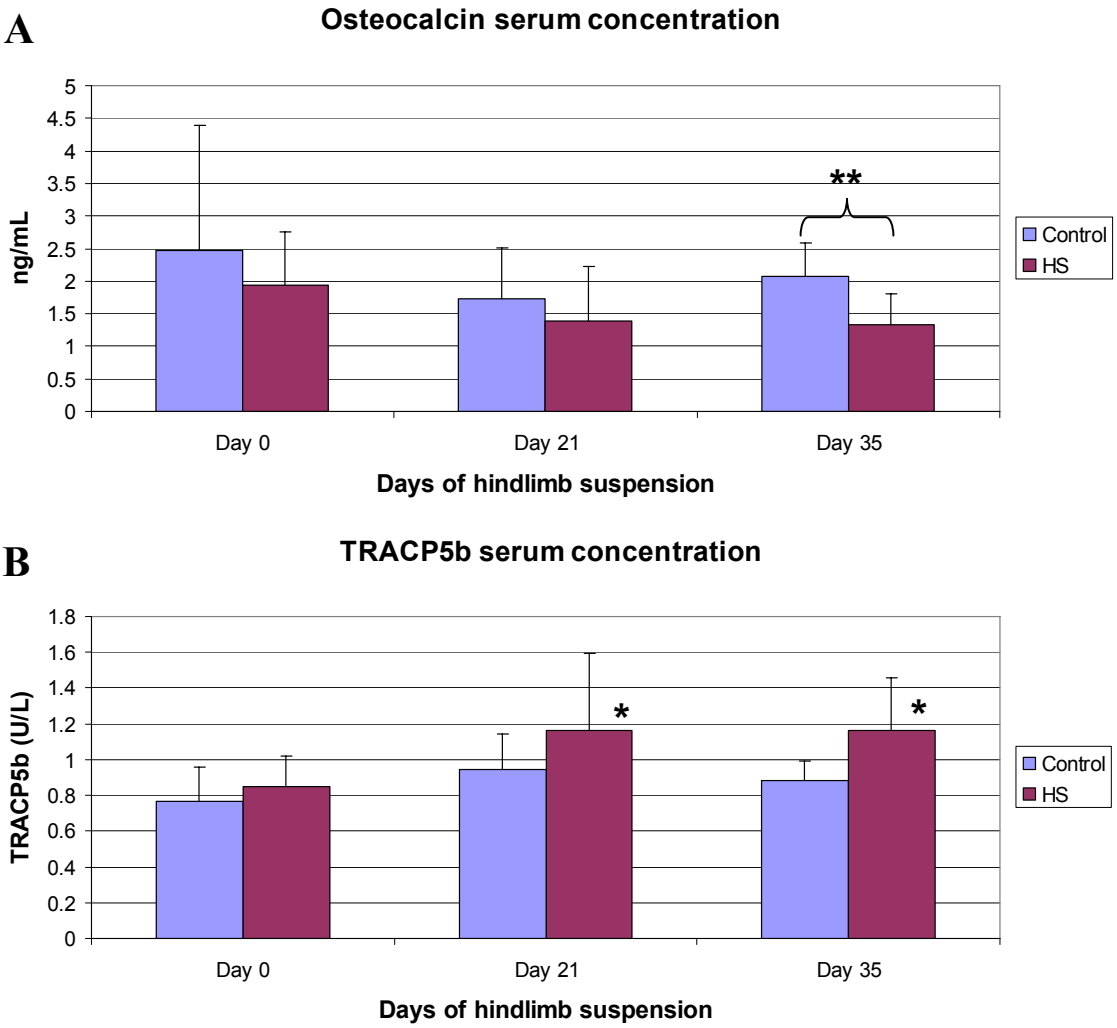

Figure 3.14. Osteocalcin and TRACP5b serum concentrations

A: Osteocalcin (OCN) serum concentration
B: RatTRAP (TRACP5b) serum concentration

Single asterisk (*) indicate significant difference within group between day 0 and indicated day. Double asterisk (**) indicate significant difference between group and control day 35. Error bars indicate standard deviations.

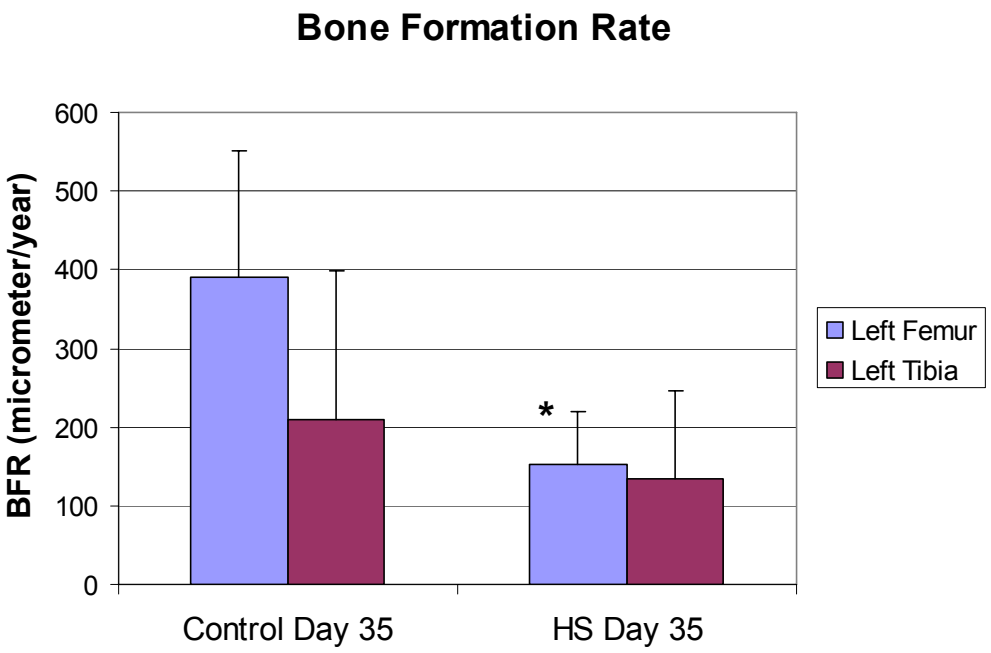

Figure 3.15. Bone formation rate

Bone formation rate for left tibiae and femora for control and hindlimb suspended animals at day 35. Single asterisk (*) indicate significant difference between group and control day 35. Error bars indicate standard deviations.

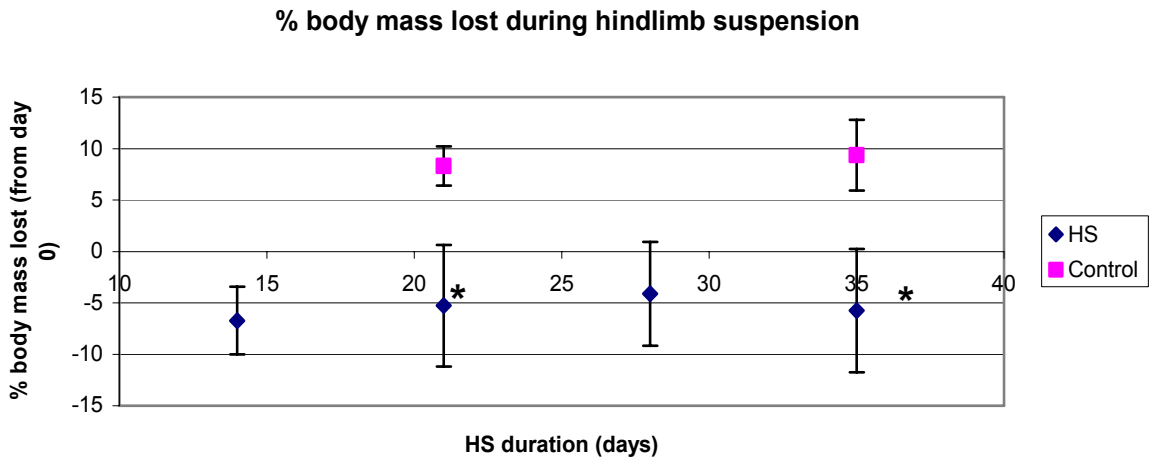

Figure 3.16. Percent body mass compared to day 0

Single asterisk (*) indicate significant difference between group and control at that day. Error bars indicate standard deviations.

	WB	HS
Avg. (με/N)	-65.15	-56.55
St.Dev.	6.31	18.87

Table 3.1. Slope of lateral strain vs. applied force relationship

	WB/HS
Avg. (με)	-10064.9
St.Dev.	1544.4

Table 3.2. Lateral strain at failure

References

Akhter, M. P., D. M. Raab, et al. (1992). "Characterization of in vivo strain in the rat tibia during external application of a four-point bending load." J Biomech **25**(10): 1241-6.

Bentolila, V., T. M. Boyce, et al. (1998). "Intracortical remodeling in adult rat long bones after fatigue loading." Bone **23**(3): 275-81.

Bikle, D. D., T. Sakata, et al. (2003). "The impact of skeletal unloading on bone formation." Gravit Space Biol Bull **16**(2): 45-54.

Caillot-Augusseau, A., L. Vico, et al. (2000). "Space flight is associated with rapid decreases of undercarboxylated osteocalcin and increases of markers of bone resorption without changes in their circadian variation: observations in two cosmonauts." Clin Chem **46**(8 Pt 1): 1136-43.

Danova, N. A., S. A. Colopy, et al. (2003). "Degradation of bone structural properties by accumulation and coalescence of microcracks." Bone **33**(2): 197-205.

De Souza, R. L., M. Matsuura, et al. (2005). "Non-invasive axial loading of mouse tibiae increases cortical bone formation and modifies trabecular organization: a new model to study cortical and cancellous compartments in a single loaded element." Bone **37**(6): 810-8.

Diab, T. and D. Vashishth (2005). "Effects of damage morphology on cortical bone fragility." Bone **37**(1): 96-102.

Follet, H., J. Li, et al. (2007). "Risedronate and alendronate suppress osteocyte apoptosis following cyclic fatigue loading." Bone **40**(4): 1172-7.

Forwood, M. R., M. B. Bennett, et al. (1998). "Modification of the in vivo four-point loading model for studying mechanically induced bone adaptation." Bone **23**(3): 307-10.

Forwood, M. R. and C. H. Turner (1995). "Skeletal adaptations to mechanical usage: results from tibial loading studies in rats." Bone **17**(4 Suppl): 197S-205S.

Fritton, J. C., E. R. Myers, et al. (2001). Validation of a loading apparatus: Characterization of murine tibial surface strains in vivo. Orthopaedic Research Society, San Francisco, CA.

Fritton, J. C., E. R. Myers, et al. (2005). "Loading induces site-specific increases in mineral content assessed by microcomputed tomography of the mouse tibia." Bone **36**(6): 1030-8.

Fritton, J. C., E. R. Myers, et al. (2005). Adaptation of cancellous bone mass and architecture following orchidectomy and loading. ASME Summer Bioengineering Conference, Vail, CO.

Inman, C. L., G. L. Warren, et al. (1999). "Mechanical loading attenuates bone loss due to immobilization and calcium deficiency." J Appl Physiol **87**(1): 189-95.

Midura, R. J., X. Su, et al. (2006). "A simulated weightlessness state diminishes cortical bone healing responses." J Musculoskelet Neuronal Interact **6**(4): 327-8.

Morey-Holton, E. R. and R. K. Globus (2002). "Hindlimb unloading rodent model: technical aspects." J Appl Physiol **92**(4): 1367-77.

Robling, A. G., D. B. Burr, et al. (2001). "Recovery periods restore mechanosensitivity to dynamically loaded bone." J Exp Biol **204**(Pt 19): 3389-99.

Sakata, T., B. P. Halloran, et al. (2003). "Skeletal unloading induces resistance to insulin-like growth factor I on bone formation." Bone **32**(6): 669-80.

Turner, C. H., M. P. Akhter, et al. (1991). "A noninvasive, in vivo model for studying strain adaptive bone modeling." Bone **12**(2): 73-9.

Verborgt, O., G. J. Gibson, et al. (2000). "Loss of osteocyte integrity in association with microdamage and bone remodeling after fatigue in vivo." J Bone Miner Res **15**(1): 60-7.

Verborgt, O., N. A. Tatton, et al. (2002). "Spatial distribution of Bax and Bcl-2 in osteocytes after bone fatigue: complementary roles in bone remodeling regulation?" J Bone Miner Res **17**(5): 907-14.

Vico, L., P. Collet, et al. (2000). "Effects of long-term microgravity exposure on cancellous and cortical weight-bearing bones of cosmonauts." Lancet **355**(9215): 1607-11.

Wronski, T. J. and E. R. Morey-Holton (1987). "Skeletal response to simulated weightlessness: a comparison of suspension techniques." Aviat Space Environ Med **58**(1): 63-8.

CHAPTER 4

EFFECTS OF DISUSE ON BONE REMODELING IN REPONSE TO MICRODAMAGE

Summary

Bone remodeling in response to fatigue microdamage is altered with age, which may increase fracture risk. Furthermore, bone loss associated with aging may result from disuse due to reduction in physical activity or infirmity. The purpose of this study was to examine the effects of disuse on bone remodeling in response to microdamage, potentially providing clinically important insight into the relationship between microdamage accumulation and increased fracture risk in the elderly.

At day 0, 120 male 6-month old Sprague Dawley rats were assigned to one of two groups: weight-bearing (WB) or hindlimb suspension (HS). At day 14, animals were anesthetized and their left tibia underwent cyclic 4-point bending in order to produce fatigue-induced microdamage (7200 cycles at 2 Hz, -7000 microstrain max. at the lateral mid-diaphysis for both WB and HS). Within each group, the rats were further divided into three subgroups (n=20), corresponding to three sacrificial times (day 14, 18 or 35). At sacrifice, right/left pairs of tibiae were assigned to one of three treatments within each subgroup: flow cytometry for hematopoietic stem cell (HSC) and monocyte markers (n=6), basic fuchsin staining for microdamage assessment (n=7), or histological/immunohistochemical staining (Picr-Sirius Red, ELF97 (TRAP), Apoptag)

(n=7). Prior to staining, morphologic analysis was conducted on the last two groups using 3D microCT.

Morphologic examinations revealed that the damage induced a stress fracture response as defined by Uthgenannt et. al. (Uthgenannt, Kramer et al. 2007), which at day 35 resulted in a significant increase in woven bone apposition for both WB and HS, with the WB group being significantly greater than the HS group. At day 35, the WB group had a significant decrease in microdamage from levels on day 14, while the HS group showed no change in remaining damage. Histological and immunohistochemical results showed that the microdamage induced at day 14 resulted in similar amounts of osteocyte apoptosis between HS and WB, corresponding to the similar amounts of microdamage detected with basic fuchsin staining. Flow cytometry indicated that a shift in the osteoclast lineage had occurred, as evidenced by an increase in HSCs and a decrease in monocytes in the damaged leg for WB compared to HS at day 35. HS showed no difference between contralateral tibiae for both flow cytometry markers at any time points. ELF97 staining supported this evidence, with a significant increase in TRAP positive resorption pits in the WB group for day 18 and 35, while the HS group showed only small increase for day 18, with a return to control levels at day 35. Taking the flow cytometry and histology together, the evidence of "no damage removal" at day 35 for HS suggest a lack of osteoclast activation, rather than a change in the targeting mechanisms of remodeling.

This study demonstrated that disuse alters the microdamage response through a reduction in woven bone production and the lack of resorption of microdamage. The data suggests that elderly individuals with significantly reduced activity may accumulate

further microdamage. Most importantly, while a variety of studies have proposed that the repair of microdamage is triggered by cell apoptosis, these results suggest that apoptosis-induced repair may be insufficient without additional stimuli resulting from mechanical usage.

Introduction

Microdamage is a natural occurrence in cortical bone (Frank, Ryan et al. 2002; Lee, Mohsin et al. 2003), and can be caused by damage inducing loads ex vivo (Burr, Forwood et al. 1997; Lee, Arthur et al. 2000; Lee, O'Brien et al. 2000; O'Brien, Taylor et al. 2002; Danova, Colopy et al. 2003; O'Brien, Taylor et al. 2003) and in vivo (Burr, Martin et al. 1985; Stover, Martin et al. 1993). Moreover, microdamage has been shown to induce localized osteocyte apoptosis surrounding individual microcracks (Verborgt, Gibson et al. 2000; Verborgt, Tatton et al. 2002), possibly as a result of hyperemia and an associated decrease in lacunocanalicular interstitial fluid flow (Muir, Sample et al. 2007). Computational models corroborate these findings and indicate that fatigue damage impedes transport from the blood supply, depleting the areas downstream of the microdamage of molecular entities (Tami, Nasser et al. 2002). These effects were confirmed in a pilot study, suggesting a link between interstitial fluid flow, mass transport, maintenance of osteocyte viability, and regulation of remodeling activity (Tami, Nasser et al. 2002). In addition, fatigue damage has been shown to increase expression of dHIF-1α, suggesting that microdamage results in impaired O_2 delivery due to disruption in fluid flow (Herman, Laudier et al. 2007). The same study showed an exponential decline in VEGF-A expression around cracks in a pattern similar to the

apoptotic osteocytes seen by Verborgt et. al. (Herman, Laudier et al. 2007), thereby supporting the concept that microcracks are associated with localized decreases in fluid flow.

Microdamage and subsequent osteocyte apoptosis correspond spatially with targeted remodeling in vivo (Burr, Martin et al. 1985; Burr and Martin 1993; Mori and Burr 1993; Bentolila, Boyce et al. 1998; Verborgt, Gibson et al. 2000; Lee, Staines et al. 2002), which was proven to be causal when the inhibition of osteocyte apoptosis prevented remodeling following fatigue damage (Cardoso, Laudier et al. 2006). In addition, key signaling events involved in osteocyte apoptosis occur early after fatigue loading and are necessary for resorption (Herman, Cardoso et al. 2007).

It has been suggested that whole-bone failure in osteoporosis could result from changes in microdamage related remodeling due to a positive feedback between microdamage and the resulting remodeling that attempts to repair the damage (Burr, Forwood et al. 1997). Microdamage results in a loss of mechanical integrity of the bone tissue, followed by a potentially greater loss in continuum-level bone strength and/or stiffness due to resorption at the beginning of the remodeling cycle. The reduced stiffness and strength may result in further damage or overt failure at lower loads than those required in the original intact bone, thus creating a positive feedback loop.

In the elderly population where osteoporosis is a frequent occurrence, such changes in the remodeling response could occur as a result of the reduced skeletal blood flow and endothelium-dependent vasodilation associated with aging (Prisby, Ramsey et al. 2007). Prior work has indeed demonstrated that bone remodeling in response to fatigue microdamage is altered with age, evidenced by a reduction in remodeling

response in trabecular bone (Waldorff, Goldstein et al. 2007) and/or a delay in remodeling response in cortical bone (Herman, Faria et al. 2006), both of which may lead to an increase in fracture risk.

Aside from the alterations in remodeling activity due to age, bone loss associated with aging may also result from disuse due to reductions in physical activity or infirmity. Disuse models such as prolonged bed rest have shown that urinary levels of formation markers decreased, while resorption markers and resistance to IGF-1 increased leading to cortical and cancellous bone loss (Inoue, Tanaka et al. 2000; Kim, Iwasaki et al. 2003). Similar effects have been found in cosmonauts during long term exposure to microgravity, during which disuse of the weight bearing limbs is prevalent (Caillot-Augusseau, Vico et al. 2000; Vico, Collet et al. 2000).

To simulate the disuse condition of bed rest and weightlessness, several groups have developed rodent hindlimb suspension models (Wronski and Morey-Holton 1987; Morey-Holton and Globus 1998; Morey-Holton and Globus 2002) that induce similar effects, such as increased resorption and decreased formation (Bloomfield, Allen et al. 2002), increased resistance to IGF-I (Sakata, Halloran et al. 2003; Sakata, Wang et al. 2004), and significant reduction of blood flow (Bloomfield 2006). Disuse hindlimb suspension models have also been shown to decrease interstitial fluid flow due to decreased pressure gradients (Stevens, Meays et al. 2006), with several studies suggesting that convective transport by means of load-induced fluid flow may be necessary to provide sufficient transport of larger molecules such as proteins to and from osteocytes (Knothe Tate, Knothe et al. 1998; Knothe Tate, Niederer et al. 1998). In addition it has been shown that osteocytes mechanically stimulated in vitro release soluble factors that

inhibit osteoclastogenesis (Tan, de Vries et al. 2007; You, Temiyasathit et al. 2008), while osteocyte apoptotic bodies initiate osteoclastogenesis leading to localized bone resorption in a RANKL-independent manner (Kogianni, Mann et al. 2008).

It is therefore hypothesized that the reduced fluid flow within the canalicular system in a disuse setting could prevent the apoptotic distress signals released by osteocytes surrounding microcracks from reaching their cytokine receptors, thereby reducing or inhibiting targeted remodeling. Hence the effects from disuse, in combination with the alteration of remodeling response associated with age, may lead to generalized skeletal weakening and alterations in general skeletal repair mechanisms. In particular, intermixing prolonged times of disuse with sporadic periods of activity could potentially increase an individuals' risk for microdamage accumulation.

The purpose of this study was therefore to examine the effects of disuse on bone remodeling in response to microdamage, potentially providing clinically important insight into the relationship between microdamage accumulation and increased fracture risk in the elderly.

Materials and Methods

Animals

Male 6-month old adult Sprague Dawley rats (350-450g) were obtained from Harlan. Animals were allowed to acclimate to our animal facility for at least three days before being included in the experiment. The procedures used in this study were approved by the University Committee on Use and Care of Animals at the University of Michigan. Animals were housed in individual non-ventilated cages in a temperature-

controlled room (68-72˚F) with a 12:12-hour light-dark cycle. Water and rat chow were provided ad libitum.

In vivo strain gauge calibration for load parameters

In order to determine the load parameters required to induce a strain level of -7000 microstrain at the lateral side of the mid-diaphysis of the tibia undergoing four-point bending, the strain-applied force relationship was determined for six 8-month old Sprague Dawley rats that were split into two groups: 1) Hindlimb suspension (HS) for 14 days (n=3), and 2) Normal weight bearing (WB) for 14 days (n=3). At day 14, all rats were anesthetized and a small incision was made at the lateral side at the mid-diaphysis of the tibiae. This allowed strain gauges to be placed bi-laterally on the lateral side of the tibiae, 8mm proximal to the tibia-fibula junction. The average slope of the lateral strain vs. applied force relationship was determined for each group (Table 4.1). No significant difference was found between the HS and WB group, indicating that the loading regime induces similar strain magnitudes for weight bearing and hindlimb suspended animals at day 14. Based on the findings a slope of -65.15με/N was chosen, resulting in a lateral strain vs. applied force relationship of:

$$\mu\varepsilon_{lateral} = -64.93 \cdot F_{Applied\ Load\ (N)}$$

This relationship would be used for all the loading parameters in the subsequent experiment.

Experimental protocol

After acclimation (day 0), 120 rats were assigned to one of two groups: Weight-bearing (WB) or hindlimb suspension (HS). Within each group, the rats were further divided into three subgroups (n=20), corresponding to three sacrifice time points (day 14, 18 or 35). Animals assigned to the HS group were briefly anesthetized with an isoflurane (2%):oxygen balance, and hindlimb suspended using a custom made hindlimb suspension system which is adaptable with standard SPF rated ventilated #3 rat boxes. Unpublished work has successfully shown that the custom made model (Chapter 3) induces similar physiological changes as previous models (Wronski and Morey-Holton 1987; Morey-Holton and Globus 2002; Midura, Su et al. 2006), where the disuse condition of the hindlimbs resulted in a decrease in bone formation and increase in bone resorption, while the general wellbeing of the hindlimb suspended animals was maintained.

At day 14, all animals were anesthetized and their left tibia underwent four-point bending using a model based on Turner et. al. (Turner, Akhter et al. 1991) in order to produce fatigue-induced microdamage. Specifically, the left tibia underwent a sinusoidal loading regime (7200 cycles at 2 Hz) with a maximum and minimum load of 107.8 N and 57.6N, respectively. This induced a maximum lateral strain of -7000 microstrain at the mid-diaphysis for both the HS and WB group (Chapter 3). Previous work had shown that loading the right tibia in a 'non-bending' configuration of the four-point bending setup as done by Turner et. al. (Turner, Akhter et al. 1991) induced strain levels between -1000 to -400 microstrain at the lateral side for the prescribed sinusoidal loading regime. Turner et. al. utilized this configuration of their four-point bender to evaluate the effects of just pin-point loading to the bone and muscle tissue, by loading the control leg in a non-

bending fashion. For our setup, the prescribed 'non-bending" loading regime was not sufficient to induce microdamage within the region of interest (ROI) 8 mm proximal to the tibia-fibula junction, at the point of maximum bending. However, it was found that at the points of contact between the loading pads of the four-point bending setup, significant amounts of microdamage were induced. To adequately test the hypothesis, it was hence determined that any microdamage induced at the application of load for the control load would result in remodeling, which would skew the findings due to the remodeling of the ROI of the left tibia undergoing pure bending. Therefore, the right tibia would serve as a non-loaded, completely undamaged control.

Once the loading regime was complete, animals were allowed full recovery from anesthesia, and subsequently hindlimb suspended or allowed full weight bearing again, in correspondence with their group assignment.

At sacrifice, right/left pairs of tibiae were carefully dissected free of soft tissue and assigned to one of three treatments within each subgroup: flow cytometry for HSC and monocyte markers (n=6), basic fuchsin staining for microdamage assessment (n=7), or histological and immunohistochemical staining (n=7). Prior to staining, morphologic analysis was conducted on the last two groups using 3D microCT.

Microcomputed tomography (microCT)

Once carefully dissected free of soft tissue, the tibiae not used for flow cytometry were scanned on a microcomputed tomography (microCT) system (GE Healthcare Systems) and reconstructed with a voxel size of 25 μm. Morphological parameters were determined for the tibiae at the cortical region of interest (ROI) that experienced the

maximum bending during four-point bending (i.e. at the mid-diaphysis). Specifically the ROI had a length of 4 mm with its center located 8mm proximal to the tibia/fibula junction (Figure 4.1). Bone architectural parameters for this ROI were determined using a custom analysis program and a commercially available voxel analysis software package (MicroView v.2.2). The following parameters were calculated: tissue mineral content (TMC), tissue mineral density (TMD), cross sectional moments of inertia (Ixx, Iyy, Izz), cortical and marrow area.

Flow cytometry (FACS)

Specimens assigned for flow cytometry were placed in PBS + 2% NCS on ice immediately after dissection. Marrow was flushed from the tibiae, washed in PBS + 2% NCS, and 10^6 cells were removed and put on ice for subsequent staining. To reduce background noise from red blood cells in the flushed marrow, the collected cells were briefly resuspended in Ack lysis buffer and subsequently washed in PBS + 2% NCS. To prevent non-specific binding of selected antibodies, cells were incubated with rIgG, mIgG, and rIgAκ (BD Biosciences Pharmingen) for 15 min at 4˚C prior to staining. In order to determine the effect of the experimental conditions on the osteoclast lineage the cells were incubated for 25 min at 4˚C with the following antibodies:

Anti-mouse CD 117 (c-kit), Hematopoietic Stem Cell (HSC) marker, PE-conjugated, isotype: Rat IgG2bκ, Clone: 2B8 (Beckman Coulter Inc., CA).

Anti-rat CD 11b (Mac-1 α chain), Monocyte/macrophage marker, FITC-conjugated, isotype: Mouse IgA,κ, Clone: WT.5 (BD Biosciences Pharmingen).

Previous work (Aicher, Rentsch et al. 2007) has shown that the 2B8 clone for mouse CD117 cross-reacted with rat CD117 by FACS (Santa Cruz Biotech., CA). In addition positive staining was determined with the selected CD117 antibody by achieving similar staining for control rat tibiae marrow cells and C57 mouse tibiae marrow cells (data not shown).

Once stained, cells were analyzed using a FACS Calibur (BD Biosciences, CA). For each sample 30,000 events were collected. For the analysis of the flow cytometry data, the forward scatter and side scatter gate (R1) (Figure 4.2) was set to a region that has previously been shown to include stem cells and monocytes (Eghbali-Fatourechi, Khosla et al. 2003). The CD117 and CD11b positive populations within the gate were identified as cells expressing specific levels of fluorescent activity above the nonspecific staining and autofluorescence of the isotype control, indicated by the M1 and M2 region in the fluorescence intensity histograms (Figure 4.3). Specifically the M2 region was used for CD11b analysis, while the M1 region was used for CD117 analysis.

Due to insufficient cell counts during FACS, 7 animals had to be eliminated from the flow cytometry data resulting in final groups of: Day 14, WB (n=6)/HS (n=5); Day 18, WB (n=3)/HS (n=4); Day 35, WB (n=4)/HS (n=6).

Basic fuchsin staining

Upon dissection and prior to microCT scanning, specimens assigned for basic fuchsin staining were kept in 70% ethanol. After microCT scanning, the tibiae were completely dehydrated and stained with basic fuchsin according to Burr et. al.'s protocol (Burr and Hooser 1995). Subsequently they were embedded in Koldmount fast curing

cold monomer (IDP/Vernon-Benshoff Company, Albany, NY), and sectioned 400 μm transverse to the longitudinal axis of the tibia at the microCT ROI using a Buehler Isomet low speed diamond blade saw. The section closest to the center of the ROI for each tibiae was mounted on a plastic microscope slide using cyanoacrylate and polished to a final thickness of 150-200 μm. The sections were examined with a standard confocal microscope (Zeiss LSM 510-META Laser Scanning Confocal Microscope) at 40x magnification using a HeNe1 laser (543 nm) with a Texas Red/Rhodamine filter. Images were taken for the entire cortical region and subsequently analyzed using the Zeiss LSM Image Browser (ver. 4.2.0.121) in order to quantify linear microdamage within the cortical region (Figure 4.4).

Only linear microdamage was quantified, since it has been shown that remodeling only occurs in bone with linear microcracks, while bone containing only diffuse damage fails to initiate a remodeling response (Herman, Berman et al. 2008).

Using light microscopy, the cortical cross sectional areas were calculated with Bioquant image software (BQ OSTEO v.7.20.10) while omitting woven bone areas.

Histology and immunohistochemistry

Upon dissection and prior to microCT scanning, specimens assigned for histology and immunohistochemistry were immediately placed in 10% NBF for two days, followed by 70% ethanol. Subsequent to microCT scanning, specimens were decalcified over five weeks using 10% EDTA at 4˚C, after which specimens were paraffin embedded. The bone within the microCT ROI was sectioned 7 μm transverse to the longitudinal axis of the tibia.

- ELF97 (TRAP)

Two paraffin-embedded sections per tibia (one millimeter apart within the microCT ROI, with the first section 7 mm proximal to the tibia/fibula junction) were stained with ELF97 phosphate (Molecular Probes, OR) in order to visualize TRAP positive resorption pits within the cortical and woven bone. The protocol used for the fluorescence-based ELF97 TRAP stain was adapted from the in vitro ELF97 stain protocol developed by Filgueira (Filgueira 2004). Specifically, 50µL of ELF97 reaction mix (41.15µL dH_2O, 0.55µL Sodium nitrite, 5.00µL 2mM ELF97, 2.20µL Acetate, 1.1µL Tartrate) was applied to each selected section, which was incubated at room temperature in the dark for five minutes. Sections were subsequently rinsed in dH_2O and cover slips were applied using Prolong Gold antifade reagent (Invitrogen/Molecular Probes, OR). Sections were imaged immediately using appropriate fluorescent filters (Figure 4.5). Histological measurements included TRAP positive intra cortical resorption pits per cortical area, percent TRAP positive periosteal perimeter, and percent TRAP positive endosteal perimeter. These measurements were determined while omitting woven bone areas. The average measurements for the two sections were used for the subsequent analysis.

- Picro-Sirius Red

Two sections per tibia (one millimeter apart within the microCT ROI, with the first section 7 mm proximal to the tibia/fibula junction) were stained with Picro-Sirius Red F3BA in order to quantify woven bone apposition (Sweat, Puchtler et al. 1964; Puchtler, Meloan et al. 1988). Using polarized light microscopy, collagen fibers were

highlighted to distinguish the lamellar and woven bone and enable quantification of woven bone apposition at the periosteal surfaces (Figure 4.6) using Bioquant image software (BQ OSTEO v.7.20.10). Histological measurements included woven bone area and resorption pits per area within woven bone. The average measurements for the two sections were used for the subsequent analysis.

- Immunohistochemical apoptosis detection (Apoptag)

One section per tibia (taken at center of the microCT ROI) was used for immunohistochemical osteocyte apoptosis detection using the ApopTag Plus Fluorescein *In Situ* Apoptosis Detection Kit (Chemicon/Millipore, CA). Specifically, the assay detects apoptosis via fluorescent DNA fragmentation labeling, similar to a standard TUNEL assay (Gavrieli, Sherman et al. 1992). Once stained, sections were cover slipped using Propidium Iodide/Antifade Solution (Millipore, CA). Sections of female rodent mammary glands were used as positive controls, due to extensive apoptosis occurring in the tissue three to five days after weaning of rat pups (Strange, Friis et al. 1995). All sections were imaged immediately using appropriate fluorescent filters (Figure 4.7). Histological measurements included number of apoptosis positive osteocytes per cortical area. These measurements were determined while omitting woven bone areas.

Statistics and graph nomenclature

For ease of comparison between different time points, the term Delta is used to indicate differences between contra-lateral limbs:

Delta = Left tibia – Right tibia = Damaged tibia – Undamaged tibia

This term will be used throughout the presentation of the results.

To compare damaged to undamaged contra-lateral sides, paired t-tests were used. A two-way ANOVA with a post hoc correction was used for comparisons of deltas between experimental groups (WB/HS) and between deltas at different time points. Significance was defined as $p \leq 0.05$. The analysis was performed using SPSS statistical software (SPSS, Chicago, IL).

Results

Animal health

The starting body mass at day 0 was not significantly different between the weight bearing and hindlimb suspended group (Table 4.2). By day 14, animals in the WB group had significantly increased their weight by 2.7%, while the HS group had significantly lost 4.2% weight (Figure 4.8). Common for both groups was a slight decline in weight (day 18) after loading at day 14, while this was followed by a slight incline in body weight at day 35. Both incline and decline for all groups were non-significant (Figure 4.8).

Microcomputed tomography (microCT)

Cross sectional microCT from the center of the ROI indicated that less mineralized bone had been deposited at the periosteal surface of both the WB and HS groups (Figure 4.9). In accordance with this observation, microCT analysis showed a significant increase in delta tissue mineral content (TMC) at day 35 for the WB group compared to WB at day 0, which was also significantly greater than for the HS group at

day 35 (Figure 4.10). Similarly, the delta cortical area was significantly increased at day 35 for both groups, with the WB group being significantly greater than the HS group at that day (Figure 4.11). Finally the delta marrow area was significantly decreased at day 35 for the WB group, while the HS group had a significant increase at day 35 (Figure 4.12). For a complete listing of the specific microCT data, please refer to Table 4.3.

Picro-Sirius Red stain (woven bone formation)

Sections stained with Picro-Sirius Red indicated that significant initial woven bone formation had occurred at day 18 for both the WB and HS group. At day 35 this had increased significantly for both groups as the woven bone became more mineralized, with the WB group having significantly more woven bone deposited than the HS group (Figure 4.13).

Basic fuchsin stain (microdamage quantification)

For microdamage quantification under confocal microscopy, sections stained with basic fuchsin showed that significant amounts of microdamage were similarly induced at day 14 for both the WB and HS group due to the loading regime (Figure 4.14). The crack surface density was smaller for the HS group compared to WB at day 14, indicating that the produced cracks might have been smaller in length overall (Figure 4.15). The WB group showed a significant decrease in microdamage from day 14 to day 35, while the significant damage remained the same for the HS group over the three time points (Figure 4.14). A similar significant trend was observed for the WB group for the crack surface

density (Figure 4.15). For a complete listing of the specific basic fuchsin data, please refer to Table 4.4.

Osteocyte apoptosis

Detection of osteocyte apoptosis with Apoptag revealed that the damage induced by fatigue loading at day 14 resulted in similar and significant increases in apoptotic osteocytes in the cortical bone for the WB and HS group (Figure 4.16). The number of apoptotic osteocytes decreased significantly for both groups from day 14 to day 18, and from day 18 to day 35, but remained similar between WB and HS at all days (Figure 4.16). For a complete listing of the specific osteocyte apoptosis detection data, please refer to Table 4.5.

Flow cytometry

FACS showed that while delta CD11b was significantly different than zero immediately following loading at day 14 for the HS group, this becomes non-significant for day 18 and day 35 (Figure 4.17). The WB group, however, showed a decline in delta CD11b from day 14, through day 18 and day 35, where it was significantly lower than zero and significantly different from the HS group at day 35 (Figure 4.17). The results for delta CD117 showed no significant difference from zero for either group until day 35, when the two groups became significantly different. The HS group was significantly lower than zero, while the WB group showed an increasing trend at day 35 (Figure 4.18). For a complete listing of the specific flow cytometry data, please refer to Table 4.6.

ELF97 (TRAP)

TRAP staining using ELF97 phosphate showed a significant increase in delta TRAP positive intra cortical resorption pits for day 18 and day 35 for the WB group, while the same held true for day 18 for the HS group (Figure 4.19). In addition, data showed a strong increasing trend over time for the WB group, but not the HS group, which showed no difference at day 35 (Figure 4.19). The delta percent TRAP positive periosteal perimeter showed a significant increase from day 14 and 18 to day 35 for the WB group, whereas only a trend was found for the HS group for similar days (Figure 4.20). The delta percent TRAP positive endosteal perimeter showed no difference across the three time points within each group; however a significant difference was found between WB and HS at day 28, which ceased at day 35 (Figure 4.21). For a complete listing of the ELF 97 TRAP and Picro-Sirius Red data, please refer to Table 4.7.

Discussion

Morphologic and histological examinations from microCT and Picro-Sirius Red staining revealed that the damage induced a stress fracture response, which at day 18 and 35 resulted in a significant increase in woven bone apposition for both WB and HS, with the WB group being significantly greater than the HS group. This corresponds to what has been shown in previous animal models, where fatigue loading induced woven bone formation, which was both dependent on and proportional to the amount of induced microdamage (Tami, Nasser et al. 2003; Matsuzaki, Wohl et al. 2007; Uthgenannt, Kramer et al. 2007). Periosteal woven bone formation after fatigue damage has also been shown to aid in the rapid recovery of whole bone strength while increasing fatigue life

(Silva and Touhey 2007; Uthgenannt, Kramer et al. 2007). Hence, not only does a significant amount of damage remain in animals that were hindlimb suspended, but the protective mechanism that the formation of woven bone provides was not present, suggesting that whole bone strength remains low in a disuse setting following fatigue damage. One reason for this could be the significant reduction of blood flow in HS models (Bloomfield 2006), since it has been shown that there is a correlation between increased fatigue loading, increased vascularity and increased woven bone formation (Silva, Uthgenannt et al. 2006). In addition, the significantly reduced woven bone response for the HS group could be due to the reduction in osteoblast responsiveness and bone formation rate associated with hindlimb suspension (Bloomfield, Allen et al. 2002; Cao, Kurimoto et al. 2007).

It has been shown that excessive fatigue loading results in woven bone formation in addition to increased intra-cortical resorption (Hsieh and Silva 2002).

The intra-cortical resorption response, which has been observed in several studies (Burr, Martin et al. 1985; Burr and Martin 1993; Mori and Burr 1993; Bentolila, Boyce et al. 1998; Verborgt, Gibson et al. 2000; Lee, Staines et al. 2002), is increased in the WB group following fatigue damage but not in the HS group. The evidence from immunohistochemistry indicates that the induced microdamage resulted in similar amounts of osteocyte apoptosis within the cortical bone of WB and HS animals. In addition a similar decay of apoptotic osteocytes from day 14 to day 18 and 35 was observed, which was expected, given that the process of apoptosis from onset to phagocytosis of the apoptotic osteocyte can take anywhere from two to three hours to one to two days (Jilka, Weinstein et al. 2007).

Since we have induced similar amounts of microdamage, resulting in similar amounts of osteocyte apoptosis in the WB and HS animals, the lack of microdamage removal and absence of intra-cortical resorption pits for the HS group could be due to either a divergence of the "targeting" mechanism of normal targeted remodeling or a lack of osteoclast recruitment following microdamage. Examining the HSC and monocyte population of the osteoclast lineage with flow cytometry revealed that a significant decrease in monocytes and increase in HSCs had occurred at day 35 in the WB animals, with no changes for the HS animals. This suggests that a shift in the osteoclast lineage occurred following induction of microdamage. The evidence from flow cytometry suggests a significant recruitment of pre-osteoclast cells to the damaged regions, resulting in a need for differentiation of monocytes into pre-osteoclasts. This "depletion" of monocytes would cause a demand for more, resulting in an increase in the HSC population for the WB group. Hence, the flow cytometry results indicate that the histological evidence of "no damage removal" at day 35 for HS was due to a lack of osteoclast activation and not a change in the targeting mechanisms of remodeling.

The lack of osteoclast activation could be due to a decrease in interstitial fluid flow which results from disuse (Stevens, Meays et al. 2006), particularly given that several studies suggest that load-induced fluid flow may be necessary to provide sufficient transport of larger molecules such as proteins to and from osteocytes (Knothe Tate, Knothe et al. 1998; Knothe Tate, Niederer et al. 1998). In addition, the evidence that osteocyte apoptotic bodies induce osteoclastogenesis leading to localized bone resorption (Kogianni, Mann et al. 2008) suggest that during hindlimb suspension or disuse, the 'activating' signal for resorption of microdamage is withheld by the lack of

fluid flow through the canalicular system, resulting in a futile delivery of resorption initiating signals from the apoptotic osteocytes.

Since bone does not appear to recognize microdamage in bone not mechanically loaded, the woven bone response in the HS group could be due to the elevated strain levels experienced during the act of loading. It has been shown that the primary incentive for woven bone formation following microdamage induction is recovery of whole bone strength (Silva and Touhey 2007; Uthgenannt, Kramer et al. 2007), and that the woven bone response is proportional to the amount of induced microdamage (Tami, Nasser et al. 2003; Matsuzaki, Wohl et al. 2007; Uthgenannt, Kramer et al. 2007). Loading causes elevated strain levels in the bone, which increases with damage accumulation due to a further loss of stiffness. Thus the increase in woven bone response with more damage could be due to an elevation in applied strain, as a result of the increase in damage rather than the direct presence of the damage. Hence, although the bone cannot "sense" the damage in a disuse setting, the act of inducing the damage can provide the signal to induce woven bone through elevated strain levels.

This study demonstrates that physiological loading is necessary for the remodeling repair response to occur following significant accumulation of microdamage, since disuse alters the response to microdamage through a reduction in woven bone production and the lack of resorption of microdamage.

The data suggests that elderly individuals with severely limited activity may accumulate further microdamage, therefore increasing fracture risk. The change in remodeling due to disuse could have consequences for how stress fractures are treated, not only in the elderly, but also in the general population. The current treatment of stress

fractures by casting and/or prevention of load-bearing may therefore need to be reconsidered, as the repair of microdamage may proceed more effectively in combination with mechanical usage.

Early evidence for this has been found in treatment of running injuries, where previous treatment methods for stress fractures associated with long distance running prescribe up to 12 weeks of therapy (dominantly non-weight-bearing) before returning to a normal running schedule (Ballas, Tytko et al. 1997). Recent studies (without an experimental basis) have decreased the recovery period by implementing earlier cross-training, enabling the athlete to return to function in only seven weeks (Knobloch, Schreibmueller et al. 2007). The results from these early clinical studies parallel the results in this study by indicating that the removal of load (i.e. by casting/disuse) indeed causes an impaired repair process.

Lastly and most importantly, while a variety of studies have proposed that the repair of microdamage is triggered by cell apoptosis, these results suggest that this mechanism may be insufficient without the stimulus associated with mechanical usage.

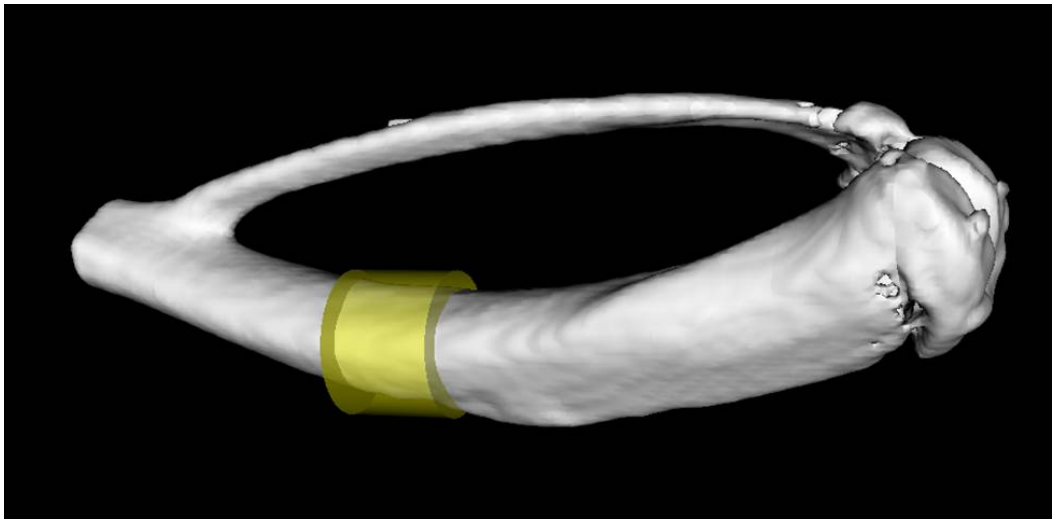

Figure 4.1. MicroCT image of tibia with ROI indicated

Region of interest (ROI) indicated with yellow, has a length of 4 mm with its center located 8mm proximal to the tibia/fibula junction.

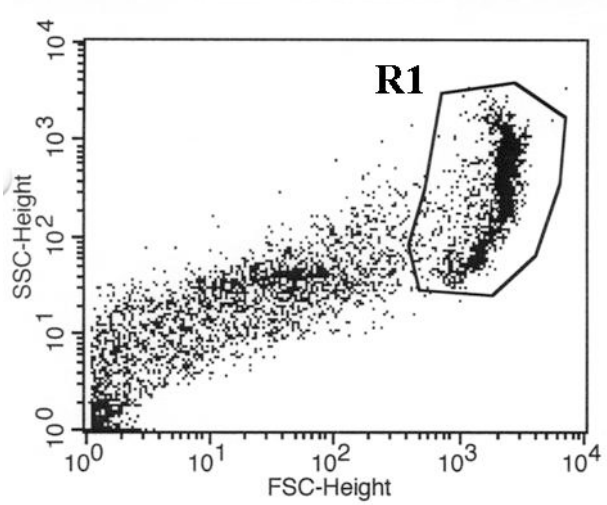

Figure 4.2. Side/forward (SSC/FSC) light scatter profile of cells for flow cytometry

R1: Inclusion region, containing MSC's and monocytes

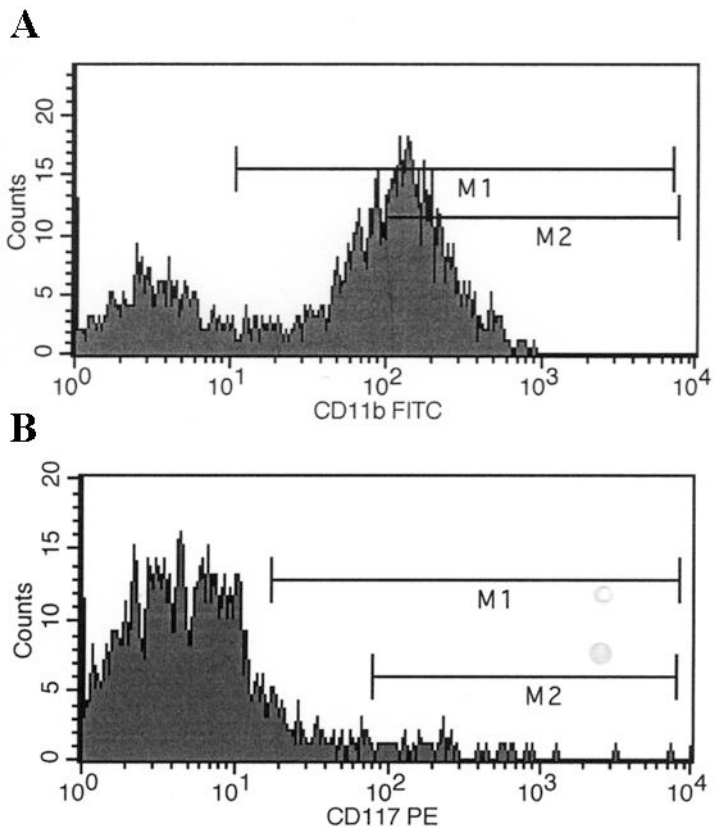

Figure 4.3. Fluorescence intensity histograms

A: CD11b fluorescence intensity histogram (M2 region: Location of positive cells)
B: CD117 fluorescence intensity histogram (M1 region: Location of positive cells)

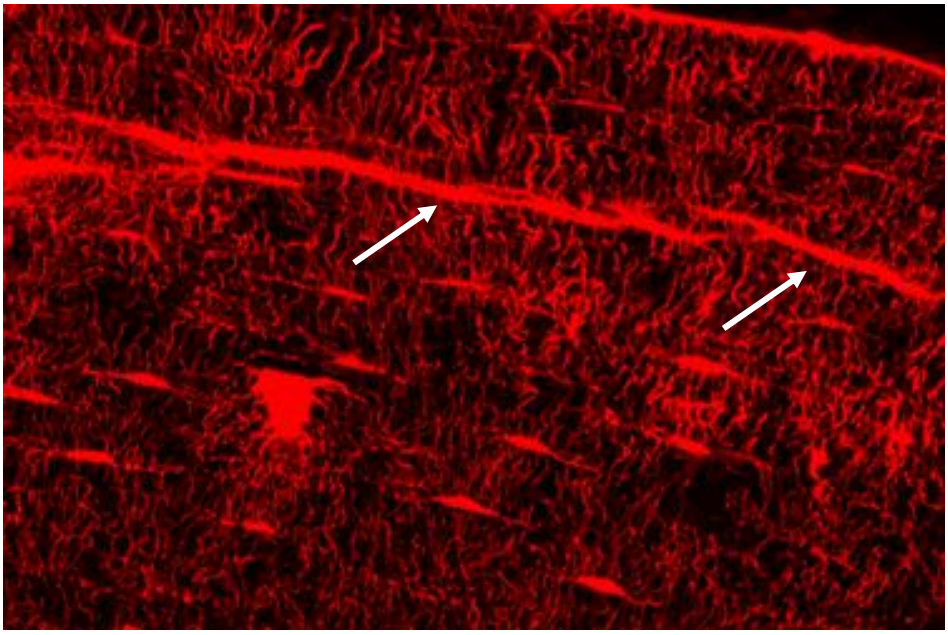

Figure 4.4. Representative microscope image of Basic Fuchsin stained section

White arrows indicate damage within cortical section at the periosteal surface.

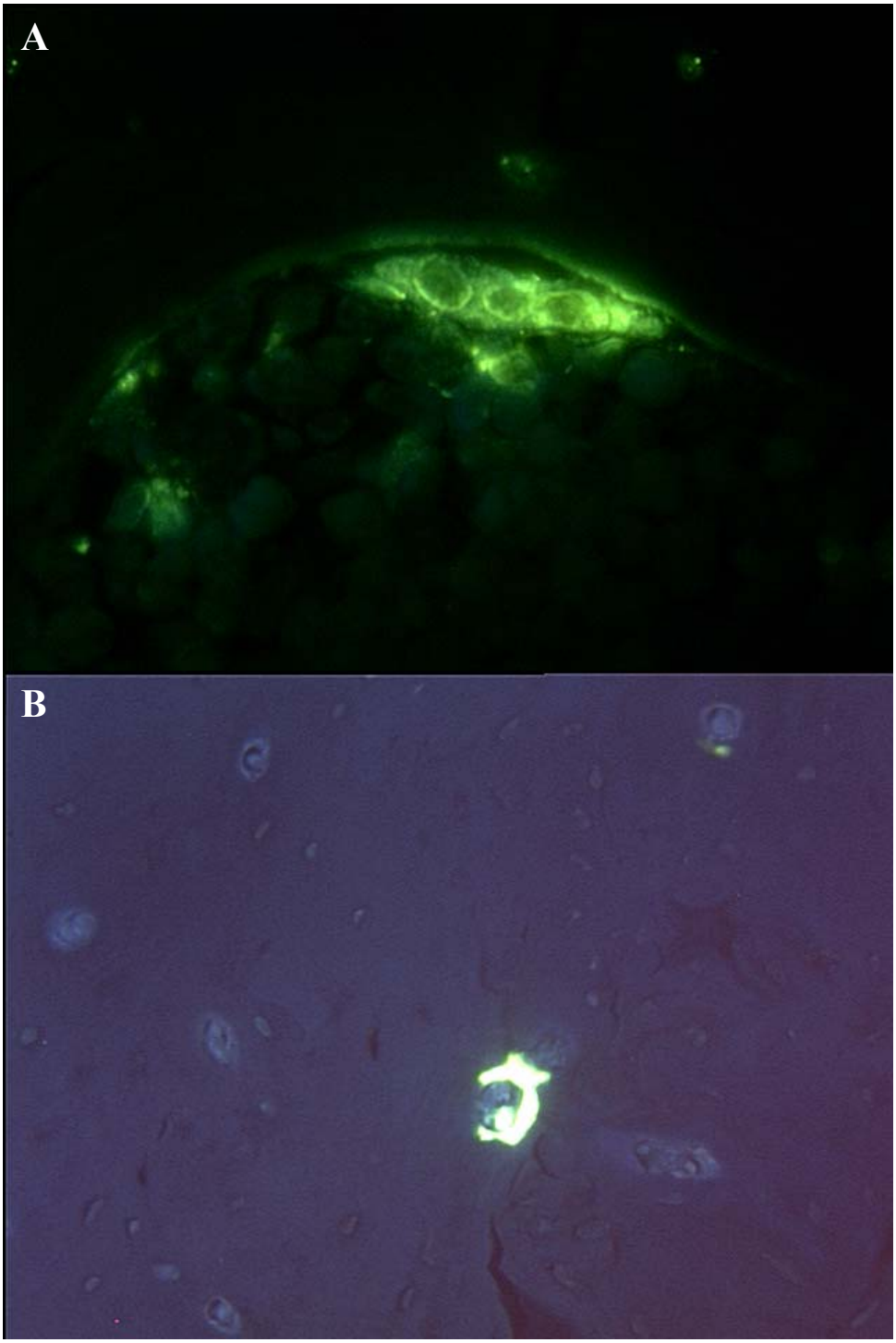

Figure 4.5. Representative microscope image of ELF97 (TRAP) stained section

A: TRAP positive osteoclast within resorption pit
B: TRAP positive resorption pit within cortex

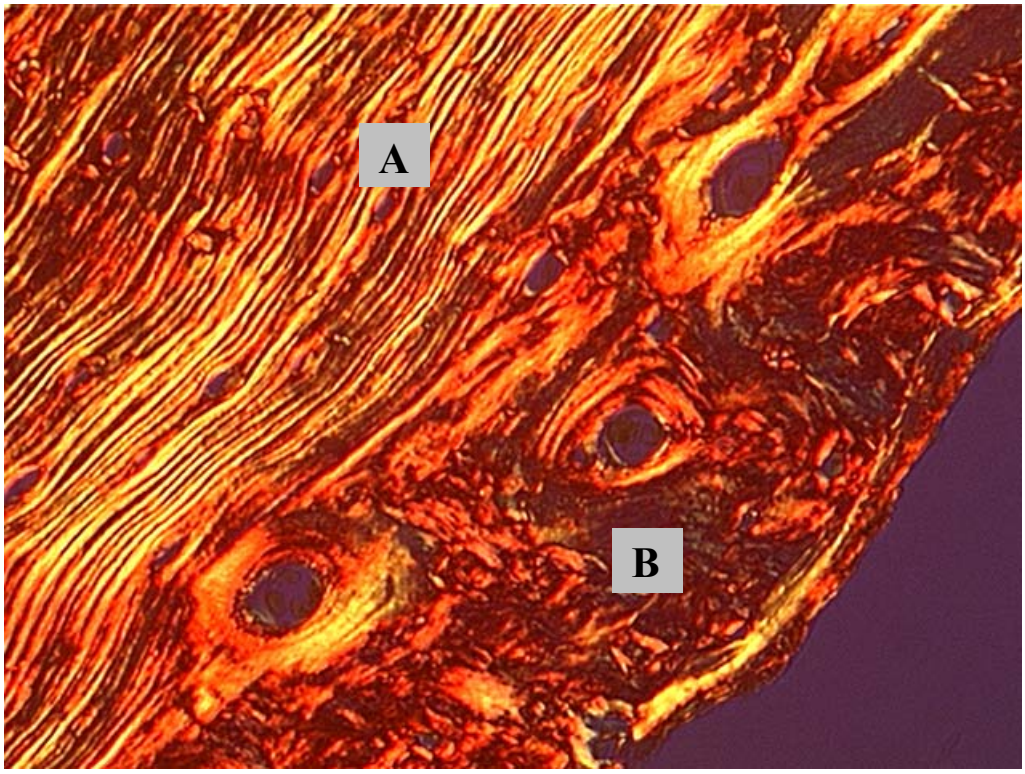

Figure 4.6. Representative microscope image of Picro-Sirius Red stained section

A: Lamellar bone
B: Woven bone

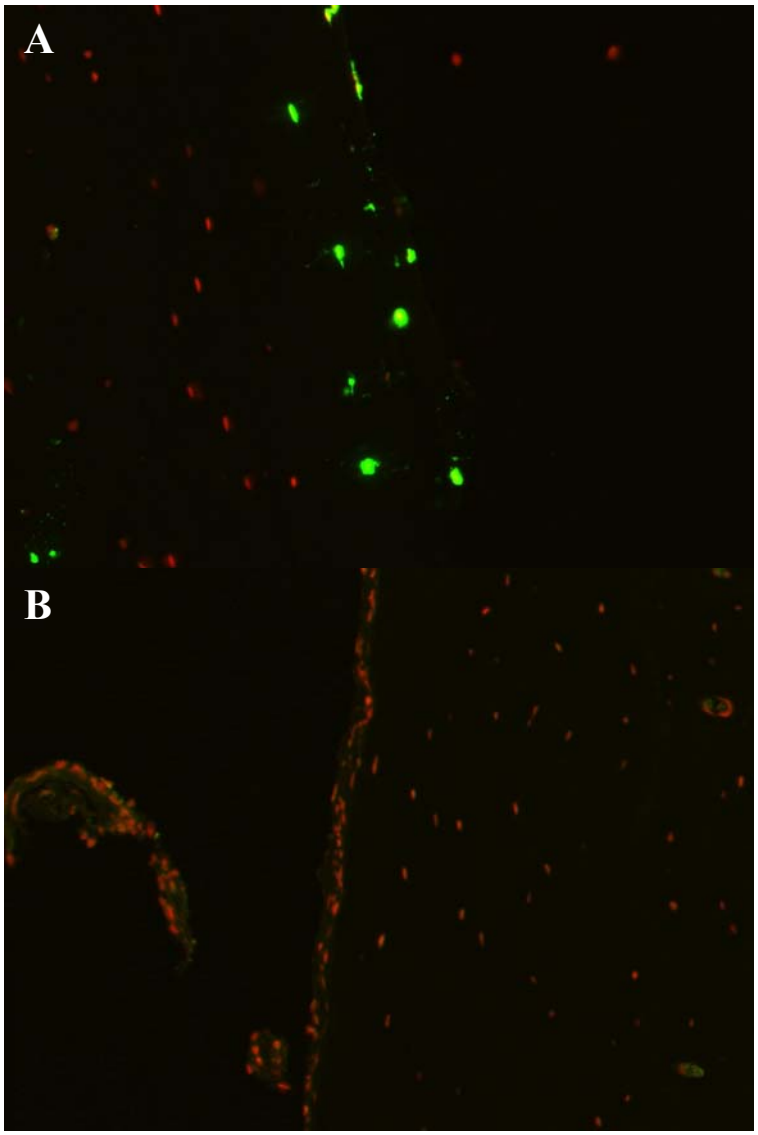

Figure 4.7. Representative microscope image of immunohistochemical stained section for apoptosis

A: Apoptotic osteocytes (green) at the periosteal surface of damaged cortical bone
B: Periosteal surface of contra lateral section (non-damaged cortical bone)

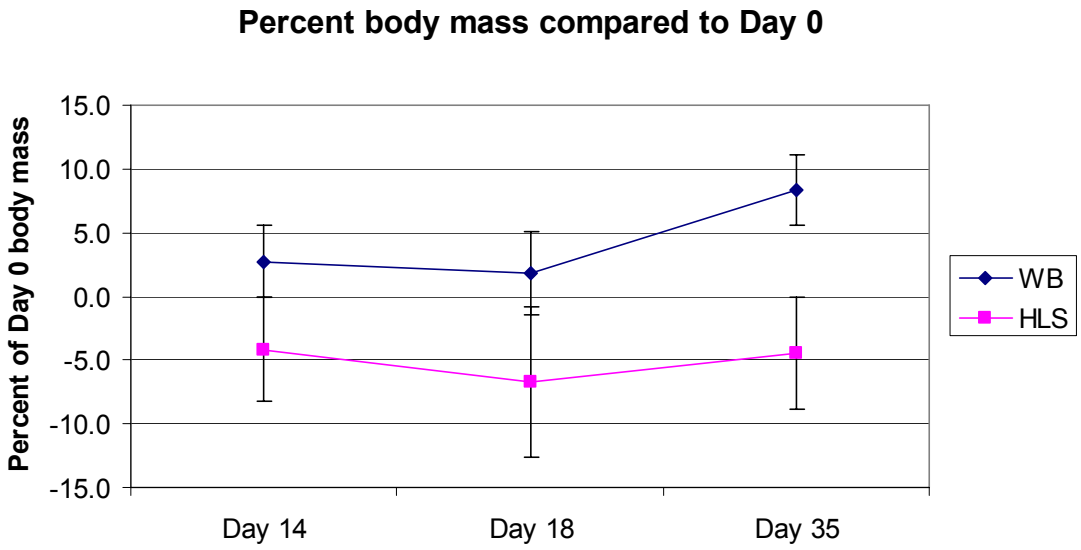

Figure 4.8. Percent body mass compared to day 0

Error bars indicate standard deviations.

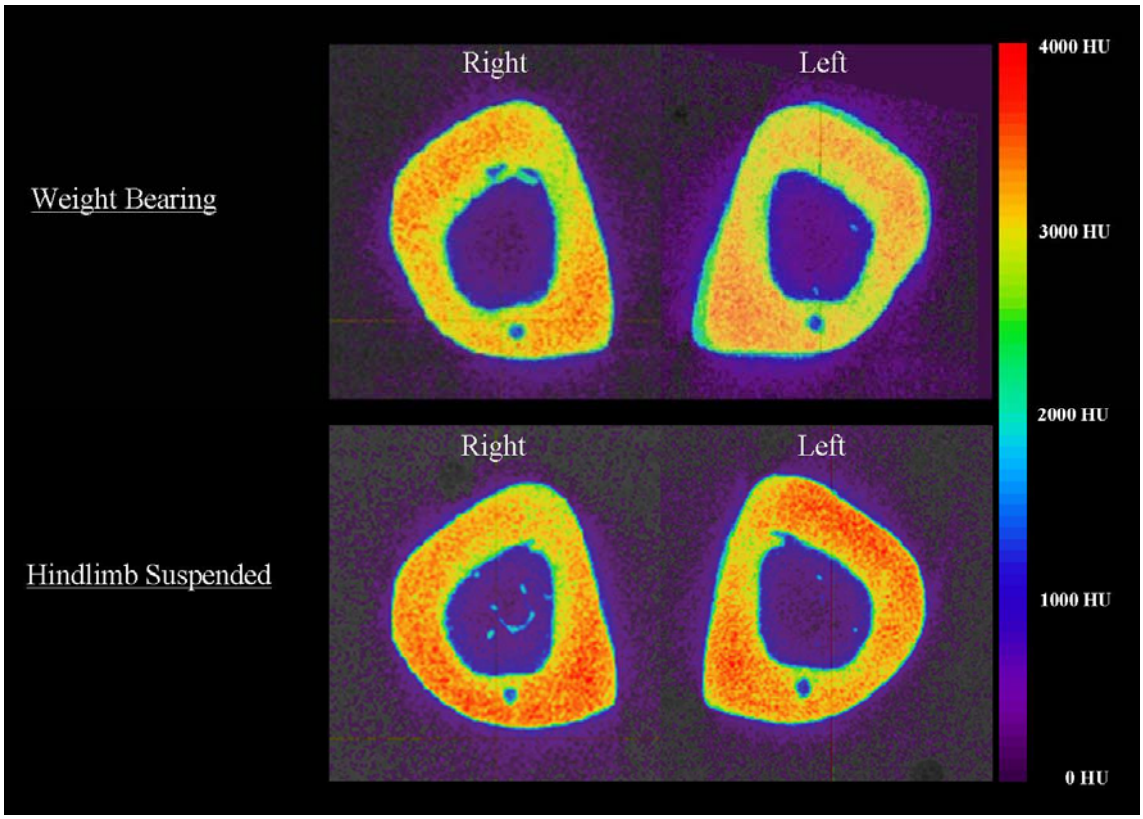

Figure 4.9. MicroCT cross-sectional mid-ROI images from specimens on day 35

Scale on the right indicates voxel HU, with higher HU indicating more mineralized tissue.

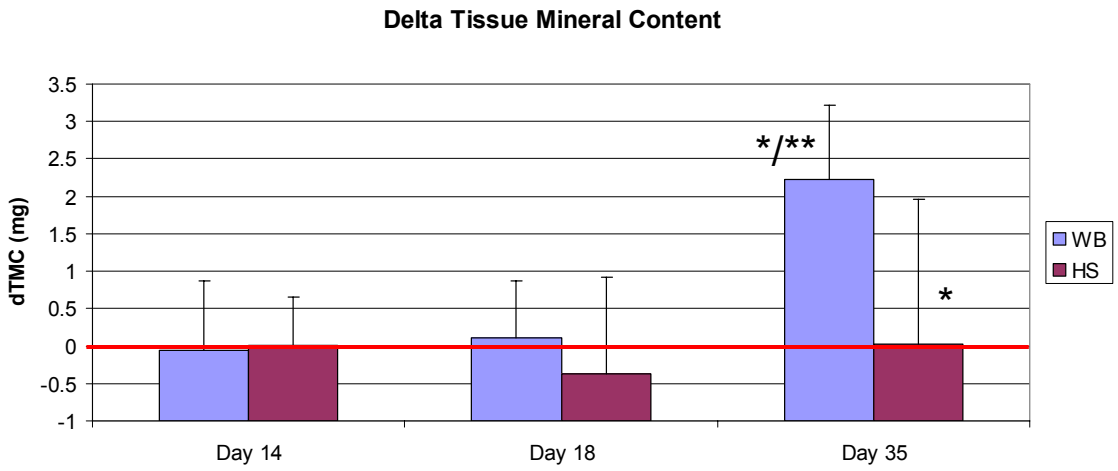

Figure 4.10. Delta tissue mineral content

Single asterisk (*), indicate significant difference between WB vs. HS at that day. Double asterisks (**), indicate significant difference between R vs. L leg for that group on the particular day (i.e. delta is significantly different from zero). Error bars indicate standard deviations.

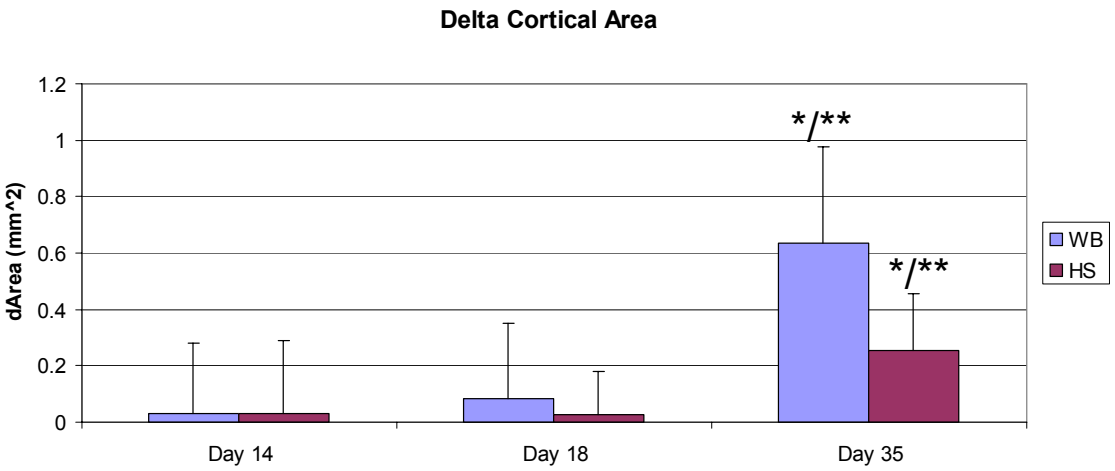

Figure 4.11. Delta cortical area

Single asterisk (*), indicate significant difference between WB vs. HS at that day. Double asterisks (**), indicate significant difference between R vs. L leg for that group on the particular day (i.e. delta is significantly different from zero). Error bars indicate standard deviations.

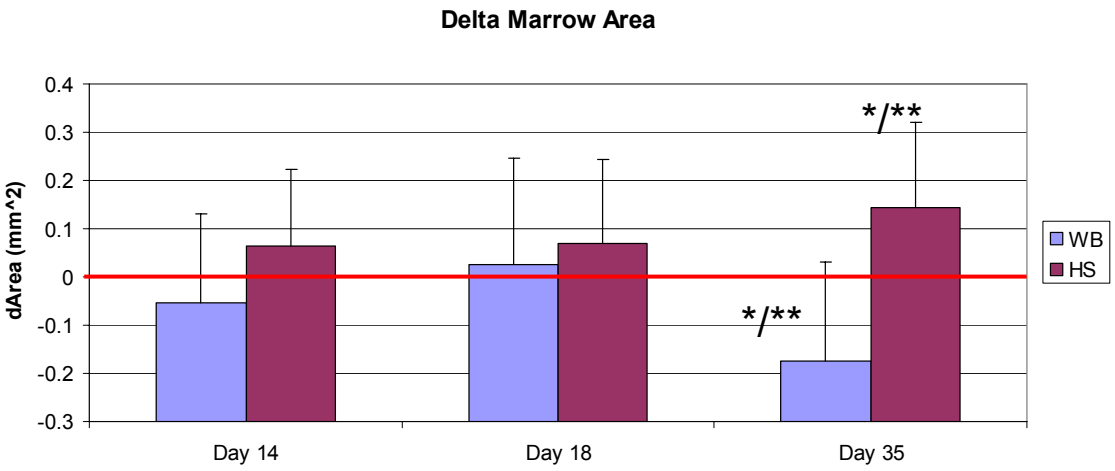

Figure 4.12. Delta marrow area

Single asterisk (*), indicate significant difference between WB vs. HS at that day. Double asterisks (**), indicate significant difference between R vs. L leg for that group on the particular day (i.e. delta is significantly different from zero). Error bars indicate standard deviations.

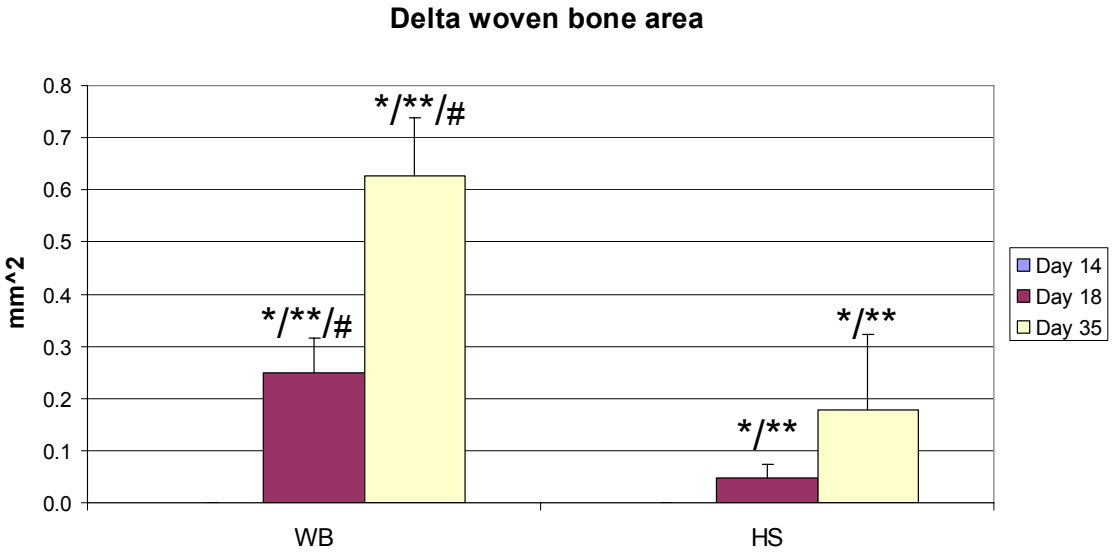

Figure 4.13. Delta woven bone area

Single asterisk (*), indicate significant difference between WB vs. HS at that day. Double asterisks (**), indicate significant difference between R vs. L leg for that group on the particular day (i.e. delta is significantly different from zero). Single pound (#), indicate significant difference between day 18 and 35 within the specific group (WB or HS). Error bars indicate standard deviations.

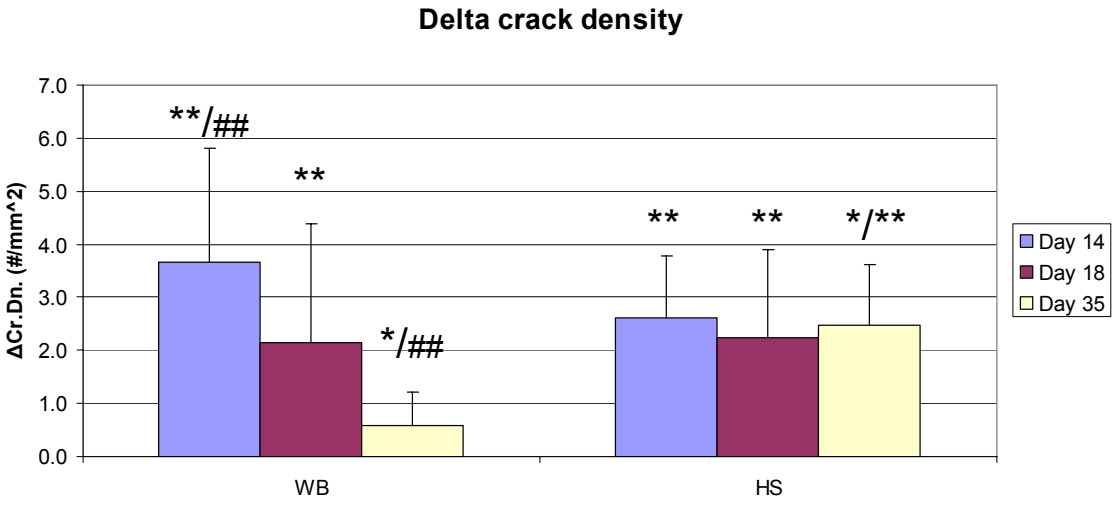

Figure 4.14. Delta crack density

Delta crack density was determined while omitting woven bone areas.

Single asterisk (*), indicate significant difference between WB vs. HS at that day. Double asterisks (**), indicate significant difference between R vs. L leg for that group on the particular day (i.e. delta is significantly different from zero). Single pound (#), indicate significant difference between day 18 and 35 within the specific group (WB or HS). Double pound (##), indicate significant difference between day 14 and 35 within the specific group (WB or HS). Error bars indicate standard deviations.

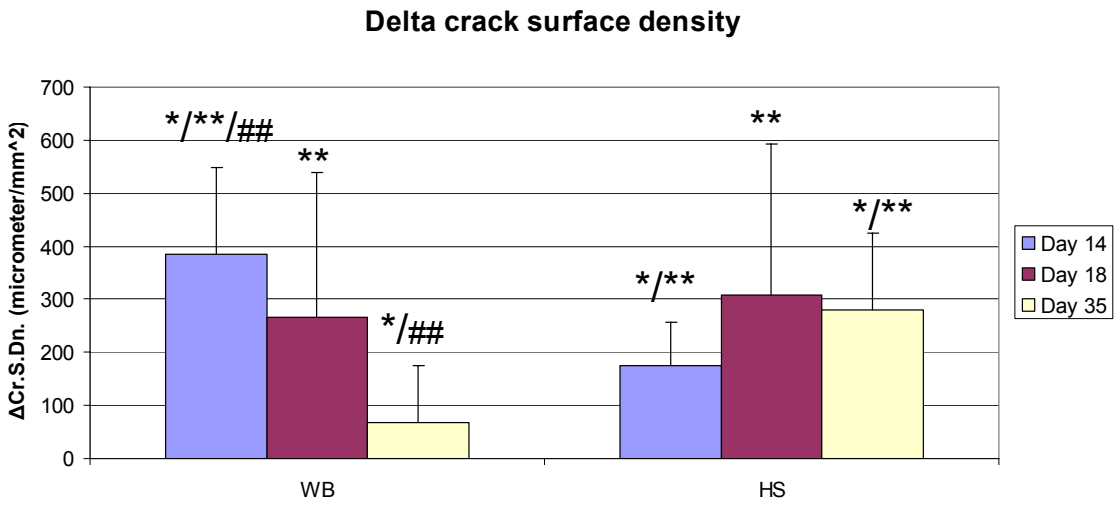

Figure 4.15. Delta crack surface density

Delta crack surface density was determined while omitting woven bone areas.

Single asterisk (*), indicate significant difference between WB vs. HS at that day. Double asterisks (**), indicate significant difference between R vs. L leg for that group on the particular day (i.e. delta is significantly different from zero). Single pound (#), indicate significant difference between day 18 and 35 within the specific group (WB or HS). Double pound (##), indicate significant difference between day 14 and 35 within the specific group (WB or HS). Error bars indicate standard deviations.

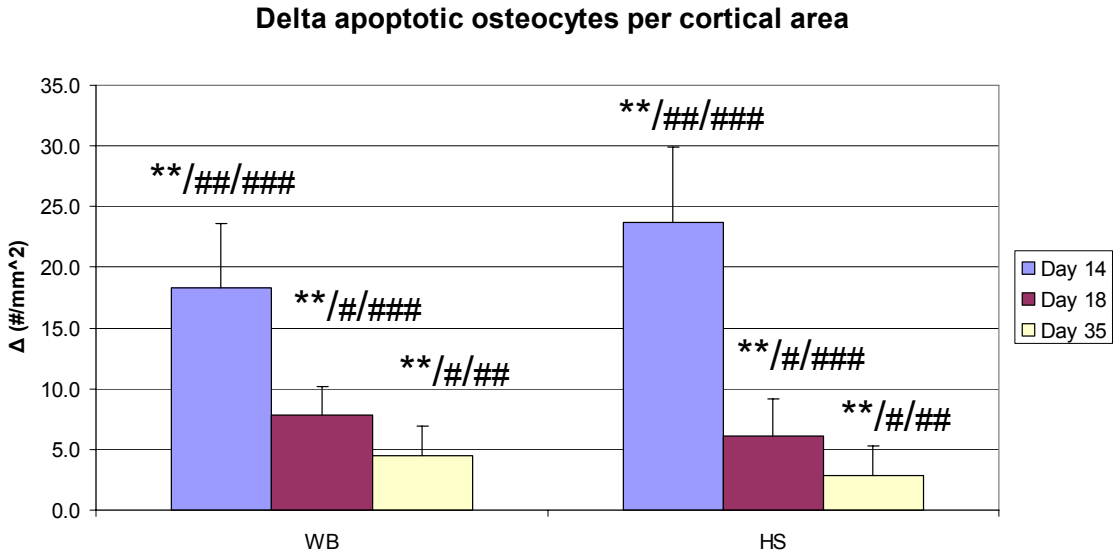

Figure 4.16. Delta apoptotic osteocytes per cortical area

Number of apoptotic osteocytes (per cortical area) was determined while omitting woven bone areas.

Single asterisk (*), indicate significant difference between WB vs. HS at that day. Double asterisks (**), indicate significant difference between R vs. L leg for that group on the particular day (i.e. delta is significantly different from zero). Single pound (#), indicate significant difference between day 18 and 35 within the specific group (WB or HS). Double pound (##), indicate significant difference between day 14 and 35 within the specific group (WB or HS). Triple pound (###), indicate significant difference between day 14 and 18 within the specific group (WB or HS). Error bars indicate standard deviations.

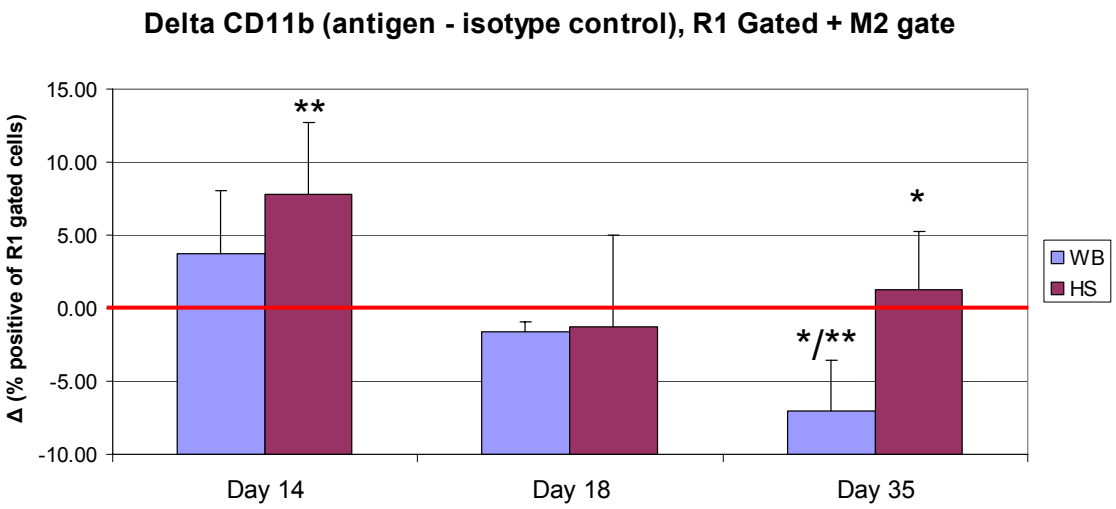

Figure 4.17. Delta CD11b

Single asterisk (*), indicate significant difference between WB vs. group at that day. Double asterisks (**), indicate significant difference between R vs. L leg for that group on the particular day (i.e. delta is significantly different from zero). Error bars indicate standard deviations.

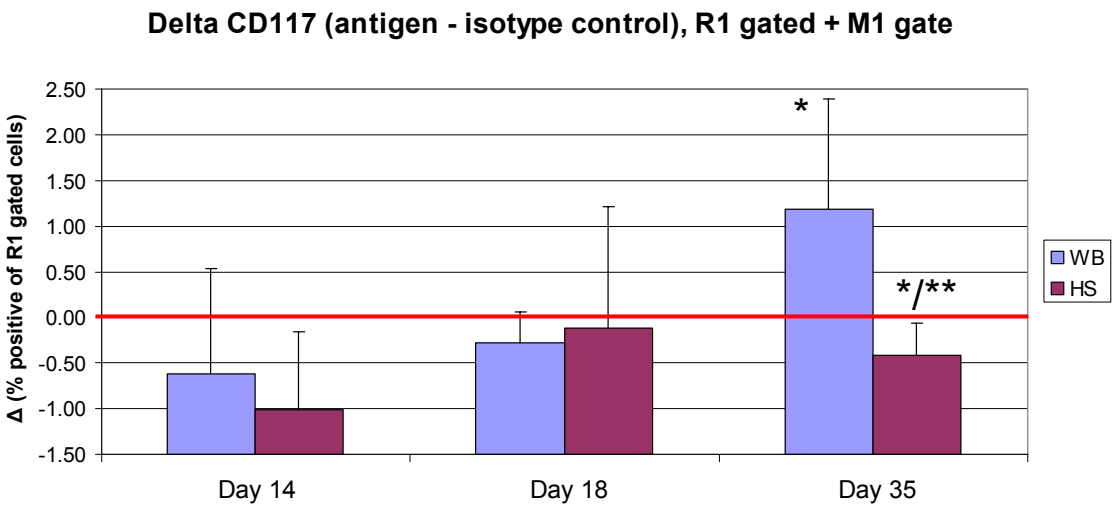

Figure 4.18. Delta CD117

Single asterisk (*), indicate significant difference between WB vs. group at that day. Double asterisks (**), indicate significant difference between R vs. L leg for that group on the particular day (i.e. delta is significantly different from zero). Error bars indicate standard deviations.

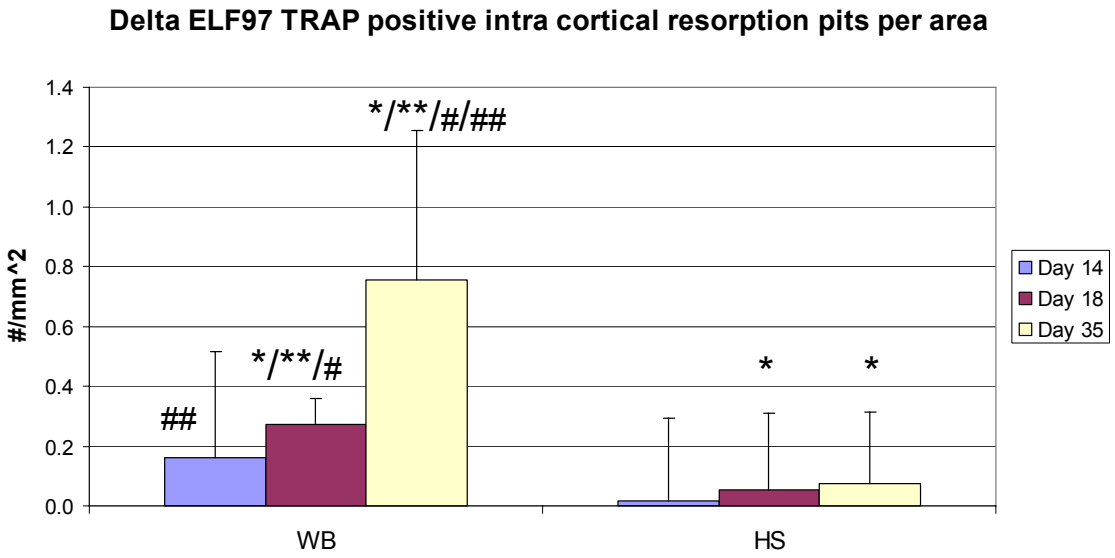

Figure 4.19. Delta TRAP positive resorption pits

Number of TRAP positive intra cortical resorption pits (per cortical area) was determined while omitting woven bone areas.

Single asterisk (*), indicate significant difference between WB vs. group at that day. Double asterisks (**), indicate significant difference between R vs. L leg for that group on the particular day (i.e. delta is significantly different from zero). Single pound (#), indicate significant difference between day 18 and 35 within the specific group (WB or HS). Double pound (##), indicate significant difference between day 14 and 35 within the specific group (WB or HS). Error bars indicate standard deviations.

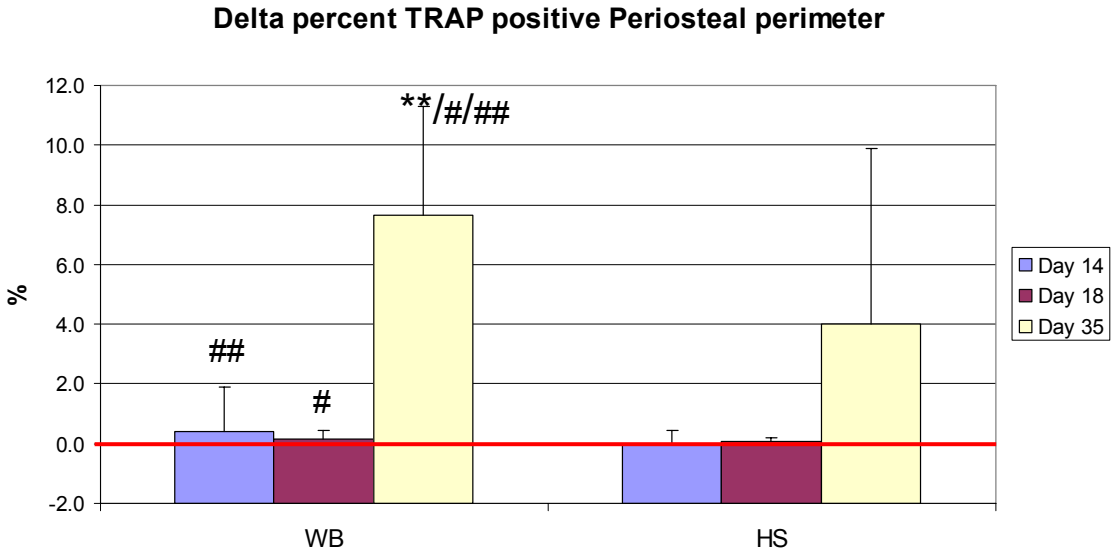

Figure 4.20. Delta percent TRAP positive periosteal perimeter

Percent TRAP positive periosteal perimeter was done using the outer most surface available (i.e. including any woven bone apposition).

Single asterisk (*), indicate significant difference between WB vs. HS at that day. Double asterisks (**), indicate significant difference between R vs. L leg for that group on the particular day (i.e. delta is significantly different from zero). Single pound (#), indicate significant difference between day 18 and 35 within the specific group (WB or HS). Double pound (##), indicate significant difference between day 14 and 35 within the specific group (WB or HS). Triple pound (###), indicate significant difference between day 14 and 18 within the specific group (WB or HS). Error bars indicate standard deviations.

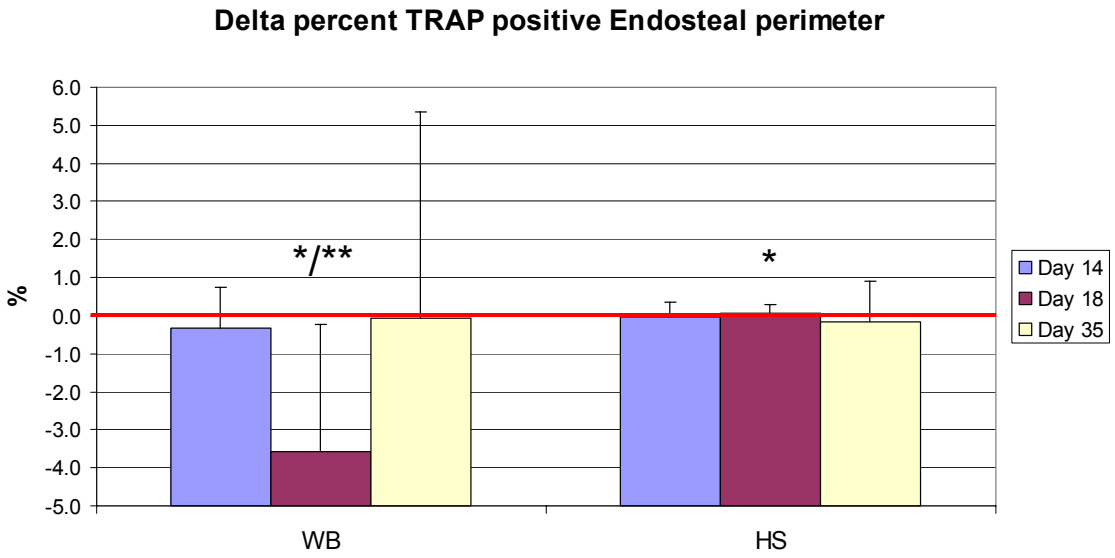

Figure 4.21. Delta percent TRAP positive endosteal perimeter

Percent TRAP positive endosteal perimeter was done using the inner most surface available (i.e. including any woven bone apposition).

Single asterisk (*), indicate significant difference between WB vs. HS at that day. Double asterisks (**), indicate significant difference between R vs. L leg for that group on the particular day (i.e. delta is significantly different from zero). Single pound (#), indicate significant difference between day 18 and 35 within the specific group (WB or HS). Double pound (##), indicate significant difference between day 14 and 35 within the specific group (WB or HS). Triple pound (###), indicate significant difference between day 14 and 18 within the specific group (WB or HS). Error bars indicate standard deviations.

	WB	HS
Avg. (με/N)	-65.15	-56.55
St.Dev.	6.31	18.87

Table 4.1. Slope of lateral strain vs. applied force relationship

	WB	HS
Avg. (g)	435.6	426.4
St.Dev.	33.5	31.5

Table 4.2. Starting body mass at day 0

				TMC (mg)	TMD (mg/cc)	Ixx (mm^4)	Iyy (mm^4)	Izz (mm^4)	Marrow Area (mm^2)	Cortical Area (mm^2)
Day 14	WB	Left	Avg	19.12	879.82	5.96	4.05	10.01	2.66	5.15
			St.Dev.	1.47	8.74	0.90	0.60	1.44	0.25	0.41
		Right	Avg	19.17	879.43	6.01	4.06	10.07	2.72	5.12
			St.Dev.	1.37	17.72	0.77	0.52	1.26	0.31	0.33
		Delta (L - R)	Avg	-0.05	0.39	-0.05	-0.01	-0.06	-0.05	0.03
			St.Dev.	0.92	14.16	0.67	0.32	0.92	0.19	0.25
	HS	Left	Avg	18.72	872.39	5.93	3.95	9.87	2.70	4.91
			St.Dev.	1.48	16.77	0.64	0.37	0.93	0.23	0.39
		Right	Avg	18.71	874.29	5.83	3.94	9.77	2.64	4.88
			St.Dev.	1.56	18.80	0.59	0.49	1.01	0.26	0.41
		Delta (L - R)	Avg	0.01	-1.89	0.10	0.01	0.10	0.06	0.03
			St.Dev.	0.65	18.12	0.32	0.27	0.43	0.16	0.26
Day 18	WB	Left	Avg	18.93	889.10	5.65	3.77	9.42	2.49	4.88
			St.Dev.	0.86	18.24	0.65	0.38	0.96	0.31	0.38
		Right	Avg	18.82	881.64	5.77	3.74	9.52	2.46	4.79
			St.Dev.	1.12	18.50	0.65	0.34	0.89	0.24	0.36
		Delta (L - R)	Avg	0.11	7.46	-0.12	0.03	-0.10	0.03	0.08
			St.Dev.	0.77	18.84	0.31	0.20	0.40	0.22	0.26
	HS	Left	Avg	18.45	878.89	5.73	3.73	9.46	2.63	4.95
			St.Dev.	1.09	13.40	0.67	0.51	1.12	0.26	0.36
		Right	Avg	18.82	874.71	5.65	3.75	9.41	2.56	4.92
			St.Dev.	1.70	15.51	0.81	0.52	1.30	0.33	0.36
		Delta (L - R)	Avg	-0.37	4.19	0.08	-0.02	0.05	0.07	0.02
			St.Dev.	1.28	14.71	0.59	0.25	0.81	0.17	0.16
Day 35	WB	Left	Avg	21.57	869.57	6.93	5.12	12.04	2.63	5.68
			St.Dev.	1.23	16.62	0.64	0.50	1.06	0.23	0.40
		Right	Avg	19.34	866.43	6.31	4.42	10.73	2.80	5.04
			St.Dev.	1.31	16.78	0.55	0.92	1.39	0.28	0.33
		Delta (L - R)	Avg	**2.23**	3.14	**0.62**	**0.69**	**1.31**	**-0.18**	**0.64**
			St.Dev.	0.99	15.87	0.45	1.00	1.33	0.21	0.34
	HS	Left	Avg	19.60	874.63	6.28	4.43	10.71	2.85	5.15
			St.Dev.	1.25	19.82	0.56	0.55	1.06	0.34	0.35
		Right	Avg	19.58	876.74	6.02	4.10	10.12	2.71	4.90
			St.Dev.	2.65	23.13	0.67	0.48	1.07	0.32	0.35
		Delta (L - R)	Avg	0.02	-2.11	0.26	**0.33**	**0.59**	**0.14**	**0.25**
			St.Dev.	1.94	14.30	0.54	0.33	0.81	0.18	0.21

Table 4.3. Specific microCT data for ROI

Values in bold indicate significant difference between left and right tibiae (i.e. value for delta is significantly different from zero).

				Cortical area (mm^2)	Cr.Dn. (cracks/mm^2)	Cr.S.Dn. (μm/mm^2)
Day 14	WB	Left	Avg	5.43	4.28	453.83
			St.Dev.	0.22	2.07	146.44
		Right	Avg	5.48	0.63	69.38
			St.Dev.	0.27	0.43	71.55
		Delta (L - R)	Avg	-0.05	**3.66**	**384.45**
			St.Dev.	0.12	2.16	163.33
	HS	Left	Avg	5.52	3.54	286.92
			St.Dev.	0.28	1.39	94.76
		Right	Avg	5.51	0.92	112.74
			St.Dev.	0.21	0.55	67.13
		Delta (L - R)	Avg	0.01	**2.62**	**174.18**
			St.Dev.	0.25	1.16	81.60
Day 18	WB	Left	Avg	5.39	2.88	408.92
			St.Dev.	0.40	2.29	279.27
		Right	Avg	5.30	0.74	142.02
			St.Dev.	0.40	0.30	69.65
		Delta (L - R)	Avg	0.09	**2.14**	**266.90**
			St.Dev.	0.31	2.24	271.57
	HS	Left	Avg	5.29	2.59	370.07
			St.Dev.	0.34	1.70	292.34
		Right	Avg	5.17	0.35	62.99
			St.Dev.	0.28	0.33	72.75
		Delta (L - R)	Avg	0.12	**2.25**	**307.08**
			St.Dev.	0.20	1.65	286.14
Day 35	WB	Left	Avg	5.69	1.40	162.59
			St.Dev.	0.36	0.56	87.23
		Right	Avg	5.72	0.83	94.36
			St.Dev.	0.31	0.32	36.26
		Delta (L - R)	Avg	-0.04	0.57	68.23
			St.Dev.	0.28	0.63	105.63
	HS	Left	Avg	5.41	2.95	321.97
			St.Dev.	0.39	1.37	165.98
		Right	Avg	5.45	0.47	40.99
			St.Dev.	0.50	0.33	29.36
		Delta (L - R)	Avg	-0.04	**2.48**	**280.98**
			St.Dev.	0.26	1.13	144.57

Table 4.4. Specific basic fuchsin data

Values in bold indicate significant difference between left and right tibiae (i.e. value for delta is significantly different from zero).

				# of apoptotic cortical osteocytes				Apop.osteo.per area
				Lateral	Medial	Posterior	**Total**	**#/(mm^2)**
Day 14	WB	Left	Avg	52.7	48.0	6.2	106.8	21.0
			St.Dev.	18.0	14.2	6.6	29.3	6.9
		Right	Avg	4.5	5.3	2.8	12.7	2.7
			St.Dev.	2.9	3.9	2.6	8.6	1.9
		Delta (L - R)	Avg	48.2	42.7	3.3	94.2	**18.3**
			St.Dev.	16.4	11.6	6.8	22.8	5.3
	HS	Left	Avg	48.0	70.0	6.6	124.6	26.4
			St.Dev.	16.4	20.9	4.1	24.2	5.3
		Right	Avg	6.4	4.0	2.6	13.0	2.7
			St.Dev.	5.0	2.3	2.1	6.5	1.3
		Delta (L - R)	Avg	41.6	66.0	4.0	111.6	**23.7**
			St.Dev.	19.7	22.0	4.0	29.6	6.2
Day 18	WB	Left	Avg	24.1	18.0	7.1	49.3	10.1
			St.Dev.	14.9	5.6	3.8	15.1	3.2
		Right	Avg	5.0	3.4	2.4	10.9	2.2
			St.Dev.	2.2	1.8	4.7	5.6	1.2
		Delta (L - R)	Avg	19.1	14.6	4.7	38.4	**7.9**
			St.Dev.	15.4	5.3	5.9	11.4	2.3
	HS	Left	Avg	12.9	20.1	4.7	37.7	7.7
			St.Dev.	5.2	10.1	3.1	14.4	3.3
		Right	Avg	2.7	2.7	2.9	8.3	1.7
			St.Dev.	1.4	2.9	2.3	2.6	0.5
		Delta (L - R)	Avg	10.1	17.4	1.9	29.4	**6.1**
			St.Dev.	5.1	10.0	3.3	13.7	3.1
Day 35	WB	Left	Avg	11.0	16.7	5.3	33.0	6.3
			St.Dev.	4.5	6.5	2.9	10.2	2.0
		Right	Avg	3.0	4.0	2.4	9.4	1.8
			St.Dev.	2.9	3.3	1.5	3.0	0.7
		Delta (L - R)	Avg	8.0	12.7	2.9	23.6	**4.4**
			St.Dev.	4.5	8.4	2.5	12.9	2.5
	HS	Left	Avg	9.1	13.1	4.1	26.4	5.2
			St.Dev.	4.9	6.8	4.5	8.7	2.0
		Right	Avg	3.8	5.1	2.4	11.3	2.4
			St.Dev.	2.0	2.6	2.3	5.9	1.4
		Delta (L - R)	Avg	5.4	8.0	1.8	15.1	**2.8**
			St.Dev.	6.3	7.2	3.7	11.0	2.5

Table 4.5. Specific osteocyte apoptosis detection data

Values in bold indicate significant difference between left and right tibiae (i.e. value for delta is significantly different from zero).

				CD11b % gated M2 gate	CD117 % gated M1 gate
Day 14	WB	Left	Avg	26.31	1.11
			St.Dev.	3.89	1.69
		Right	Avg	22.54	1.72
			St.Dev.	5.40	0.65
		Delta (L - R)	Avg	3.77	-0.61
			St.Dev.	4.29	1.15
	HS	Left	Avg	35.82	1.24
			St.Dev.	5.77	0.77
		Right	Avg	28.06	2.26
			St.Dev.	8.45	1.52
		Delta (L - R)	Avg	**7.76**	-1.01
			St.Dev.	4.98	0.85
Day 18	WB	Left	Avg	16.22	1.00
			St.Dev.	8.06	1.41
		Right	Avg	17.81	1.28
			St.Dev.	7.40	1.18
		Delta (L - R)	Avg	-1.58	-0.28
			St.Dev.	0.68	0.33
	HS	Left	Avg	22.27	-0.45
			St.Dev.	11.71	1.13
		Right	Avg	23.56	-0.33
			St.Dev.	17.72	1.55
		Delta (L - R)	Avg	-1.29	-0.12
			St.Dev.	6.32	1.33
Day 35	WB	Left	Avg	26.66	4.52
			St.Dev.	9.14	4.06
		Right	Avg	33.67	3.34
			St.Dev.	8.56	3.58
		Delta (L - R)	Avg	**-7.02**	1.19
			St.Dev.	3.47	1.21
	HS	Left	Avg	48.53	1.83
			St.Dev.	4.61	0.73
		Right	Avg	47.27	2.25
			St.Dev.	4.34	0.88
		Delta (L - R)	Avg	1.26	**-0.42**
			St.Dev.	3.99	0.35

Table 4.6. Specific flow cytometry data

Values in bold indicate significant difference between left and right tibiae (i.e. value for delta is significantly different from zero).

				Woven bone area (mm^2)	TRAP pos.pits/CorA #/mm^2	Percent perimeter covered (%) Periosteal	Endosteal
Day 14	WB	Left	Avg	0.00	0.65	1.06	0.73
			St.Dev.	0.00	0.51	2.61	0.96
		Right	Avg	0.00	0.52	0.74	1.72
			St.Dev.	0.00	0.23	1.24	1.92
		Delta (L - R)	Avg	0.00	0.12	0.32	-0.99
			St.Dev.	0.00	0.39	2.52	1.83
	HS	Left	Avg	0.00	0.66	0.10	0.26
			St.Dev.	0.00	0.56	0.17	0.68
		Right	Avg	0.00	0.62	0.22	0.10
			St.Dev.	0.00	0.56	0.53	0.26
		Delta (L - R)	Avg	0.00	0.03	-0.12	0.16
			St.Dev.	0.00	0.40	0.60	0.76
Day 18	WB	Left	Avg	0.26	0.68	0.35	0.55
			St.Dev.	0.08	0.42	0.58	0.73
		Right	Avg	0.00	0.38	0.00	6.70
			St.Dev.	0.00	0.16	0.00	7.76
		Delta (L - R)	Avg	**0.26**	**0.30**	0.35	-6.15
			St.Dev.	0.08	0.32	0.58	7.04
	HS	Left	Avg	0.04	0.26	0.11	0.15
			St.Dev.	0.03	0.10	0.29	0.41
		Right	Avg	0.00	0.06	0.00	0.00
			St.Dev.	0.00	0.10	0.00	0.00
		Delta (L - R)	Avg	**0.04**	**0.20**	0.11	0.15
			St.Dev.	0.03	0.16	0.29	0.41
Day 35	WB	Left	Avg	0.63	1.47	15.25	8.38
			St.Dev.	0.19	1.01	6.47	8.85
		Right	Avg	0.00	0.59	0.91	8.26
			St.Dev.	0.00	0.49	1.39	9.34
		Delta (L - R)	Avg	**0.63**	**0.88**	**14.34**	0.12
			St.Dev.	0.19	0.95	6.82	10.78
	HS	Left	Avg	0.16	0.32	7.84	0.75
			St.Dev.	0.15	0.15	11.56	1.33
		Right	Avg	0.00	0.37	0.46	1.11
			St.Dev.	0.00	0.30	1.00	1.53
		Delta (L - R)	Avg	**0.16**	-0.05	7.38	-0.36
			St.Dev.	0.15	0.25	11.45	2.17

Table 4.7. Specific TRAP and PSR data

Values in bold indicate significant difference between left and right tibiae (i.e. value for delta is significantly different from zero).

References

Aicher, A., M. Rentsch, et al. (2007). "Nonbone marrow-derived circulating progenitor cells contribute to postnatal neovascularization following tissue ischemia." Circ Res **100**(4): 581-9.

Ballas, M. T., J. Tytko, et al. (1997). "Common overuse running injuries: diagnosis and management." Am Fam Physician **55**(7): 2473-84.

Bentolila, V., T. M. Boyce, et al. (1998). "Intracortical remodeling in adult rat long bones after fatigue loading." Bone **23**(3): 275-81.

Bloomfield, S. A. (2006). "Does altered blood flow to bone in microgravity impact on mechanotransduction?" J Musculoskelet Neuronal Interact **6**(4): 324-6.

Bloomfield, S. A., M. R. Allen, et al. (2002). "Site- and compartment-specific changes in bone with hindlimb unloading in mature adult rats." Bone **31**(1): 149-57.

Burr, D. B., M. R. Forwood, et al. (1997). "Bone microdamage and skeletal fragility in osteoporotic and stress fractures." J Bone Miner Res **12**(1): 6-15.

Burr, D. B. and M. Hooser (1995). "Alterations to the en bloc basic fuchsin staining protocol for the demonstration of microdamage produced in vivo." Bone **17**(4): 431-3.

Burr, D. B. and R. B. Martin (1993). "Calculating the probability that microcracks initiate resorption spaces." J Biomech **26**(4-5): 613-6.

Burr, D. B., R. B. Martin, et al. (1985). "Bone remodeling in response to in vivo fatigue microdamage." J Biomech **18**(3): 189-200.

Caillot-Augusseau, A., L. Vico, et al. (2000). "Space flight is associated with rapid decreases of undercarboxylated osteocalcin and increases of markers of bone resorption without changes in their circadian variation: observations in two cosmonauts." Clin Chem **46**(8 Pt 1): 1136-43.

Cao, J. J., P. Kurimoto, et al. (2007). "Aging impairs IGF-I receptor activation and induces skeletal resistance to IGF-I." J Bone Miner Res **22**(8): 1271-9.

Cardoso, L., D. M. Laudier, et al. (2006). Inhibition of osteocyte apoptosis prevents activation of bone remodeling after fatigue in vivo. Orthopaedic Research Society, Chicago, IL.

Danova, N. A., S. A. Colopy, et al. (2003). "Degradation of bone structural properties by accumulation and coalescence of microcracks." Bone **33**(2): 197-205.

Eghbali-Fatourechi, G., S. Khosla, et al. (2003). "Role of RANK ligand in mediating increased bone resorption in early postmenopausal women." J Clin Invest **111**(8): 1221-30.

Filgueira, L. (2004). "Fluorescence-based staining for tartrate-resistant acidic phosphatase (TRAP) in osteoclasts combined with other fluorescent dyes and protocols." J Histochem Cytochem **52**(3): 411-4.

Frank, J. D., M. Ryan, et al. (2002). "Aging and accumulation of microdamage in canine bone." Bone **30**(1): 201-6.

Gavrieli, Y., Y. Sherman, et al. (1992). "Identification of programmed cell death in situ via specific labeling of nuclear DNA fragmentation." J Cell Biol **119**(3): 493-501.

Herman, B. C., D. Berman, et al. (2008). Activation of bone remodeling after fatigue: Differential response to linear microcracks and diffuse damage. Orthopaedic Research Society, San Francisco, CA.

Herman, B. C., L. Cardoso, et al. (2007). The importance of early apoptotoc events following microdamage in triggering fatigue induced bone remodeling. Orthopaedic Research Society, San Diego, CA.

Herman, B. C., B. Faria, et al. (2006). Significant differences in fatigue behavior and remodeling response exist between young adult and older adult rat bones. Orthopaedic Research Society, Chicago, IL.

Herman, B. C., D. M. Laudier, et al. (2007). Acute osteocyte response to fatigue microdamage: Production of HIF-1α and VEGF-A. Orthopaedic Research Society, San Diego, CA.

Hsieh, Y. F. and M. J. Silva (2002). "In vivo fatigue loading of the rat ulna induces both bone formation and resorption and leads to time-related changes in bone mechanical properties and density." J Orthop Res **20**(4): 764-71.

Inoue, M., H. Tanaka, et al. (2000). "Altered biochemical markers of bone turnover in humans during 120 days of bed rest." Bone **26**(3): 281-6.

Jilka, R. L., R. S. Weinstein, et al. (2007). "Quantifying osteoblast and osteocyte apoptosis: challenges and rewards." J Bone Miner Res **22**(10): 1492-501.

Kim, H., K. Iwasaki, et al. (2003). "Changes in bone turnover markers during 14-day 6 degrees head-down bed rest." J Bone Miner Metab **21**(5): 311-5.

Knobloch, K., L. Schreibmueller, et al. (2007). "Rapid rehabilitation programme following sacral stress fracture in a long-distance running female athlete." Arch Orthop Trauma Surg **127**(9): 809-13.

Knothe Tate, M. L., U. Knothe, et al. (1998). "Experimental elucidation of mechanical load-induced fluid flow and its potential role in bone metabolism and functional adaptation." Am J Med Sci **316**(3): 189-95.

Knothe Tate, M. L., P. Niederer, et al. (1998). "In vivo tracer transport through the lacunocanalicular system of rat bone in an environment devoid of mechanical loading." Bone **22**(2): 107-17.

Kogianni, G., V. Mann, et al. (2008). "Apoptotic bodies convey activity capable of initiating osteoclastogenesis and localized bone destruction." J Bone Miner Res **23**(6): 915-27.

Lee, T. C., T. L. Arthur, et al. (2000). "Sequential labelling of microdamage in bone using chelating agents." J Orthop Res **18**(2): 322-5.

Lee, T. C., S. Mohsin, et al. (2003). "Detecting microdamage in bone." J Anat **203**(2): 161-72.

Lee, T. C., F. J. O'Brien, et al. (2000). "The nature of fatigue damage in bone." Int J Fatigue **22**: 847-53.

Lee, T. C., A. Staines, et al. (2002). "Bone adaptation to load: microdamage as a stimulus for bone remodelling." J Anat **201**(6): 437-46.

Matsuzaki, H., G. R. Wohl, et al. (2007). "Damaging fatigue loading stimulates increases in periosteal vascularity at sites of bone formation in the rat ulna." Calcif Tissue Int **80**(6): 391-9.

Midura, R. J., X. Su, et al. (2006). "A simulated weightlessness state diminishes cortical bone healing responses." J Musculoskelet Neuronal Interact **6**(4): 327-8.

Morey-Holton, E. R. and R. K. Globus (1998). "Hindlimb unloading of growing rats: a model for predicting skeletal changes during space flight." Bone **22**(5 Suppl): 83S-88S.

Morey-Holton, E. R. and R. K. Globus (2002). "Hindlimb unloading rodent model: technical aspects." J Appl Physiol **92**(4): 1367-77.

Mori, S. and D. B. Burr (1993). "Increased intracortical remodeling following fatigue damage." Bone **14**(2): 103-9.

Muir, P., S. J. Sample, et al. (2007). "Effect of fatigue loading and associated matrix microdamage on bone blood flow and interstitial fluid flow." Bone **40**(4): 948-56.

O'Brien, F. J., D. Taylor, et al. (2002). "An improved labelling technique for monitoring microcrack growth in compact bone." J Biomech **35**(4): 523-6.

O'Brien, F. J., D. Taylor, et al. (2003). "Microcrack accumulation at different intervals during fatigue testing of compact bone." J Biomech **36**(7): 973-80.

Prisby, R. D., M. W. Ramsey, et al. (2007). "Aging reduces skeletal blood flow, endothelium-dependent vasodilation, and NO bioavailability in rats." J Bone Miner Res **22**(8): 1280-8.

Puchtler, H., S. N. Meloan, et al. (1988). "Are picro-dye reactions for collagens quantitative? Chemical and histochemical considerations." Histochemistry **88**(3-6): 243-56.

Sakata, T., B. P. Halloran, et al. (2003). "Skeletal unloading induces resistance to insulin-like growth factor I on bone formation." Bone **32**(6): 669-80.

Sakata, T., Y. Wang, et al. (2004). "Skeletal unloading induces resistance to insulin-like growth factor-I (IGF-I) by inhibiting activation of the IGF-I signaling pathways." J Bone Miner Res **19**(3): 436-46.

Silva, M. J. and D. C. Touhey (2007). "Bone formation after damaging in vivo fatigue loading results in recovery of whole-bone monotonic strength and increased fatigue life." J Orthop Res **25**(2): 252-61.

Silva, M. J., B. A. Uthgenannt, et al. (2006). "In vivo skeletal imaging of 18F-fluoride with positron emission tomography reveals damage- and time-dependent responses to fatigue loading in the rat ulna." Bone **39**(2): 229-36.

Stevens, H. Y., D. R. Meays, et al. (2006). "Pressure gradients and transport in the murine femur upon hindlimb suspension." Bone **39**(3): 565-72.

Stover, S. M., R. B. Martin, et al. (1993). In vivo labeling of microdamage in cortical bone tissue. Orthopaedic Research Society, San Francisco, CA.

Strange, R., R. R. Friis, et al. (1995). "Programmed cell death during mammary gland involution." Methods Cell Biol **46**: 355-68.

Sweat, F., H. Puchtler, et al. (1964). "Sirius Red F3ba As A Stain For Connective Tissue." Arch Pathol **78**: 69-72.

Tami, A. E., P. Nasser, et al. (2003). "Noninvasive fatigue fracture model of the rat ulna." J Orthop Res **21**(6): 1018-24.

Tami, A. E., P. Nasser, et al. (2002). "The role of interstitial fluid flow in the remodeling response to fatigue loading." J Bone Miner Res **17**(11): 2030-7.

Tan, S. D., T. J. de Vries, et al. (2007). "Osteocytes subjected to fluid flow inhibit osteoclast formation and bone resorption." Bone **41**(5): 745-51.

Turner, C. H., M. P. Akhter, et al. (1991). "A noninvasive, in vivo model for studying strain adaptive bone modeling." Bone **12**(2): 73-9.

Uthgenannt, B. A., M. H. Kramer, et al. (2007). "Skeletal self-repair: stress fracture healing by rapid formation and densification of woven bone." J Bone Miner Res **22**(10): 1548-56.

Verborgt, O., G. J. Gibson, et al. (2000). "Loss of osteocyte integrity in association with microdamage and bone remodeling after fatigue in vivo." J Bone Miner Res **15**(1): 60-7.

Verborgt, O., N. A. Tatton, et al. (2002). "Spatial distribution of Bax and Bcl-2 in osteocytes after bone fatigue: complementary roles in bone remodeling regulation?" J Bone Miner Res **17**(5): 907-14.

Vico, L., P. Collet, et al. (2000). "Effects of long-term microgravity exposure on cancellous and cortical weight-bearing bones of cosmonauts." Lancet **355**(9215): 1607-11.

Waldorff, E. I., S. A. Goldstein, et al. (2007). "Age-dependent microdamage removal following mechanically induced microdamage in trabecular bone in vivo." Bone **40**(2): 425-32.

Wronski, T. J. and E. R. Morey-Holton (1987). "Skeletal response to simulated weightlessness: a comparison of suspension techniques." Aviat Space Environ Med **58**(1): 63-8.

You, L., S. Temiyasathit, et al. (2008). "Osteocytes as mechanosensors in the inhibition of bone resorption due to mechanical loading." Bone **42**(1): 172-9.

CHAPTER 5

DAILY SHORT-TERM WEIGHTBEARING DURING DISUSE RESCUES THE MICRODAMAGE REPAIR AND REMODELING RESPONSE

Summary

Prior work (chapter 4) demonstrates that bone remodeling in response to fatigue microdamage is absent during disuse. The purpose of this study was to examine the effects of daily short-term weight bearing during disuse on targeted remodeling.

At day 0, 40 male 6-month old Sprague Dawley rats were assigned to hindlimb suspension with daily weight bearing following damage inducing loading (HW). The rats were divided into two subgroups (n=20), corresponding to two sacrifice time points (day 18 or 35). At day 14, animals were anesthetized and their left tibia underwent cyclic four-point bending in order to produce fatigue-induced microdamage. At sacrifice, right/left pairs of tibiae were assigned to one of three treatments within each subgroup: flow cytometry for HSC and monocyte markers (n=6), basic fuchsin staining for microdamage assessment (n=7), or histological/immunohistochemical staining (Picr-Sirius Red, ELF97 (TRAP), Apoptag) (n=7). Prior to staining, morphologic analysis was conducted on the last two groups using 3D microCT.

Morphologic examinations revealed that the damage induced a stress fracture response resulting in a significant increase in woven bone apposition. At day 35, the HW group had a significant decrease in microdamage, corresponding to that seen with normal

weight bearing (WB) animals (chapter 4). The HW group had similar amounts of apoptotic osteocytes as WB or purely hindlimb suspended (HS) animals. Flow cytometry indicated that a shift in the osteoclast lineage had occurred due to a decrease of monocytes in the damaged leg for the HW group, which was similar to the WB group (chapter 4). ELF97 staining supported this evidence, showing a significant increase in TRAP positive resorption pits for day 18 and 35 for the HW group.

This study demonstrates that intermittent daily physiological loading can reverse the lack of remodeling in response to microdamage present during disuse. Although intermittent loading cannot rescue the reduction in woven bone production following microdamage, the targeted resorption of microdamage is restored. Furthermore, this study cements the results presented in chapter 4, that the mechanisms by which targeted remodeling is 'sensed' are indeed very dependent on the stimulus associated with mechanical usage.

Introduction

In chapter 4, we demonstrated that physiological loading is necessary for the remodeling repair response to occur following significant accumulation of microdamage, since disuse alters the microdamage response through a reduction in woven bone production and the lack of resorption of microdamage. The lack of osteoclast activation was hypothesized to be due a decrease in interstitial fluid flow, which has been observed during disuse (Stevens, Meays et al. 2006). In addition, several studies suggest that load-induced fluid flow may be necessary to provide sufficient transport of larger molecules such as proteins to and from osteocytes (Knothe Tate, Knothe et al. 1998; Knothe Tate,

Niederer et al. 1998). As mentioned in chapter 3, there is evidence that osteocyte apoptotic bodies initiate osteoclastogenesis leading to localized bone resorption (Kogianni, Mann et al. 2008) suggesting that during hindlimb suspension or disuse the 'active' signal for resorption of microdamage is inhibited due to the lack of fluid flow through the canalicular system, thus preventing delivery of resorption initiating signals from the apoptotic osteocytes.

Previous studies have shown that supine weight-bearing exercise within a lower body negative chamber (LBNP) counteracts bone loss associated with long-term bed rest (Smith, Davis-Street et al. 2003; Zwart, Hargens et al. 2007). However daily standing for one or two hours per day during 28 days of hindlimb suspension does not alter the deterioration of cortical bone due to hindlimb suspension (Zhang, Sun et al. 2003). Early clinical evidence for recovery of bone repair in a disuse setting with moderate physiologic loading comes from the treatment of running related stress fractures. Previous treatment methods for stress fractures associated with long distance running prescribed up to 12 weeks of therapy (dominantly non-weight-bearing) before returning to a normal running schedule (Ballas, Tytko et al. 1997). However a recent study (without an experimental basis) decreased the recovery period by implementing earlier cross-training and enabled the athlete to return to function in only seven weeks (Knobloch, Schreibmueller et al. 2007). This early clinical study parallels the results presented in chapter 4 indicating that the removal of load (i.e. the casting/disuse) indeed causes an impaired repair process.

It was therefore hypothesized that moderate physiological loading could potentially rescue the impaired microdamage repair that was presented in chapter 4. By

allowing intermittent perfusion of the already reduced fluid flow within the canalicular system in a disuse setting, the apoptotic distress signal from osteocytes surrounding microcracks could potentially reach their cytokine receptors and thereby induce targeted remodeling. Hence moderate exercise could potentially prove adequate for inducing the necessary repair process.

The purpose of this study was therefore to examine the effects of daily one hour weight bearing during disuse on bone remodeling in response to microdamage, potentially providing support to early clinical evidence that moderate loading can reduce recovery time from stress fractures.

Materials and Methods

Animals

Male 6-month old adult Sprague Dawley rats (350-450g) were obtained from Harlan. Animals were allowed to acclimate to our animal facility for at least three days before being included in the experiment. The procedures used in this study were approved by the University Committee on Use and Care of Animals at the University of Michigan. Animals were housed in individual non-ventilated cages in a temperature-controlled room (68-72˚F) with a 12:12-hour light-dark cycle. Water and rat chow were provided ad libitum.

Experimental protocol

After acclimation (day 0), 40 rats were assigned to hindlimb suspension with daily weight bearing following damage inducing loading (HW). The rats were divided

into two subgroups (n=20), corresponding to two sacrifice time points (day 18 or 35). At day 0 all animals were briefly anesthetized with an isoflurane (2%):oxygen balance, and hindlimb suspended using a custom made hindlimb suspension system (see chapters 3 and 4) for 14 days. Normal weight bearing (WB) and hindlimb suspended w/o daily weight bearing (HS) animals from a previous experiment (see chapter 4) served as positive and negative controls, respectively. At day 14, all animals were anesthetized and their left tibia underwent four-point bending in order to produce fatigue-induced microdamage using the same load protocol presented in chapter 4. The right tibia served as a non-loaded, completely undamaged control. Once the loading regime was complete, animals were allowed full recovery from anesthesia, and subsequently hindlimb suspended again. Starting at day 15, animals were unhooked from the tail suspension mechanism in their cages and allowed one hour of full weight bearing within their respective cages each day, after which they were returned to hindlimb suspension.

At sacrifice, right/left pairs of tibiae were carefully dissected free of soft tissue and assigned to one of three treatments within each subgroup: Flow cytometry for HSC and monocyte markers (n=6), basic fuchsin staining for microdamage assessment (n=7), or regular histological and immunohistochemical staining (n=7). Prior to staining, morphologic analysis was conducted on the last two groups using 3D microCT.

The protocols for microcomputed tomography (microCT), flow cytometry (FACS), basic fuchsin staining, histology (ELF97 (TRAP), Picro-Sirius Red) and immunohistochemistry (Apoptag apoptosis detection) were performed similarly as explained in chapter 4. The region of interest (ROI) was identical to the ROI presented in

chapter 4, with a length of 4 mm with its center located 8 mm proximal to the tibia/fibula junction.

Statistics and graph nomenclature

To compare damaged to undamaged contralateral sides, paired t-tests were used. A two-way ANOVA with a post hoc correction was used for comparisons between experimental groups (HW/WB/HS) and between groups at different time points. Significance was defined as $p \leq 0.05$. The analysis was performed using SPSS statistical software (SPSS, Chicago, IL).

For ease of comparison between different time points, the term Delta is used to indicate differences between contra-lateral limbs:

Delta = Left tibia – Right tibia = Damaged tibia – Undamaged tibia

This term will be used throughout the presentation of the results.

Results

Animal health

The starting body mass at day 0 was not significantly different between the HW, WB and HS groups (Table 5.1). By day 14, animals in the HW group had lost 2.9% weight (Figure 5.1), which was not significantly different than the 4.2% weight loss for the HS group. Common for all three groups was a slight decline in weight (day 18) after loading at day 14, followed by a slight incline in body weight at day 35. Both incline and decline for all groups were non-significant, and not significantly different between the HW and HS groups (Figure 5.1).

Microcomputed tomography (microCT)

MicroCT analysis showed a trend of an increase in delta tissue mineral content (TMC) at day 35 for the HW group, which was similar to the HS group, but significantly smaller than for the WB group (Figure 5.2). The delta cortical area was significantly increased at day 35 for the HW group, which was similar to the WB and HS groups, but with a slight increase compared to the HS group (Figure 5.3). Finally, the delta marrow area was significantly increased at day 35 for the HW group, which was similar to the HS group. This change at day 35 was significantly different than the WB group (Figure 5.4). For a complete listing of the specific microCT data for the HW group, please refer to Table 5.2. See chapter 4 for specific data on the WB and HS groups.

Picro-Sirius Red stain (woven bone formation)

Sections stained with Picro-Sirius Red indicated that significant initial woven bone formation had occurred at day 18 for the HW group. This was significantly less than the WB group, but more than the HS group. At day 35 this had increased slightly for the HW group, which was similar to the HS group, but with the WB group having significantly more woven bone deposited than both the HS and HW group (Figure 5.5).

Basic fuchsin stain (microdamage quantification)

Sections stained with basic fuchsin for microdamage quantification showed that similar significant amounts of microdamage remained at day 18 for the WB, HS and HW groups (Figure 5.6). The crack surface density was also similar between the three groups at day 18 (Figure 5.7). The HW group showed a significant decrease in microdamage

from day 18 to day 35, which was similar to what was observed for the WB group, while damage remained the same for the HS group over the three time points (Figure 5.6). A similar significant trend was observed for the HW group for the crack surface density from day 18 to day 35 (Figure 5.7). For a complete listing of the specific basic fuchsin data for the HW group, please refer to Table 5.3. See chapter 4 for specific data on the WB and HS groups.

Osteocyte apoptosis

Apoptag osteocyte apoptosis detection revealed that the damage induced by fatigue loading at day 14 resulted in significant amounts of cortical apoptotic osteocytes at day 18 and 35 for the HW group (Figure 5.8). The number of apoptotic osteocytes decreased significantly from day 18 to day 35 for the HW group. The results were similar to the data for the WB and HS groups at day 18 and 35 (Figure 5.8). For a complete listing of the specific osteocyte apoptosis detection data for the HW group, please refer to Table 5.4. See chapter 4 for specific data on the WB and HS groups.

Flow cytometry

FACS showed that delta CD11b was significantly decreased at day 18 for the HW group (Figure 5.9). At day 35 the decrease only follows a strong trend ($p=0.07$), but is significantly lower than the HS group. This is similar to the difference between the WB and HS group at day 35 (Figure 5.9). The results for delta CD117 showed no significant difference from zero for the HW group at any time points, in addition to not being significantly different than the WB or HS group at either day 18 or day 35 (Figure 5.10).

For a complete listing of the specific flow cytometry data for the HW group, please refer to Table 5.5. See chapter 4 for specific data on the WB and HS groups.

ELF97 (TRAP staining)

TRAP staining using ELF97 phosphate showed a significant increase in delta TRAP positive intra cortical resorption pits for day 18 and day 35 for the HW group (Figure 5.11). The HW group increased significantly from day 18 to day 35, showing a similar trend as the WB group. In addition, the HW and HS groups were significantly different at day 35 (Figure 5.11). Delta percent TRAP positive periosteal perimeter showed a significant increase from day 18 to day 35 (Figure 5.12), while delta percent TRAP positive endosteal perimeter showed no difference between day 18 and 35 for the HW group (Figure 5.13). For a complete listing of the ELF 97 TRAP and Picro-Sirius Red data for the HW group, please refer to Table 5.6. See chapter 4 for specific data on the WB and HS groups.

Discussion

Although the HW group lost a significant amount of body weight over the first 14 days during assimilation, this was similar to the HS group. In addition, the maintenance of body weight from day 14, through day 18 and day 35 for all three groups indicated that general animal health was maintained over the course of the experiment.

Similar to WB and HS groups morphologic and histological examinations from microCT and Picro-Sirius Red staining revealed that the damage induced a stress fracture response, which at day 18 and 35 resulted in a significant increase in woven bone

apposition for the HW group. This response was similar in magnitude to the HS group at both day 18 and 35 with respect to woven bone apposition, although the microCT results indicated that HW had a slightly larger delta cortical area than HS at day 35. The marrow area was similar between HW and HS, but still significantly larger than for the WB group. This would indicate that general resorption continues at the endosteal perimeter for the HW and HS groups, or that significant woven bone apposition occurs at the endosteal surface for the WB group. However since the Picro-Sirius Red examinations did not reveal significant woven bone deposition at the endosteal surface, the former explanation seems to be more plausible.

Unlike the hindlimb suspended animals, the HW group had a significant reduction in remaining damage from day 14 and 18. This would indicate that unlike the HS group, osteoclasts must have been activated to remove the remaining damage. Since the woven bone deposition was still less than the WB group at day 35, this would suggest that although the mechanism targeting the local resorption of microcracks seems to have been activated for the HW group, the protective mechanism that the formation of woven bone provides is no longer present. This implies that whole bone strength remains low in a disuse setting following fatigue damage despite the daily physiological loading. One reason for this could be the significant reduction of blood flow in HS models (Bloomfield 2006), since there is a correlation between increased fatigue loading, increased vascularity and increased woven bone formation (Silva, Uthgenannt et al. 2006). However it has also been shown that one hour of daily loading for hindlimb suspended animals seems to prevent adverse changes in myocardial contractility and therefore blood flow (Zhang, Sun et al. 2003). Hence the significantly smaller woven bone response for

the HW and HS group seem most likely to be stemming from the reduction in osteoblast responsiveness and bone formation rate associated with hindlimb suspension (Bloomfield, Allen et al. 2002; Cao, Kurimoto et al. 2007).

The intra-cortical resorption response, which has been seen in several studies (Burr, Martin et al. 1985; Burr and Martin 1993; Mori and Burr 1993; Bentolila, Boyce et al. 1998; Verborgt, Gibson et al. 2000; Lee, Staines et al. 2002), is evident for both the WB and HW group following fatigue damage. The immunohistochemical results indicate that there is a similar decay of apoptotic osteocytes from day 14 to day 18 and 35, assuming that the initial apoptosis is similar at day 14 for the HS and HW group. It has been shown that similar amounts of microdamage have been induced for all three groups, resulting in similar amounts of osteocyte apoptosis. Hence the increase in intra-cortical resorption pits and significant microdamage removal for the HW group suggest that the lack of osteoclast recruitment for the HS group was recovered with daily moderate loading.

The examination of the HSC and monocyte population of the osteoclast lineage with flow cytometry for the HW group revealed a significant decrease in monocytes at day 18, with a continued strong decreasing trend at day 35, where the HW group was significantly lower than the HS group, but similar to the WB group. The increase in HSC population at day 35 for the WB group was not mirrored for the HW group, which was not significantly different than the WB and HS groups at any time point. Although the HSC results were inconclusive, the monocyte results indicate that, as with the WB group, a shift in the osteoclast lineage has occurred following induction of microdamage. Hence

the flow cytometry results in conjunction with the TRAP staining suggest that targeted osteoclast activation and recruitment has indeed been recovered with daily loading.

As discussed in chapter 4, there is evidence that interstitial fluid flow decreases during disuse (Stevens, Meays et al. 2006), and that cell-to-cell communications via gap junctions between osteocyte-like MLO-Y4 cells decrease significantly in multi-dimensional gravity (Matsuda, Kurata et al. 2006). However, in parallel with the idea that load-induced fluid flow may be necessary to provide sufficient transport of larger molecules such as proteins to and from osteocytes (Knothe Tate, Knothe et al. 1998; Knothe Tate, Niederer et al. 1998), the results for the HW group seem to indicate that intermittent loading during disuse can provide enough interstitial fluid flow to distribute any 'active' signal of resorption.

This study demonstrates that intermittent daily physiological loading can reverse the lack of remodeling in response to microdamage present during disuse. Although intermittent loading cannot rescue the reduction in woven bone production following microdamage, the targeted resorption of microdamage is revived. The data suggest that the early clinical evidence (without an experimental basis) of a decreased recovery time from a running-related stress fracture with early moderate exercise (Knobloch, Schreibmueller et al. 2007) is due to the increase in targeted remodeling. Future larger scale clinical studies should therefore be done to test the effect of changing the current treatment of stress fractures from prevention of load-bearing to a moderate exercise treatment.

Finally, this study cements the results presented in chapter 4, that the mechanism by which targeted remodeling is 'sensed' is indeed dependent on the stimulus associated with mechanical usage.

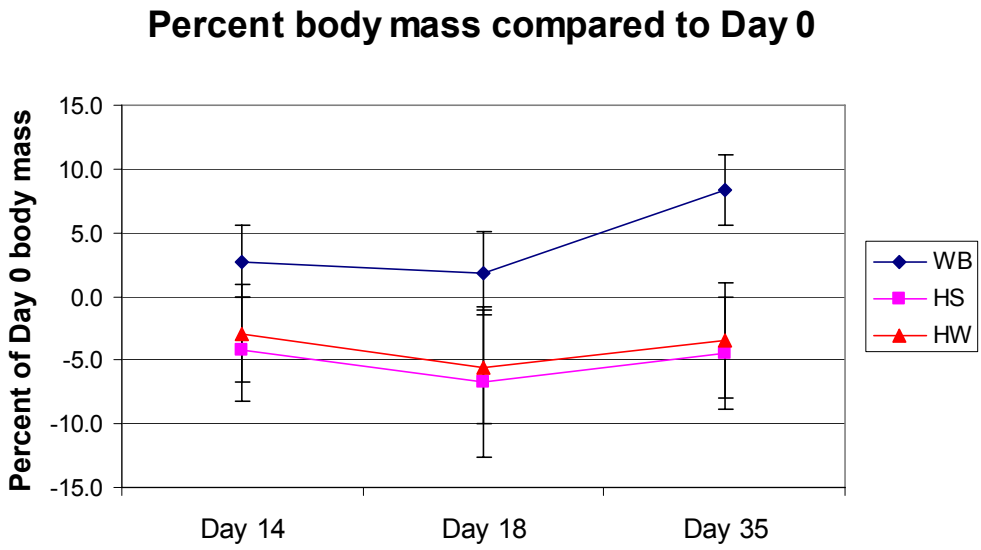

Figure 5.1. Percent body mass compared to day 0

Error bars indicate standard deviations.

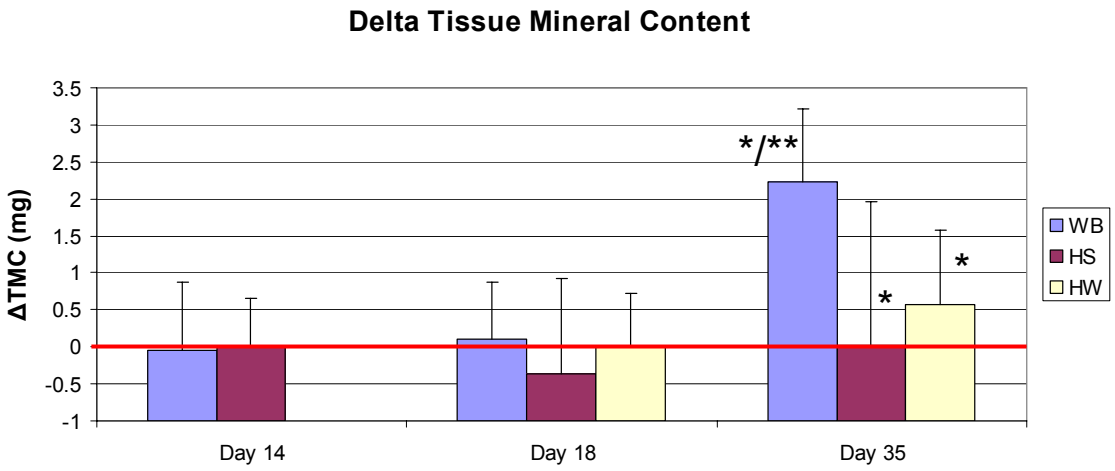

Figure 5.2. Delta tissue mineral content

Single asterisk (*), indicate significant difference between WB vs. group at that day. Double asterisks (**), indicate significant difference between R vs. L leg for that group on the particular day (i.e. delta is significantly different from zero). Error bars indicate standard deviations.

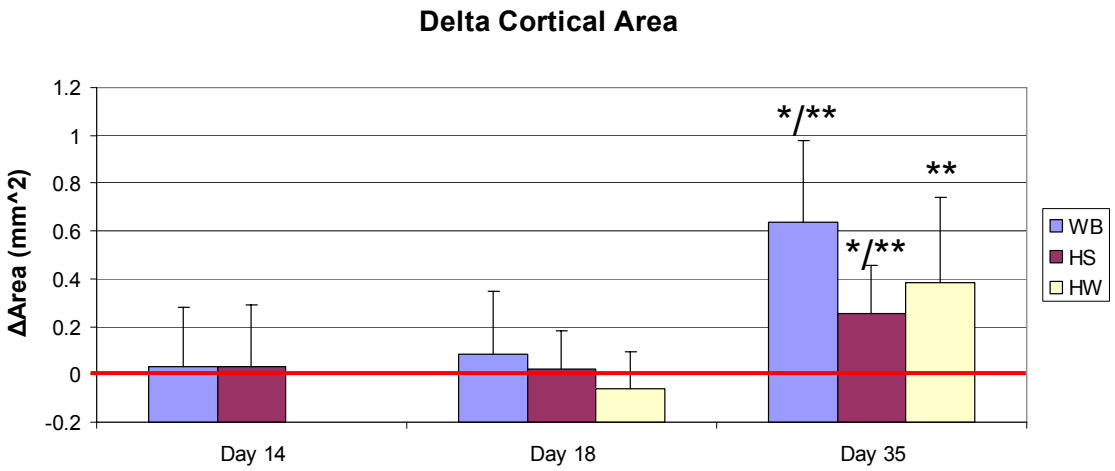

Figure 5.3. Delta cortical area

Single asterisk (*), indicate significant difference between WB vs. group at that day. Double asterisks (**), indicate significant difference between R vs. L leg for that group on the particular day (i.e. delta is significantly different from zero). Error bars indicate standard deviations.

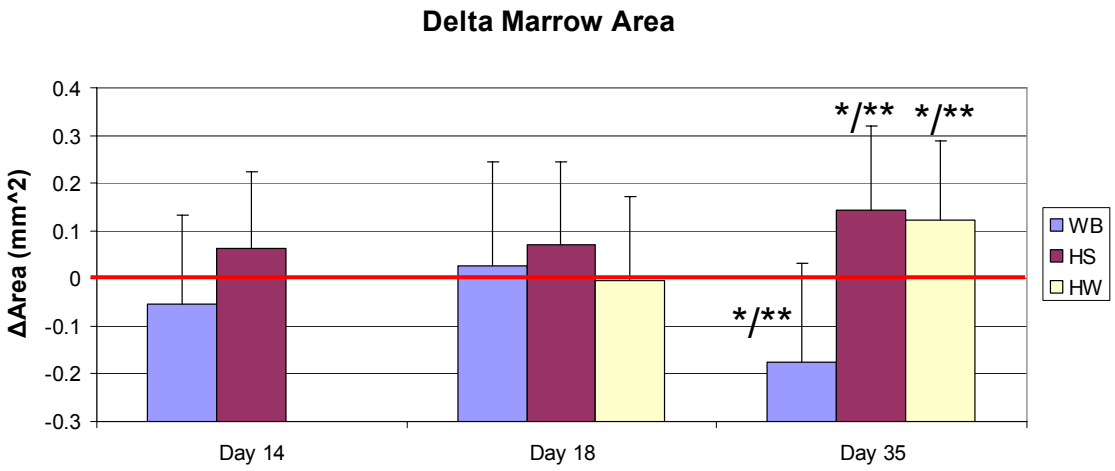

Figure 5.4. Delta marrow area

Single asterisk (*), indicate significant difference between WB vs. group at that day. Double asterisks (**), indicate significant difference between R vs. L leg for that group on the particular day (i.e. delta is significantly different from zero). Error bars indicate standard deviations.

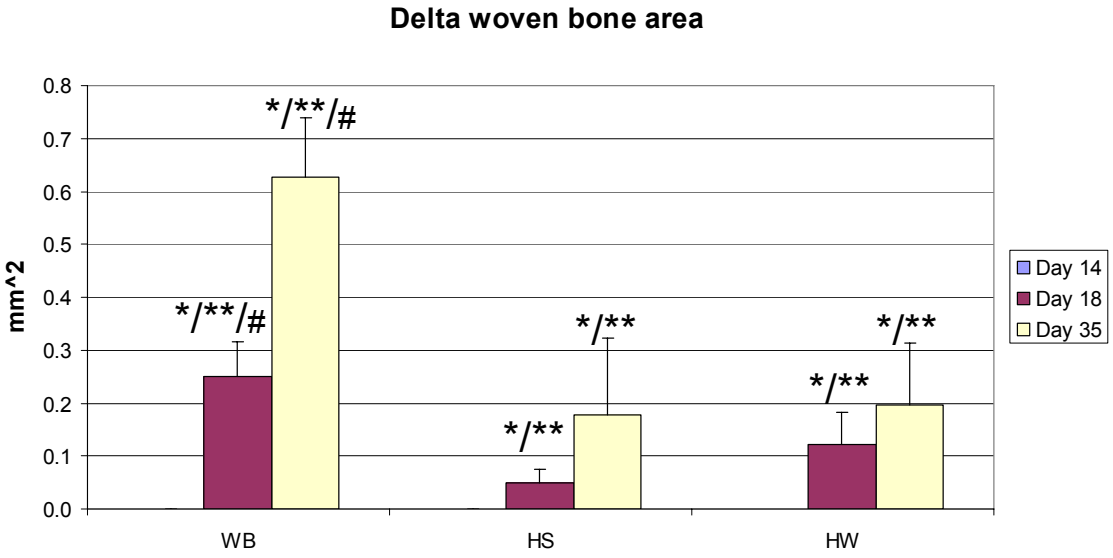

Figure 5.5. Delta woven bone area

Single asterisk (*), indicate significant difference between WB vs. group at that day. Double asterisks (**), indicate significant difference between R vs. L leg for that group on the particular day (i.e. delta is significantly different from zero). Single pound (#), indicate significant difference between day 18 and 35 within the specific group (WB, HS or HW). Error bars indicate standard deviations.

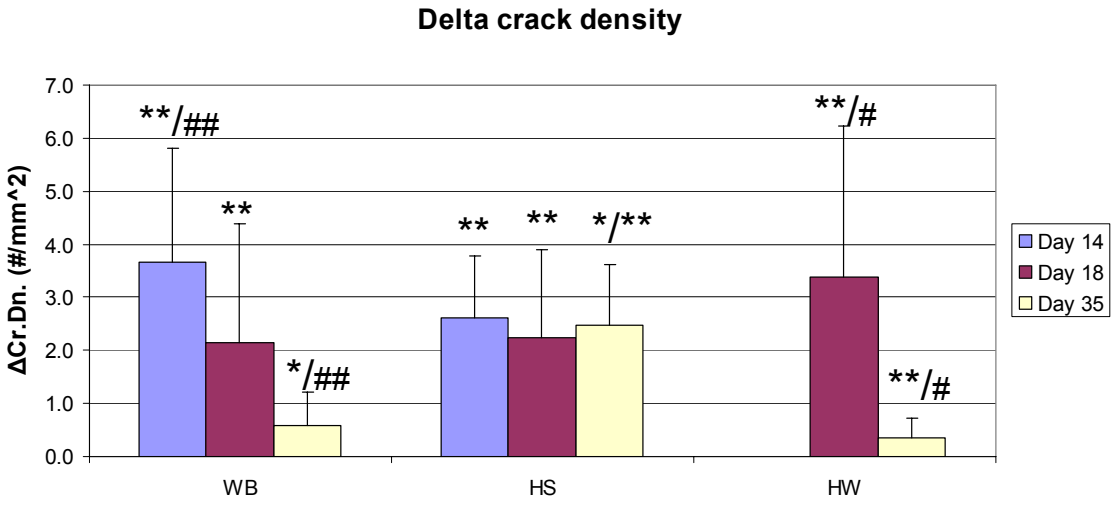

Figure 5.6. Delta crack density

Delta crack density was determined while omitting woven bone areas.

Single asterisk (*), indicate significant difference between WB vs. group at that day. Double asterisks (**), indicate significant difference between R vs. L leg for that group on the particular day (i.e. delta is significantly different from zero). Single pound (#), indicate significant difference between day 18 and 35 within the specific group (WB, HS or HW). Double pound (##), indicate significant difference between day 14 and 35 within the specific group (WB, HS or HW). Error bars indicate standard deviations.

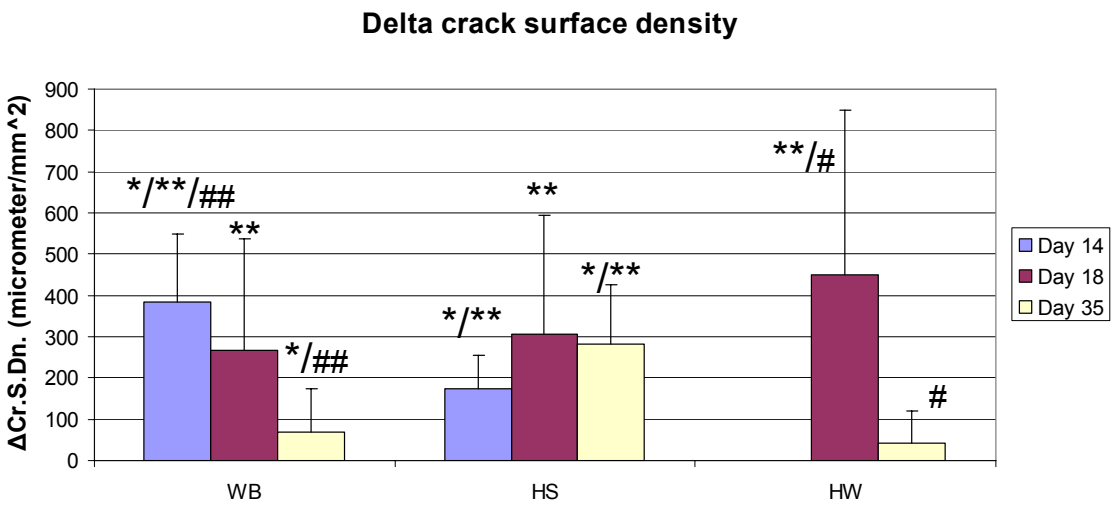

Figure 5.7. Delta crack surface density

Delta crack surface density was determined while omitting woven bone areas.

Single asterisk (*), indicate significant difference between WB vs. group at that day. Double asterisks (**), indicate significant difference between R vs. L leg for that group on the particular day (i.e. delta is significantly different from zero). Single pound (#), indicate significant difference between day 18 and 35 within the specific group (WB, HS or HW). Double pound (##), indicate significant difference between day 14 and 35 within the specific group (WB, HS or HW). Error bars indicate standard deviations.

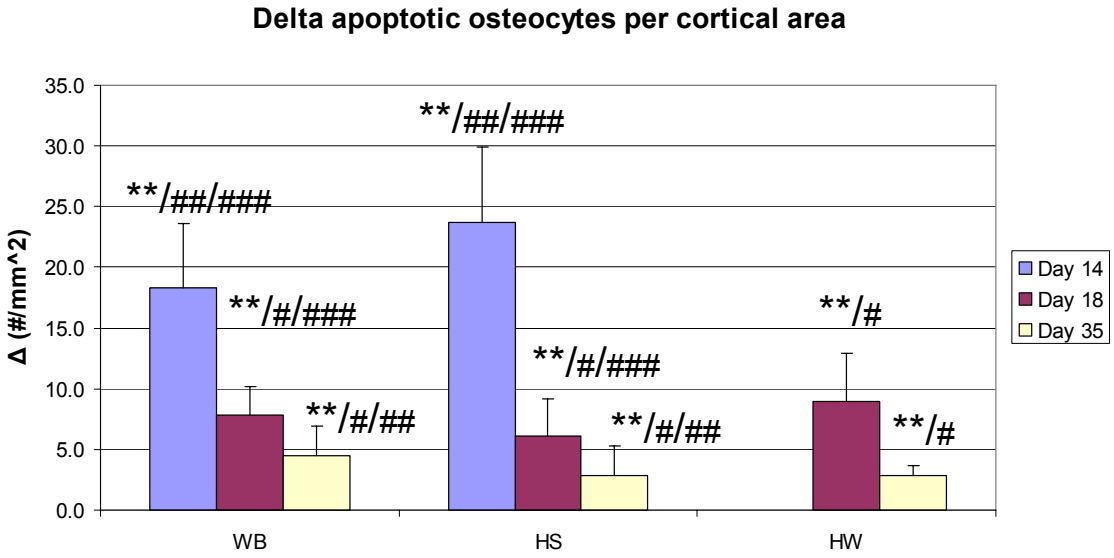

Figure 5.8. Delta apoptotic osteocytes per cortical area

Number of apoptotic osteocytes (per cortical area) was determined while omitting woven bone areas.

Single asterisk (*), indicate significant difference between WB vs. group at that day. Double asterisks (**), indicate significant difference between R vs. L leg for that group on the particular day (i.e. delta is significantly different from zero). Single pound (#), indicate significant difference between day 18 and 35 within the specific group (WB, HS or HW). Double pound (##), indicate significant difference between day 14 and 35 within the specific group (WB, HS or HW). Triple pound (###), indicate significant difference between day 14 and 18 within the specific group (WB, HS or HW). Error bars indicate standard deviations.

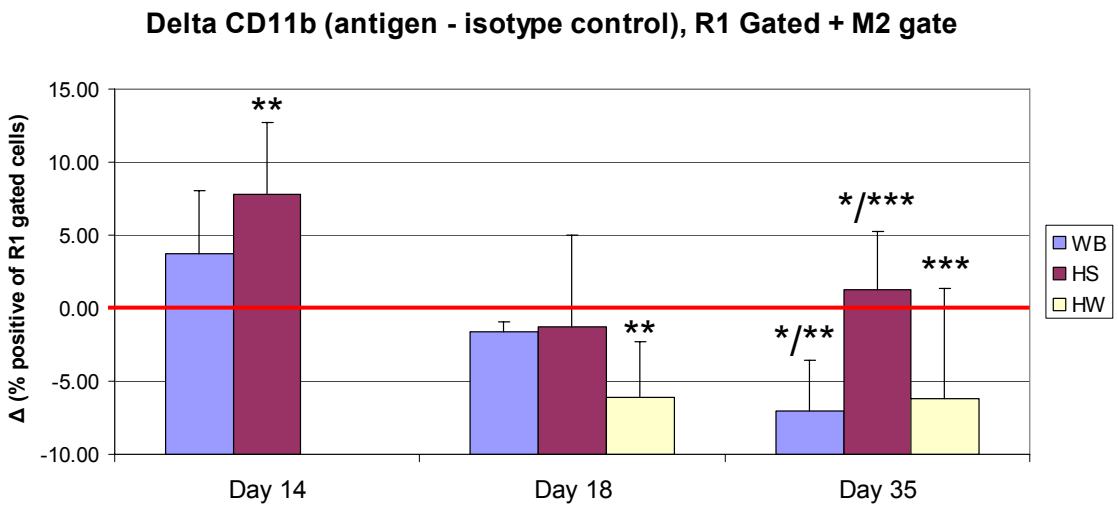

Figure 5.9. Delta CD11b

Single asterisk (*), indicate significant difference between WB vs. group at that day. Double asterisks (**), indicate significant difference between R vs. L leg for that group on the particular day (i.e. delta is significantly different from zero). Triple asterisk (***), indicate significant difference between HW vs. group at that day. Error bars indicate standard deviations.

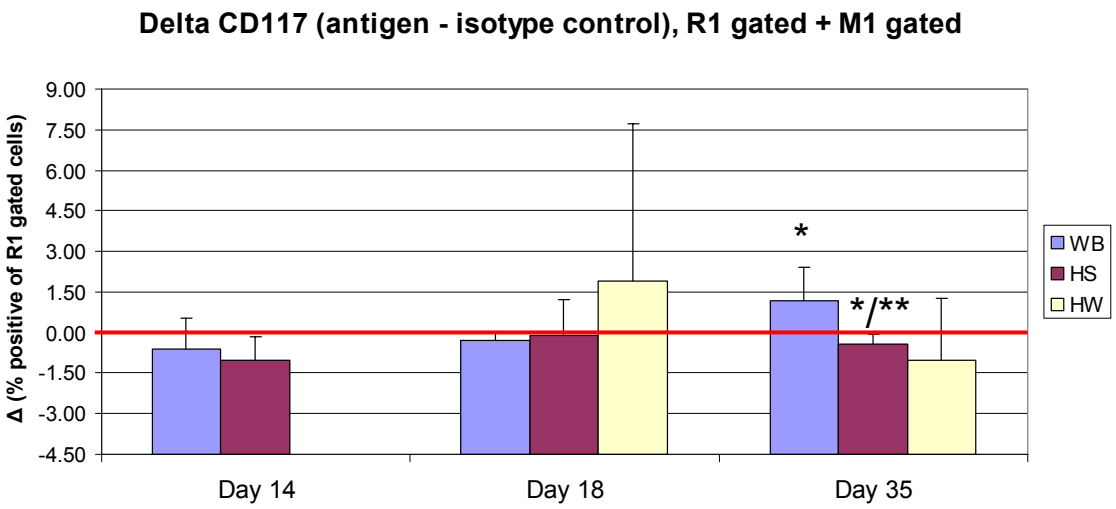

Figure 5.10. Delta CD117

Single asterisk (*), indicate significant difference between WB vs. group at that day. Double asterisks (**), indicate significant difference between R vs. L leg for that group on the particular day (i.e. delta is significantly different from zero). Triple asterisk (***), indicate significant difference between HW vs. group at that day. Error bars indicate standard deviations.

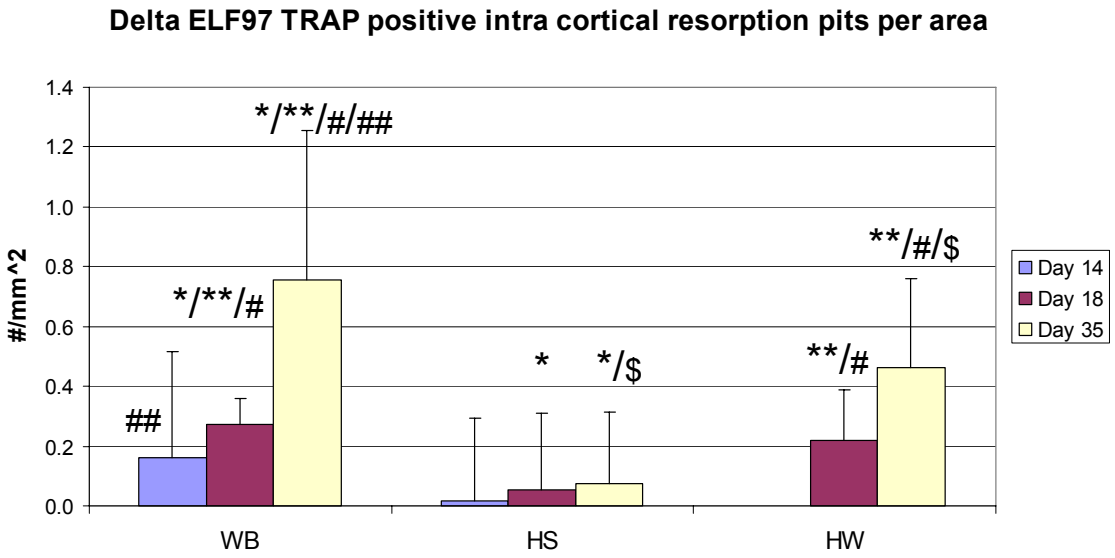

Figure 5.11. Delta TRAP positive resorption pits

Number of TRAP positive intra cortical resorption pits (per cortical area) was determined while omitting woven bone areas.

Single asterisk (*), indicate significant difference between WB vs. group at that day. Double asterisks (**), indicate significant difference between R vs. L leg for that group on the particular day (i.e. delta is significantly different from zero). Single pound (#), indicate significant difference between day 18 and 35 within the specific group (WB, HS or HW). Double pound (##), indicate significant difference between day 14 and 35 within the specific group (WB, HS or HW). Single dollar sign ($), indicate significant difference between HS vs. HW at that day. Error bars indicate standard deviations.

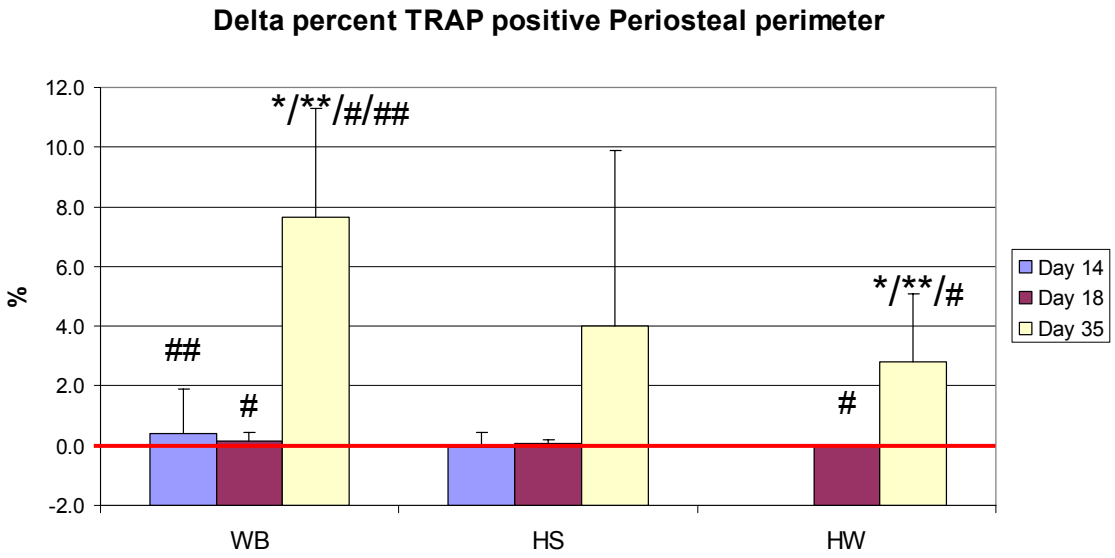

Figure 5.12. Delta percent TRAP positive periosteal perimeter

Percent TRAP positive periosteal perimeter was done using the outer most surface available (i.e. including any woven bone apposition).

Single asterisk (*), indicate significant difference between WB vs. group at that day. Double asterisks (**), indicate significant difference between R vs. L leg for that group on the particular day (i.e. delta is significantly different from zero). Single pound (#), indicate significant difference between day 18 and 35 within the specific group (WB or HS). Double pound (##), indicate significant difference between day 14 and 35 within the specific group (WB or HS). Triple pound (###), indicate significant difference between day 14 and 18 within the specific group (WB or HS). Error bars indicate standard deviations.

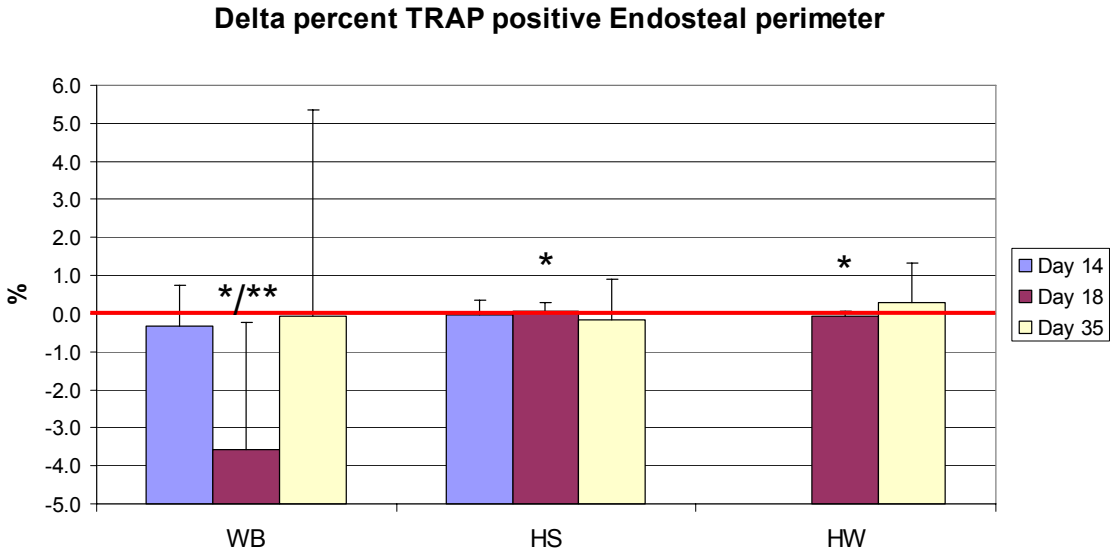

Figure 5.13. Delta percent TRAP positive endosteal perimeter

Percent TRAP positive endosteal perimeter was done using the outer most surface available (i.e. including any woven bone apposition).

Single asterisk (*), indicate significant difference between WB vs. group at that day. Double asterisks (**), indicate significant difference between R vs. L leg for that group on the particular day (i.e. delta is significantly different from zero). Single pound (#), indicate significant difference between day 18 and 35 within the specific group (WB or HS). Double pound (##), indicate significant difference between day 14 and 35 within the specific group (WB or HS). Triple pound (###), indicate significant difference between day 14 and 18 within the specific group (WB or HS). Error bars indicate standard deviations.

	WB	HS	HW
Avg. (g)	435.6	426.4	430.5
St.Dev.	33.5	31.5	18.7

Table 5.1. Starting body mass at day 0

				TMC (mg)	TMD (mg/cc)	Ixx (mm^4)	Iyy (mm^4)	Izz (mm^4)	Marrow Area (mm^2)	Cortical Area (mm^2)
Day 18	HW	Left	Avg	18.35	879.94	5.68	3.67	9.35	2.63	4.88
			St.Dev.	0.58	15.22	0.51	0.30	0.76	0.35	0.28
		Right	Avg	18.35	872.86	5.75	3.75	9.50	2.63	4.93
			St.Dev.	0.83	9.54	0.62	0.42	0.99	0.37	0.35
		Delta (L - R)	Avg	0.00	7.07	-0.07	-0.08	-0.15	0.00	-0.06
			St.Dev.	0.72	15.40	0.47	0.28	0.62	0.17	0.15
Day 35	HW	Left	Avg	18.94	862.95	5.85	4.08	9.93	2.54	5.00
			St.Dev.	1.03	11.09	0.84	0.44	1.23	0.34	0.41
		Right	Avg	18.36	865.89	5.52	3.76	9.28	2.42	4.62
			St.Dev.	1.22	8.51	0.73	0.38	1.05	0.30	0.31
		Delta (L - R)	Avg	0.58	-2.94	0.33	**0.31**	**0.64**	**0.12**	**0.38**
			St.Dev.	1.00	12.83	0.68	0.33	0.92	0.16	0.36

Table 5.2. Specific microCT data for ROI

Values in bold indicate significant difference between left and right tibiae (i.e. value for delta is significantly different from zero).

				Cortical area (mm^2)	Cr.Dn. (cracks/mm^2)	Cr.S.Dn. (μm/mm^2)
Day 18	HW	Left	Avg	5.43	4.03	551.32
			St.Dev.	0.25	3.10	455.62
		Right	Avg	5.28	0.65	102.29
			St.Dev.	0.32	0.74	116.06
		Delta (L - R)	Avg	0.14	**3.38**	**449.03**
			St.Dev.	0.26	2.86	401.34
Day 35	HW	Left	Avg	5.53	0.78	104.04
			St.Dev.	0.33	0.14	43.42
		Right	Avg	5.25	0.42	60.84
			St.Dev.	0.32	0.37	66.74
		Delta (L - R)	Avg	0.27	**0.36**	43.21
			St.Dev.	0.41	0.36	76.29

Table 5.3. Specific basic fuchsin data

Values in bold indicate significant difference between left and right tibiae (i.e. value for delta is significantly different from zero).

				# of apoptotic cortical osteocytes				Apop.osteo.per area
				Lateral	Medial	Posterior	**Total**	**#/(mm^2)**
Day 18	HW	Left	Avg	28.8	19.2	7.8	55.8	11.4
			St.Dev.	22.0	5.3	2.8	20.7	4.1
		Right	Avg	3.3	6.3	3.0	12.7	2.4
			St.Dev.	1.4	2.0	2.1	3.7	0.7
		Delta (L - R)	Avg	25.5	12.8	4.8	43.2	**8.9**
			St.Dev.	22.8	5.9	3.9	20.1	4.0
Day 35	HW	Left	Avg	10.8	12.0	5.5	28.3	5.5
			St.Dev.	7.4	7.9	3.0	5.3	0.9
		Right	Avg	5.2	6.2	2.2	13.5	2.6
			St.Dev.	1.7	2.6	1.7	3.6	0.6
		Delta (L - R)	Avg	5.7	5.8	3.3	14.8	**2.9**
			St.Dev.	7.8	7.1	3.3	4.7	0.8

Table 5.4. Specific osteocyte apoptosis detection data

Values in bold indicate significant difference between left and right tibiae (i.e. value for delta is significantly different from zero).

				CD11b % gated M2 gate	CD117 % gated M1 gate
Day 18	HW	Left	Avg	24.92	4.95
			St.Dev.	14.73	10.44
		Right	Avg	31.05	3.06
			St.Dev.	13.45	8.15
		Delta (L - R)	Avg	**-6.13**	1.89
			St.Dev.	3.83	5.84
Day 35	HW	Left	Avg	-2.21	3.66
			St.Dev.	11.30	2.56
		Right	Avg	4.00	4.66
			St.Dev.	10.21	4.43
		Delta (L - R)	Avg	-6.21	-1.01
			St.Dev.	7.53	2.26

Table 5.5. Specific flow cytometry data

Values in bold indicate significant difference between left and right tibiae (i.e. value for delta is significantly different from zero).

				Woven bone area (mm^2)	TRAP pos.pits/CorA #/mm^2	Percent perimeter covered (%) Periosteal	Endosteal
Day 18	HW	Left	Avg	0.13	0.30	0.00	0.00
			St.Dev.	0.08	0.10	0.00	0.00
		Right	Avg	0.00	0.13	0.00	0.09
			St.Dev.	0.00	0.10	0.00	0.21
		Delta (L - R)	Avg	**0.13**	**0.17**	0.00	-0.09
			St.Dev.	0.08	0.15	0.00	0.21
Day 35	HW	Left	Avg	0.18	0.55	5.60	1.17
			St.Dev.	0.10	0.27	4.53	1.85
		Right	Avg	0.00	0.03	0.00	0.60
			St.Dev.	0.00	0.08	0.00	0.93
		Delta (L - R)	Avg	**0.18**	**0.51**	**5.60**	0.57
			St.Dev.	0.10	0.30	4.53	2.06

Table 5.6. Specific TRAP and PSR data

Values in bold indicate significant difference between left and right tibiae (i.e. value for delta is significantly different from zero).

References

Ballas, M. T., J. Tytko, et al. (1997). "Common overuse running injuries: diagnosis and management." Am Fam Physician **55**(7): 2473-84.

Bentolila, V., T. M. Boyce, et al. (1998). "Intracortical remodeling in adult rat long bones after fatigue loading." Bone **23**(3): 275-81.

Bloomfield, S. A. (2006). "Does altered blood flow to bone in microgravity impact on mechanotransduction?" J Musculoskelet Neuronal Interact **6**(4): 324-6.

Bloomfield, S. A., M. R. Allen, et al. (2002). "Site- and compartment-specific changes in bone with hindlimb unloading in mature adult rats." Bone **31**(1): 149-57.

Burr, D. B. and R. B. Martin (1993). "Calculating the probability that microcracks initiate resorption spaces." J Biomech **26**(4-5): 613-6.

Burr, D. B., R. B. Martin, et al. (1985). "Bone remodeling in response to in vivo fatigue microdamage." J Biomech **18**(3): 189-200.

Cao, J. J., P. Kurimoto, et al. (2007). "Aging impairs IGF-I receptor activation and induces skeletal resistance to IGF-I." J Bone Miner Res **22**(8): 1271-9.

Knobloch, K., L. Schreibmueller, et al. (2007). "Rapid rehabilitation programme following sacral stress fracture in a long-distance running female athlete." Arch Orthop Trauma Surg **127**(9): 809-13.

Knothe Tate, M. L., U. Knothe, et al. (1998). "Experimental elucidation of mechanical load-induced fluid flow and its potential role in bone metabolism and functional adaptation." Am J Med Sci **316**(3): 189-95.

Knothe Tate, M. L., P. Niederer, et al. (1998). "In vivo tracer transport through the lacunocanalicular system of rat bone in an environment devoid of mechanical loading." Bone **22**(2): 107-17.

Kogianni, G., V. Mann, et al. (2008). "Apoptotic bodies convey activity capable of initiating osteoclastogenesis and localized bone destruction." J Bone Miner Res **23**(6): 915-27.

Lee, T. C., A. Staines, et al. (2002). "Bone adaptation to load: microdamage as a stimulus for bone remodelling." J Anat **201**(6): 437-46.

Matsuda, J., K. Kurata, et al. (2006). Bone marrow cell differentiation regulated by gel-embedded osteocyte under multi-dimensional gravity. 5th World Congress of Biomechanics, Munich, Germany.

Mori, S. and D. B. Burr (1993). "Increased intracortical remodeling following fatigue damage." Bone **14**(2): 103-9.

Silva, M. J., B. A. Uthgenannt, et al. (2006). "In vivo skeletal imaging of 18F-fluoride with positron emission tomography reveals damage- and time-dependent responses to fatigue loading in the rat ulna." Bone **39**(2): 229-36.

Smith, S. M., J. E. Davis-Street, et al. (2003). "Evaluation of treadmill exercise in a lower body negative pressure chamber as a countermeasure for weightlessness-induced bone loss: a bed rest study with identical twins." J Bone Miner Res **18**(12): 2223-30.

Stevens, H. Y., D. R. Meays, et al. (2006). "Pressure gradients and transport in the murine femur upon hindlimb suspension." Bone **39**(3): 565-72.

Verborgt, O., G. J. Gibson, et al. (2000). "Loss of osteocyte integrity in association with microdamage and bone remodeling after fatigue in vivo." J Bone Miner Res **15**(1): 60-7.

Zhang, L. F., B. Sun, et al. (2003). "Effectiveness of intermittent -Gx gravitation in preventing deconditioning due to simulated microgravity." J Appl Physiol **95**(1): 207-18.

Zwart, S. R., A. R. Hargens, et al. (2007). "Lower body negative pressure treadmill exercise as a countermeasure for bed rest-induced bone loss in female identical twins." Bone **40**(2): 529-37.

CHAPTER 6

CONCLUSION

The potential effects of geriatrics related factors such as age and disuse on the potential increase in the risk of whole bone fracture was not well understood. This thesis set out to examine the effect of these factors on microdamage-related remodeling, which has been associated with whole bone fracture risk when dramatically altered.

In chapter 2 the effects of age on bone remodeling in response to microdamage were explored in addition to introducing a unique experimental animal model. The model which consists of a novel hydraulic chamber was developed for the specific need to apply controlled cyclic loads to intact distal femoral trabecular bone in rats. The implementation showed that the model was capable of delivering effective characterization of damage accumulation and subsequent response in trabecular bone in vivo. Using the model in a cohort of mature and old rats, older rats showed a reduced ability of bone to recover after damage and removal of microdamage was altered with advancing age. The absent or delayed remodeling response has later been shown to be present in cortical bone, too (Herman, Faria et al. 2006). The reason behind the alteration with age could be due to an increase in mineralization with aging (Nagaraja, Lin et al. 2007). Increased mineralization has been shown to cause a reduction in toughness in bone with age (Zioupos 2001). Because of this, bone loses its ability to generate diffuse

damage, creating more linear microcracks, that have a unique ability to activate targeted remodeling (Herman, Berman et al. 2008). In addition, aging causes a decrease in lacunae density that correlates with an increase in crack density (Vashishth, Verborgt et al. 2000; Frank, Ryan et al. 2002). Hence, considering ceteris paribus, aging bone will accumulate more microdamage if remodeling rates are not increased. Substantial increases in the rate of remodeling may not be possible in old animals due to a reduction of skeletal blood flow (Prisby, Ramsey et al. 2007) and impairment of IGF-I receptor activation with age (Cao, Kurimoto et al. 2007). As a result, even if aging bone is capable of detecting microdamage, the localized delivery of cells necessary for remodeling is reduced, and the subsequent bone formation is blunted, allowing more microdamage to accumulate due to a reduced remodeling response.

The positive feedback loop between increases in microdamage and subsequent remodeling could be enhanced by secondary effects associated with aging such as disuse, caused by a decrease in physical activity and/or infirmity. Hence, not only is microdamage repair in general reduced in elderly individuals, but the cessation of activity with increased age could possibly exacerbate this reduction. Considering this, sporadic periods of activity intermixed with times of disuse, might make individuals prone to microdamage accumulation, and therefore at increased risk of fracture. The influence of disuse on bone remodeling could therefore potentially provide clinically important insight into the relationship between microdamage accumulation and increased fracture risk in the elderly. The experiments addressing this question are described in chapter 4 and 5, while the necessary animal models associated with these experiments were presented in chapter 3.

In chapter 3, two animal models capable of inducing cortical microdamage in the tibia were presented. The development, the subsequent testing to fulfill experimental criteria, and subsequent selection for future experiments were shown. Finally the development and verification of a third animal model capable of simulating disuse, was presented. The hindlimb suspension model was shown to be capable of inducing physiologic changes similar to other disuse models in the literature.

With the successful verification and selection of two animal models capable of inducing microdamage and simulating disuse, chapter 4 utilized them to examine the effect of disuse on remodeling associated with microdamage. The experiment in chapter 4 demonstrated that disuse altered the microdamage response through a reduction in woven bone production and the lack of resorption of microdamage. Most importantly, while many studies have proposed that the repair of microdamage is triggered by cell apoptosis (Burr, Martin et al. 1985; Burr and Martin 1993; Mori and Burr 1993; Bentolila, Boyce et al. 1998; Verborgt, Gibson et al. 2000; Lee, Staines et al. 2002; Cardoso, Laudier et al. 2006), the present results suggest that this mechanism may be insufficient without the stimulus associated with mechanical usage. Specifically, we showed that although disuse did not alter the amount of apoptotic osteocytes caused by induced microdamage, the 'active' signal for resorption of microdamage was not present, which could be due to a the lack of fluid flow through the canalicular system, resulting in a futile delivery of resorption initiating signals from the apoptotic osteocytes.

Chapter 5 examined the concept that daily short-term loading of damage induced bones could rescue this 'active' signal for resorption of microdamage by providing a short stimulus of loading hypothesized to induce fluid flow through the cortex. The

results showed that intermittent loading did not increase woven bone production above that observed in hindlimb suspended animals following microdamage, but the targeted resorption of microdamage was rescued. This underscored the results found in chapter 4, effectively showing that the mechanism by which targeted remodeling is 'sensed' is indeed dependent on the stimulus associated with mechanical usage.

In aggregate the data presented in this thesis suggest that elderly individuals with severe activity reductions may further accumulate microdamage and therefore have an increased fracture risk, due to a dual reduction in targeted remodeling by both age and disuse. In addition, the data suggest that elderly individuals could prevent microdamage accumulation through moderate exercise. This knowledge also supports the potential for altering the current clinical therapeutic paradigm for treating stress fractures. Rather than implementing a regimen of extended non-weight bearing (current treatment method), future clinical studies should evaluate the potential of controlled therapeutic loading on the rate and extent of recovery from stress fractures.

References

Bentolila, V., T. M. Boyce, et al. (1998). "Intracortical remodeling in adult rat long bones after fatigue loading." Bone **23**(3): 275-81.

Burr, D. B. and R. B. Martin (1993). "Calculating the probability that microcracks initiate resorption spaces." J Biomech **26**(4-5): 613-6.

Burr, D. B., R. B. Martin, et al. (1985). "Bone remodeling in response to in vivo fatigue microdamage." J Biomech **18**(3): 189-200.

Cao, J. J., P. Kurimoto, et al. (2007). "Aging impairs IGF-I receptor activation and induces skeletal resistance to IGF-I." J Bone Miner Res **22**(8): 1271-9.

Cardoso, L., D. M. Laudier, et al. (2006). Inhibition of osteocyte apoptosis prevents activation of bone remodeling after fatigue in vivo. Orthopaedic Research Society, Chicago, IL.

Frank, J. D., M. Ryan, et al. (2002). "Aging and accumulation of microdamage in canine bone." Bone **30**(1): 201-6.

Herman, B. C., D. Berman, et al. (2008). Activation of bone remodeling after fatigue: Differential response to linear microcracks and diffuse damage. Orthopaedic Research Society, San Francisco, CA.

Herman, B. C., B. Faria, et al. (2006). Significant differences in fatigue behavior and remodeling response exist between young adult and older adult rat bones. Orthopaedic Research Society, Chicago, IL.

Lee, T. C., A. Staines, et al. (2002). "Bone adaptation to load: microdamage as a stimulus for bone remodelling." J Anat **201**(6): 437-46.

Mori, S. and D. B. Burr (1993). "Increased intracortical remodeling following fatigue damage." Bone **14**(2): 103-9.

Nagaraja, S., A. S. Lin, et al. (2007). "Age-related changes in trabecular bone microdamage initiation." Bone **40**(4): 973-80.

Prisby, R. D., M. W. Ramsey, et al. (2007). "Aging reduces skeletal blood flow, endothelium-dependent vasodilation, and NO bioavailability in rats." J Bone Miner Res **22**(8): 1280-8.

Vashishth, D., O. Verborgt, et al. (2000). "Decline in osteocyte lacunar density in human cortical bone is associated with accumulation of microcracks with age." Bone **26**(4): 375-80.

Verborgt, O., G. J. Gibson, et al. (2000). "Loss of osteocyte integrity in association with microdamage and bone remodeling after fatigue in vivo." J Bone Miner Res **15**(1): 60-7.

Zioupos, P. (2001). "Accumulation of in-vivo fatigue microdamage and its relation to biomechanical properties in ageing human cortical bone." J Microsc **201**(Pt 2): 270-8.